THE DEVELOPMENT OF AN ANTENNA ARRAY FOR MOBILE SATELLITE COMMUNICATIONS

BY

Frank Mark Franczyk

A Thesis

Submitted to the Faculty of Graduate Studies

In Partial Fullfillment of the Requirements

for the Degree of Master of Science

University of Manitoba

Department of Electrical Engineering

Winnnipeg, Manitoba

Canada

May, 1987 

ISBN 0-315-37450-0

THE DEVELOPMENT OF AN ANTENNA ARRAY FOR MOBILE SATELLITE COMMUNICATIONS

BY

FRANK MARK FRANCZYK

A thesis submitted to the Faculty of Graduate Studies of the University of Manitoba in partial fulfillment of the requirements of the degree of

Master of Science

ABSTRACT

A mobile terminal antenna array for satellite communications in the L-Band is designed and investigated numerically and experimentally.

Ten- and twelve-element conical patch array configurations were numerically simulated and optimized for modified MSAT design guidelines. The arrays yielded an absolute gain of 10 dBic over the required elevation region by adjustment of the conical tilt angle. Complete azimuth coverage was obtained by generating two beams per three active elements with the utilization of a 45 degree phase shift, relative to the central element, to each of the two outer elements. A feed network and the beam position control, as well as the numerical and experimental results for the element's input impedance, complete the presentation of the development of a suitable array.

In the experimental investigation, a 10-element array configuration was constructed and losses due to the feed network and terminal mismatch were measured to be 3.26 dB. The array's radiation characteristics were observed for three different element dimensions and data concerning the beam peak gain, location, and field ellipticity, is presented. The influence of the patch-edge to ground plane distance, in combination with different ground plane sizes, is noted and recommendations for future experiments are given. Absolute gain patterns are also generated from the experimental rotating linear patterns and are compared to numerically generated results showing suprisingly good agreement.

ACKNOWLEDGEMENTS

I wish to express my sincere thanks and appreciation to Dr. L. Shafai for his guidance, advice, and inspiration throughout every stage of the project. I am indeed indebted to him for the time taken during our long discussions since they have certainly resulted in the broadening of my knowledge in the antennas field.

Special thanks also to Dr. Arun Bhattacharyya for his technical help and to Brad Tabachnik for his help with the experimental work in the anechoic chamber. My deepest appreciation is also extended to Greg Bridges for his review of the first draft of the thesis. As well, extended thanks to my fellow colleagues, Rick Smegal and Sid Allman, for the helpful discussions and advice in the preparation of the thesis.

Finally, I acknowledge the financial assistance provided by the Province of Manitoba's Industry, Trade, and Technology Division under the Manitoba Graduate Scholarship. I sincerely hope that the program continues and such scholarships are available to upcoming graduate students.

TABLE OF CONTENTS

LIST OF SYMBOLS

α^i	Phase excitation of i^{th} feed
α_{ij}	Direction cosines for transformation of coordinates
$\hat{a}_\rho$, $\hat{a}_\theta$, $\hat{a}_\phi$, $\hat{a}_z$	Unit vectors in ρ, θ, ϕ and z dimensions.
a	Physical radius of the circular microstrip patch (cm)
a_{eff}	Effective radius of the circular microstrip patch (cm)
AR	Axial ratio
d	Feed probe diameter
dB	Decible value
dBi	Decible gain with respect to an isotropic source
dBic	Absolute circularly polarized gain in dBi
ε_r	Relative dielectric permittivity
ε_o	Permittivity in a vacuum (8.85 pF)
EFIE	Electric field integral equation
E_θ, E_ϕ	Electric field components in θ, ϕ dimensions (V/m)
GHz	Giga Hertz (10^9 cycles per second)
h	Thickness of dielectric substrate (mm)
k_d	Wave number in a dielectric medium (rad/m)
k_o	Wave number in free space (rad/m)
L-Band	Frequency band from 1.0 - 2.0 GHz
λ	Wavelength for a frequency f (cm)
λ_o	Wavelength for a frequency f_o (cm)
MFIE	Magnetic field integral equation
μ_o	Permeability of a vacuum (400π nH/m)
MSAT	Mobile Satellite
MHz	Mega Hertz (10^6 cycles per second)

NEC	Numerical Electromagnetic Code
η	Free space impedance ($120\ \pi\ \Omega$)
ω	Angular frequency (rad/s)
ρ_o	Feed probe position
R,X	Resistive and reactive components of input impedance
TM	Transverse magnetic ($H_z = 0$)
UHF-Band	Ultra-High frequency band (500- 1000 MHz)
Z	Complex input impedance
ρ, ϕ, z	Cylindrical coordinates
r, θ, ϕ	Spherical coordinates
r_t, θ_t, ϕ_t	Translation coordinates
ψ_p, ψ_y, ψ_r	Pitch-yaw-roll coordinates

LIST OF TABLES

LIST OF FIGURES

CHAPTER 1

INTRODUCTION

1.1 Background and Purpose

Since 1980, Canada has taken a leading role in the investigation of a satellite system which will provide fixed, semi-portable and mobile communications to all of Canada including the 200 mile offshore limits. Approved and partially funded by the Canadian Government, the system will improve and in some cases establish communications to isolated rural and remote communities. Moreover, the business aspect of the system is forseen to be economically attractive in complementing current cellular mobile communications in the lower latitudes with many added benefits.

A satellite communication system employs a different band of frequencies for transmit and receive over a vast geographical region. In contrast, a cellular mobile communication system reuses a limited range of frequencies over discrete subdivided regions known as cells with the level of isolation between cells determined by the cell size and the transmitter power level. As a result, from the mobile antenna design standpoint, the only stipulation enforced on the cellular system design is for the antenna to have omnidirectional coverage. Hence, a single element such as a monopole whip or loop, which is fairly inexpensive and simple to construct, can be used.

The mobile antenna for the satellite based communication system, on the other hand, must meet many more performance specifications than simple omnidirectionality. The directivity of the antenna, for example, must be large in the high latitude regions since the satellite will be located in a geosynchronous orbit above the equator. As well, the satellite will have limited resources as to antenna size and transmitter power. Thus, a single antenna element will normally not provide the required gain to establish the

proper communication link. An array of discrete elements must therefore be configured to meet the requirements.

The purpose of this thesis is to present an antenna array configuration which will perform up to reasonable design standards set on the mobile terminal antenna for the MSAT (Mobile Satellite) program and in addition be of a fair size and inexpensive to fabricate.

1.2 Review of Existing Antenna Designs for MSAT

The fact that an array of elements is required for the mobile ground station antenna has been somewhat justified in the previous section. Further defense comes from the fact that more than one satellite may eventually be placed in orbit for this service. As a result, the antenna would have to have the ability for satellite discrimination, a characteristic that an omnidirectional single element lacks. The task that remains, then, is to determine the type of individual element to use and design an appropriate array configuration.

During the Phase B studies of the MSAT program, the push for a mobile terminal antenna began. Since the MSAT program was still in its development stage at that time, several single element radiators were considered as possible candidates These included the drooping crossed-dipole, the four-arm conical log-spiral, and the backfire quadrifilar helix antennas. Butterworth [1] studied these three types and presented experimental data on their performance in the UHF band. The results showed that each radiator had most of the required characteristics, but at the expense of a bulky physical structure. A low profile antenna, the microstrip patch, was another possible candidate that was studied. Shafai and Kumar [2] presented data for a circular patch operating in different modes. Broadside radiation resulted with dominant mode excitation while the excitation of the higher order modes caused the main beam to shift off the axis to the lower elevation regions. They concluded that the antenna was an excellent candidate

if improvements could be made to its narrow frequency bandwidth.

Based on some of the single antenna elements mentioned, several antenna arrays have been proposed. One in particular, the planar circular patch phased array, is perhaps one of the best practical designs for a mobile antenna because of its planar profile. Several authors [3], [4], and [5] have studied the array and have presented data on its performance. The design by Shafai et al [5] is perhaps the best analyzed and tested since all mututal coupling effects were included in the analysis. The experimental results show that the array meets most of the performance specifications up to an elevation angle of 60 degrees from the zenith axis. Beyond 60 degrees, the gain of the antenna decreases rapidly. For U.S. coverage, this is acceptable, but will not meet the Canadian specifications where the coverage area must extend down to 65 degrees. The array also requires an elaborate and hence expensive feed network. Expensive refers to the cost of the network with respect to today's state of the art of the required components. In the future, these costs will undoubtedly decrease.

A drooping dipole phased array was also studied and tested. Neilson [6] presented simulated results for a numerically optimized antenna array and concluded that a six element array of crossed drooping dipoles would provide the required gain, polarization and beam steering capabilities for the MSAT system. Jacob and Feuer [7] presented the experimental results for such an array, but one comprised of seven drooping dipoles. The radiation patterns for the 820 - 870 MHz band showed a peak gain which fell between 45 degrees and 90 degrees off zenith. Noted was the fact that the axial ratio was very sensitive to the operating frequency as it increased well beyond the 3 dB threshold. Perhaps the drawback to the array is its size. The height of each element was stated as 0.56 λ_o or 10.6 cm in terms of the L-Band midband frequency of 1.6 GHz where the wavelength is 18.75 cm. Combined with its total surface area, the array turns out to be quite massive, and hence impractical for most mobile vehicles.

Recently, Milne [8] presented a 17- element monopole switched array. Unlike phased arrays which require an elaborate feed network with multi-bit phase shifters, a switched array simply uses one or two diode-type switches to control the excitation of specific elements. The proposed design is ingeneous in that it uses the monopole elements as both active and passive devices. The passive elements form a parabolic reflector in front of the active one. This results in a directional scattering of the energy to the appropriate elevation regions, while the switching control to adjacent elements produces the required azimuthal coverage. Moreover, the array has two beam states, for the low and high elevation regions, and apparently has a peak gain of approximately 10 dBi. It is not indicated whether this gain is absolute or if it is the true gain at the receiver terminals. In addition, the array is designed to receive linearly polarized energy. Hence, the signal power received will be 3 dB less since the incident signal from the satellite is circularly polarized. This is a drawback, but in respect to the polarization diversity which is required by a circularly polarized antenna, the linearly polarized array need not distinguish between the right and left handed circularly polarized signals. Consequently, its feed network will be less complicated.

As far as other array designs for the required application, it is worth mentioning that mechanically steered arrays were also considered. However, the disadvantage about this option is that its usefullness in the Canadian harsh environment is limited. Moreover, the array will undoubtedly be expensive to fabricate and later maintain. Consequently, it is not a feasible option and the electrically switched or phased arrays will be employed.

1.3 Scope

The current MSAT design goals and coverage area definitions for the mobile ground station antenna will be presented in Chapter 2 along with appropriate modifications to those which are not considered feasible. The word 'current' is proper

at this time since frequency allocations and satellite specifications have not yet been confirmed. Chapter 3 presents numerical results for the investigation of possible element plus scatterer configurations which were considered before a final choice for the array element was made. The design arrangement and composition decided upon, the conical circular patch array, will then be presented in Chapter 4.

Chapter 4 includes the theoretical analysis for the single element and derives the far fields with definitions for the axial ratio, the co- and cross-polar field components, and the directivity. The coordinate transformations for the purpose of referencing the individual elements to a global coordinate system are then presented, followed by the numerical simulations of two different array configurations in free space with two and three element excitations. Futher simulations are presented for possible superarray arrangements with the inclusion of additional elements. A discussion on the antenna's feeding arrangement and beam control are also given and the chapter concludes by presenting theoretical and experimental values for the input impedance of the single element.

Chapter 5 presents the experimental data obtained for the single element and a 10-element array configuration which were extensively tested for various orientations with finite and extended ground plane sizes. The final chapter of the thesis presents a discussion on the numerical and experimental results, and presents recommendations for future experimentation and analysis.

CHAPTER 2

MSAT SYSTEM REQUIREMENTS FOR A MOBILE TERMINAL ANTENNA

The first generation MSAT ground station system is based on many studies concerning the spacecraft design, propagation measurements, and link simulations in shadowing and fading environments. These and other studies have resulted in standard design goals for the various components of the system. The antenna on the mobile terminal is an important component in this system, and as mentioned in the introduction, the restrictions on its performance specifications have varied since the initial system conception and will no doubt change again. The principal reason for these changes is the attempt to make the communication link economically viable, both for the system manager and system user.

In this short chapter, the most recent design goals for the mobile ground station antenna will be presented in conjunction with the performance specifications within the region which are considered reasonable and feasible. The definitions found in this chapter will then be used as guidelines in the determination of an optimum antenna design.

[A] Beam Coverage and Frequency Bands

Initially, the proposed satellite was to provide coverage to both Canada and the U.S. with four beams at the L- Band and two beams at the UHF Band. The expected satellite footprints are shown in Fig. 2.1. The UHF band has been allocated a 4 MHz uplink from 821 - 825 MHz and a 4 MHz downlink from 866 - 870 MHz. The L-Band allocation occupies 55 MHz with a 1544 - 1599 MHz uplink and a 1645.5 -

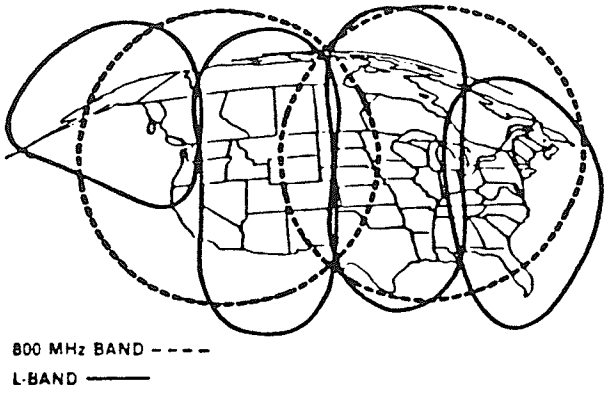

Figure 2.1: MSAT beam coverage [9]

1660.5 MHz downlink. Due to strong opposition by various cellular mobile radio equipment producers, it is unlikely that the UHF band will be employed for the MSAT system. Consequently, only L-Band service will be available. For this reason, the antenna design will be based on L-Band frequency operation.

For the determination of the position of the mobile with respect to the satellite, a pilot signal will be transmitted over the entire coverage region. This pilot will be transmitted from the central control station and will be reflected by the satellite. It is expected that the pilot will be at a higher power level and in addition, be at a frequency very near the downlink frequency band. Hence, the antenna array feed network design should be able to distinguish this signal and process it appropriately to scan over the entire region.

[B] Scan Volume

For Canada wide coverage, the antenna is to have a directive beam covering the polar region from 40 to 65 degrees, where Fairbanks, Alaska was selected as the northern- most point, and Windsor, Ontario as the southern-most point. The azimuth coverage should be omnidirectional. In array configurations, complete azimuth

coverage is obtained by phasing or switching groups of elements. A three dimensional representation of the scan volume from $\phi = 0$ to 360 degrees in the required elevation region for a particular azimuth section is shown in Fig. 2.2.

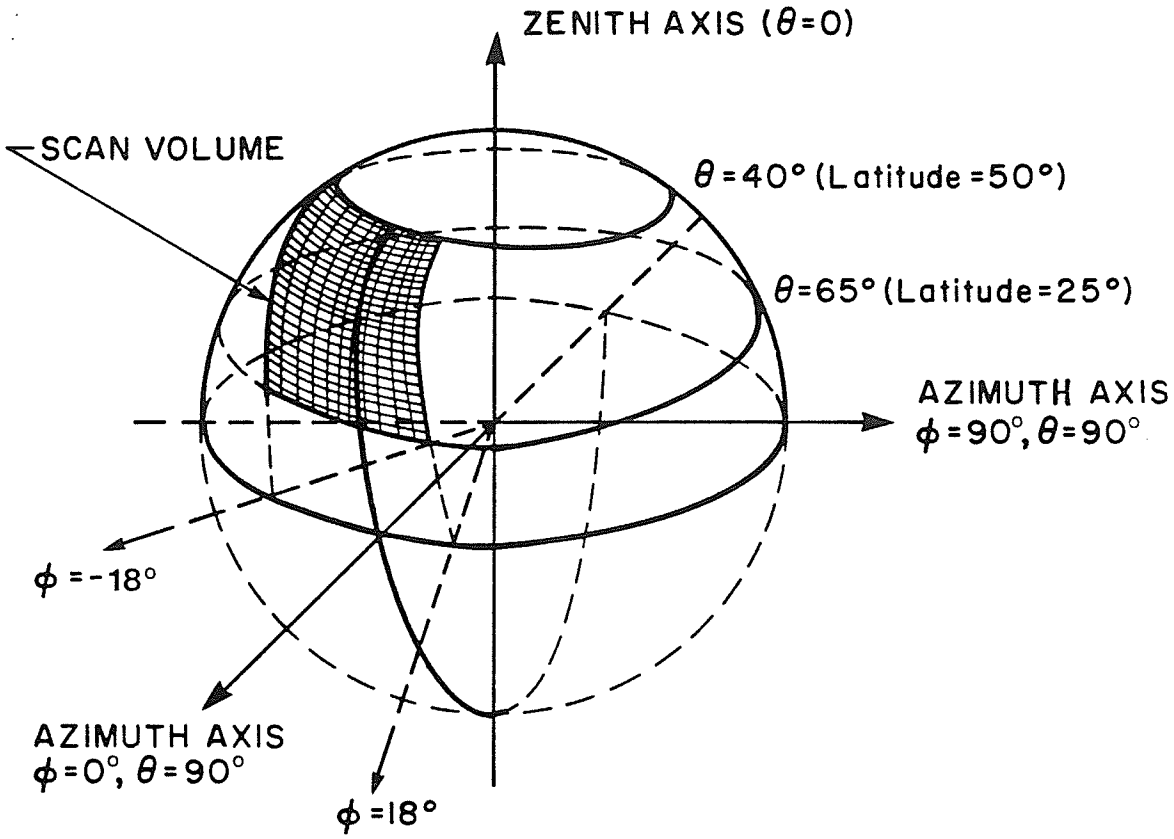

Figure 2.2: Elevation scan volume for Canada-wide coverage

The section of the global sphere from $\theta = 0$ to 90 degrees for the ϕ section from $\phi =$ -18 to 18 degrees is mapped out onto a flat surface in Fig. 2.3. The contour lines show the values of the absolute gain of the mobile antenna as would be seen from the satellite's perspective.

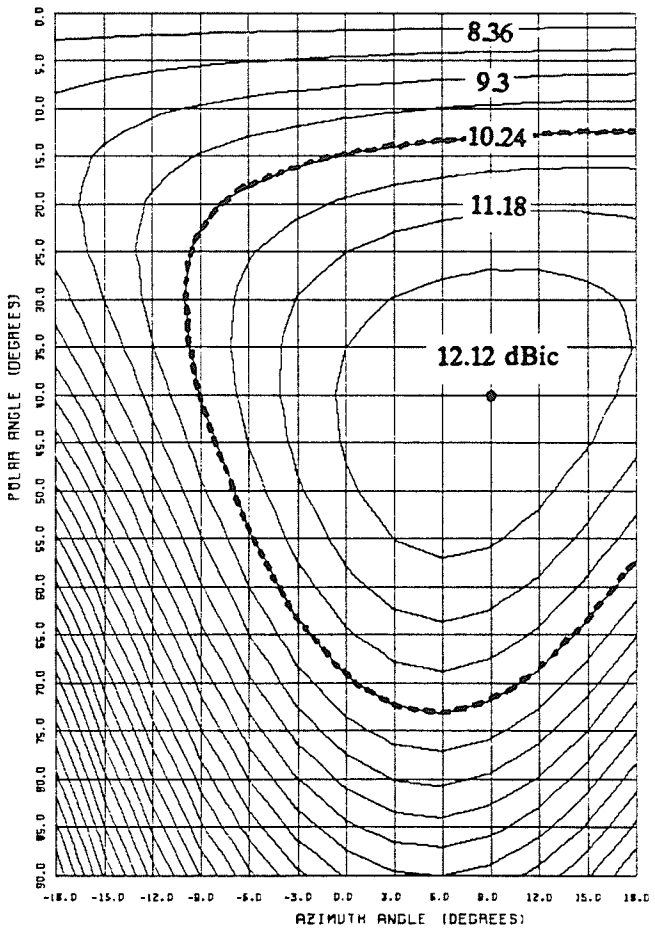

Figure 2.3: Gain contour plot of ϕ-sectioned scan volume

[C] Antenna Gain, Ripple and the 8.0 dB Beamwidth

The gain of an antenna is equal to its directivity multiplied by its radiation efficiency. The radiation efficiency includes the mismatch and insertion losses inherent in the feed network of the antenna, as well as the polarization loss. By not including these losses, the gain is equal to the directivity and will be refered to as absolute. Including the losses gives the true or net gain of the antenna system. The minimum required true gain at the receiver terminals is that quantity which must be achieved over the entire coverage region. For the L-Band, a minimum net gain of 12.0 dBic has been stipulated. This value will undoubtedly be decreased if reasonably sized and priced mobile antennas are to be employed. Hence, a minimum required gain of 8.5

dBic will be assumed for the work in this thesis. Assuming losses on the order of 1.5 to 2.0 dB to account for the radiation efficiency, absolute gains greater than 10 dBic will be pursued for the worst case regions of the coverage area. Hence, peak gains on the order of 12 dBic must be obtained in general.

The ripple value of the array is defined in the H-plane as the difference in gain of the beam peak maximum in the corresponding azimuth plane, to the gain of the fields in the worst case azimuth plane. This ripple definition assumes that the beam peak is pointed directly at the satellite, and therefore provides a good picture of the beam coverage in addition to an E-plane pattern. In defining the ripple as such, a design goal of 2.0 dB will be enforced with the minimum gain set at 10.0 dBic in the worst-case azimuth plane.

Another design guideline used in the array simulation was to achieve a minimum of 8.0 dBic over the complete elevation and azimuth regions. This value was simply used for design aid purposes since it was more readily achievable than the required 10.0 dBic. Thus, the 8.0 dBic beamwidth characteristic provided yet another picture of the radiation characteristics obtained from each array arrangement and determined whether a particular array configuration had the potential for further analysis.

[D] Polarization and Impedance Bandwidth

The antenna must discriminate between right and left hand circular polarization in a switchable configuration. This is evident from Fig. 2.1 where each adjacent footprint is oppositely polarized. This polarization scheme produces the required isolation between the footprints. The design goal for the axial ratio, which is the measure of the ellipticity of the received fields, is 3.0 dB. That is, the ratio of the cross- to co-polar field components received should be no greater than 17 %.

The impedance bandwidth of the antenna is required to be on the order of 7.5 % to comfortably include uplink, downlink and pilot signals. What this means is that the antenna should be matched to 50 Ω over 7.5 % or 120 MHz of the L-Band centered about 1.6 GHz. This matching is discussed in the section on input impedance in Chapter 4.

[E] Physical Size and Cost Considerations

Two other design considerations inherent in the development of a suitable antenna are the physical dimensions and expected costs of fabrication. The antenna must be suitable for placement on all mobile vehicles from automobiles to planes. As well, the antenna must be reasonably inexpensive to manufacture, for as mentioned earlier, the communication link must be economically attractive to the user.

CHAPTER 3

SINGLE ELEMENT CONFIGURATIONS

3.1 Introduction

The initial work towards finding a suitable antenna configuration for the MSAT application involved the use of existing software to model the antenna and then to examine the resultant far field patterns. The Numerical Electromagnetic Code (NEC) program, which is based on the EFIE, MFIE, or a combination of the two, and the ROT2 program, which is based on the EFIE, were the two tools used in configuring possible single element radiators which could be later arranged in array fashion. Wire mesh structures over an infinite ground plane were used to model the elements with NEC, while rotationally symmetric conducting geometries over finite ground planes were modelled with ROT2.

This chapter describes several types of antenna geometries and presents examples of the numerically generated far field distributions for most of them. The far field E-plane elevation pattern and the antenna's directivity were the only characteristics considered at this particular stage in the development.

3.2 The Slotted Cylinder

It is well documented that an axial slot on a narrow cylinder produces a broad endfire pattern and that an array of these slots produces a directive endfire beam. Jordan [10] , shows these results for a center-fed slot, 0.75 λ in length on a cylinder in free space. Based on the pattern, it was conjectured that an axially slotted cylinder placed above a ground plane and excited at its top end would result in a beam with a

peak off zenith. The slotted cylinder with an appropriate excitation is shown in Fig. 3.1 as it was modelled for the NEC program.

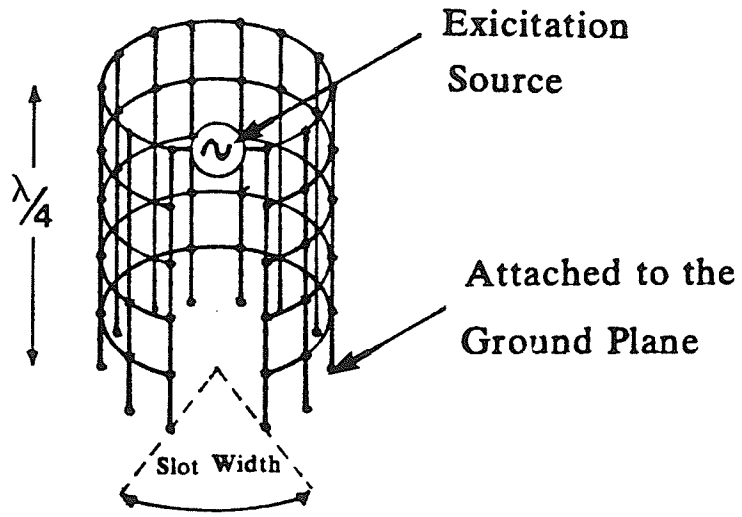

Figure 3.1: The cylinder with axial slot as modelled for NEC

Since the field distribution across the slot is ϕ-directed, electric currents exist along the periphery of the slot, as well as azimuthally around the cylinder. To determine the radiated fields directly in front of the slot, the electric field distribution over the slot can be replaced by an equivalent magnetic current source. For an equivalent magnetic source, $\frac{\lambda}{4}$ in length above a ground plane, the corresponding image will also be $\frac{\lambda}{4}$ in length below the ground plane, but directed in the opposite direction.

Based on the complementary structure, the far field directly in front of the slot, would be horizontally polarized and would have a pattern variation of the following form,

$$P(E_\phi) = A \tan\theta \, [1-\cos(\frac{\pi \cos\theta}{2})] \qquad (3.1)$$

This variation generates a far field peak maximum at $\theta = 45$ degrees with nulls at 0

and 90 degrees. The numerically generated results are in agreement with this pattern variation only for the smaller sized cylinders. The results for the larger sized cylinders deviated from the predicted patterns. The slotted cylinders considered had slot widths from 3 to 30 degrees, diameters from 0.125 λ to 1.0 λ and a vertical height of 0.25 λ.

For cylindrical diameters less than 0.2 λ, a beam peak maximum at θ= 45 degrees was obtained. As the cylinder diameter was increased beyond 0.2 λ, the beam peak shifted towards the zenith axis and for large cylindrical diameters, i.e. $D \geq 0.5\ \lambda$, the beam peak relocated behind the slot. This result was linked to the modelling of the the slot itself, as nothing prevented the energy to radiate in the opposite direction (the distance to the cylinder back wall from the slot is larger for the larger diameters). Semi-circular and square mesh cavities were modelled in behind the slot, but the energy in the backward direction continued to be greater than that in the forward direction. Furthermore, for the smaller cylinders, it was noted that much more energy was radiated to the sides of the slot rather than directly in front of it. Thus, it seems that the azimuth currents along the diameter of the cylinder are much larger than the equivalent magnetic current source. This result is noted since it could affect the performance of an array of these axial slots when configured around the cylinder. Several field patterns are shown in Fig. 3.2 for a slot width of 6 degrees, a height of 0.25 λ and for various cylinder diameters.

3.3 The Cylinder as a Scatterer

A source radiating in the presence of an infinite conducting cylinder in free space is one of the most common scattering problems studied in electromagnetics [11]. Configuring a finite cylinder above a ground plane and using horizontal dipoles and vertical monopoles as the excitation sources complicates the analytical analysis considerably. It is known, however, that this type of arrangement increases the directivity of the far field [12]. It was on this premise that a numerical investigation was undertaken to generate the far field patterns for this geometry.

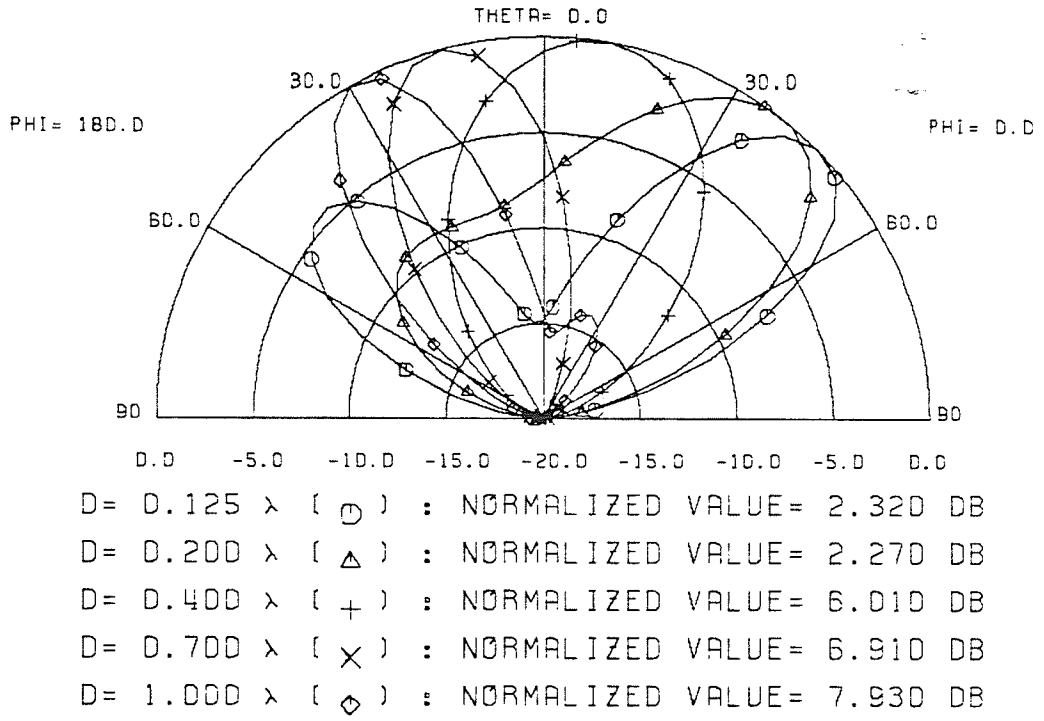

Figure 3.2: Patterns for Axially Slotted Cylinder of Various Diameters

3.3.1 Horizontal Dipole Excitation

A horizontal $\frac{\lambda}{2}$ dipole is placed in front of a cylinder of height $\frac{\lambda}{4}$ mounted on a ground plane as shown in Fig. 3.3. The solid cylinder was once again modelled as a mesh structure when NEC was employed for the infinite ground plane analysis. The dipole consisted of seven wire segments with the central segment excited. With ROT2, the cylinder was generated as a rotationally symmetric conducting contour, and an extended lip was modelled to simulate a finite ground plane. The exciting dipole source also consisted of seven short wire radiators, but here, each segment had a specific amplitude and phase associated with it, such that the total excitation would simulate a cosinusoidal current distribution.

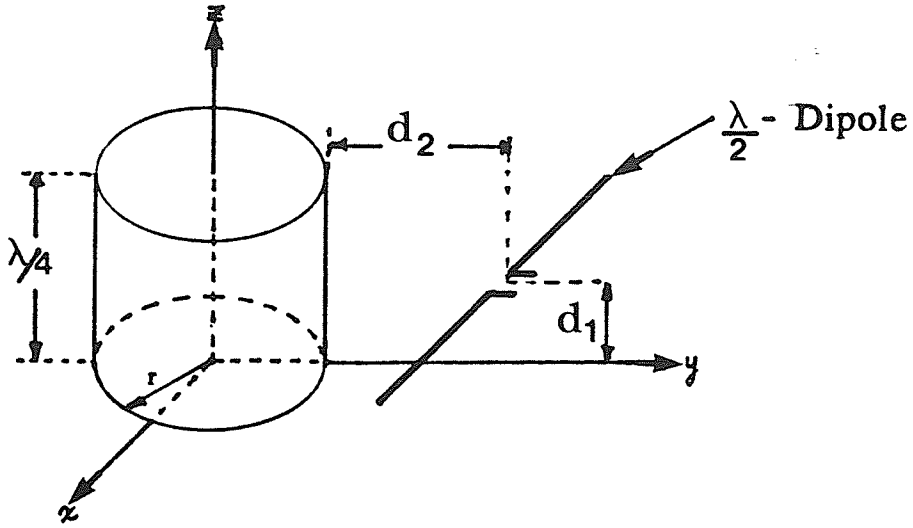

Figure 3.3: Horizontal dipole excitation of the cylindrical scatterer

For the infinite ground plane analysis, in absence of the cylindrical scatterer, it was found that the peak of the far field occured at $\theta = 0$ degrees. The directivity was high for dipole positions near the ground plane and decreased rather quickly as the dipole was moved farther away, causing the pattern to broaden substantially.

With a cylindrical scatterer, $\frac{\lambda}{4}$ long, placed in front of the excitation source, the far field pattern directivity increased and the peak gain occured at an elevation angle of $\theta = 20$ degrees for dipole locations near the cylinder. The fields were horizontally linear polarized in the plane normal to the dipole. Off the normal, the fields were elliptically polarized approaching vertical linear polarization in the plane parallel to the dipole. The gain increase with the added scatterer was 1 dB for dipoles situated near the ground plane and up to 2.0 dB for other positions. The distance of the dipole from the cylinder, then, determines the peak location, where the upper bound was found to be at $\theta = 20$ degrees, while the dipole location above the ground plane determines the value of the peak gain. Table 1 summarizes the optimization of the dipole location for the infinite ground plane.

Table 1: Results for the horizontal dipole excitation of a cylinder

Distance Above Gnd. Plane (d1) λ	Distance From Cylinder (d2) λ	Peak Gain (dB)	Polar Angle θ (degrees)
0.055	0.12	9.39	20.0
0.1	0.025	8.99	20.0
0.1	0.12	9.3	20.0
0.125	0.05	9.1	20.0
0.125	0.1	9.23	20.0
0.125	0.3	9.21	15.0
0.125	0.4	9.27	10.0
0.125	0.6	9.5	0.0
0.185	0.12	8.95	20.0

The dipole location was also optimized for a finite ground plane configuration. Without the cylindrical scatterer, the finite ground plane had no effect on the beam peak location, only on the field magnitude. Including the scatterer and a finite ground plane of radius 2.0 λ, the peak of the pattern shifted down to θ= 30 degrees. This was true for dipole locations from 0.1 to 0.225 λ above the ground plane, but for distances less that 0.1 λ, the beam peak shifted back up to θ= 20 degrees, as for the infinite ground plane configuration. Figure 3.4 shows the comparison of the field patterns for finite and infinite ground planes. The diameter of the cylinder is 1.2 λ, the distance of the source from the cylinder is 0.12 λ, its distance above the ground plane is 0.1 λ, and the finite ground plane radius is 2.0 λ.

It should be noted that an attempt was made to shift the beam peak to a lower elevation angle by placing a parasitic dipole of equal length directly above the active dipole. This simulation was performed with the infinite ground plane and NEC. The

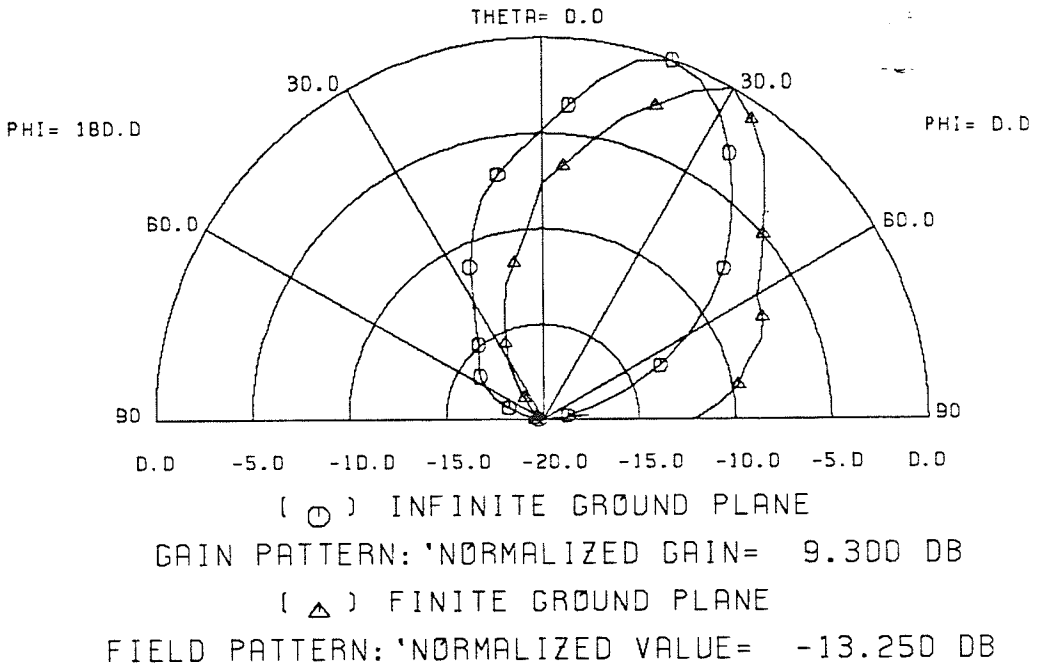

Figure 3.4: Field patterns for finite and infinite ground planes due to the horizontal dipole excitation of a cylinder

results obtained showed that the beam peak did indeed shift, but towards zenith, not towards azimuth. The other interesting result was that the gain increased by 2 dB over the results without the added element. Table 2 lists some of these results.

3.3.2 Vertical Monopole Excitation

The second type of excitation used for the cylindrical scatterer was the $\frac{\lambda}{4}$ monopole. For infinite ground plane analysis, the geometry becomes that of a $\frac{\lambda}{2}$ vertical dipole in front of a finite cylinder of the same length in free space. The geometry is shown in Fig. 3.5.

Table 2: Results with parasitic element above active dipole

Distance of Dipoles from Cylinder (λ)	Distance of Active Dipole Above Grd. Plane (λ)	Distance of Parasitic Dipole Above Grd. Plane (λ)	Peak Gain (dB)	Polar Angle θ (degrees)
0.26	0.055	0.24	11.07	10.0
0.26	0.100	0.24	11.10	10.0
0.26	0.150	0.24	11.12	5.00
0.26	0.180	0.24	11.20	0.00

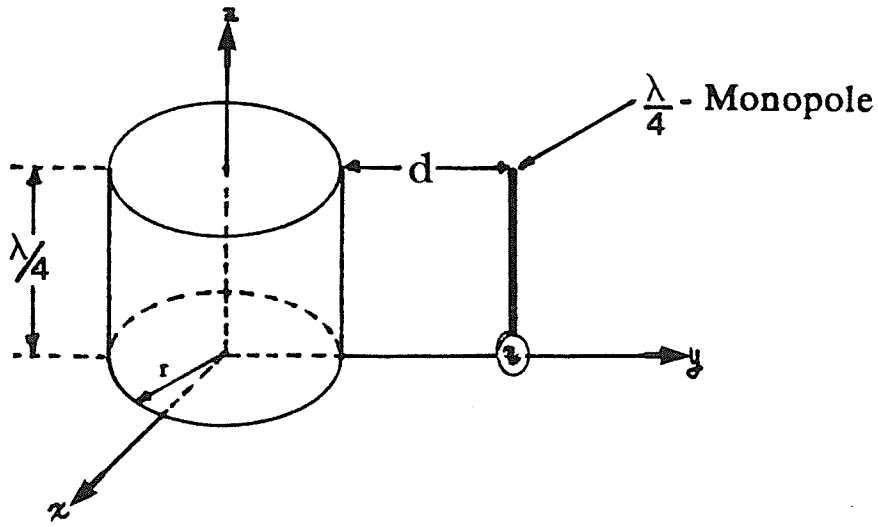

Figure 3.5: Vertical monopole excitation of a cylinder

For infinite ground plane analysis, the monopole was broken down into 5 segments. The bottom segment was excited causing a cosinusoidal current distribution. In the absence of the scatterer, the beam peak occurs at θ= 90 degrees as expected with a peak gain of 5.17 dB. With the scatterer in place, the directivity increases and the beam peak remains at θ= 90 degrees. The peak gain increases by as much as 3.3 dB

for a dipole distance of 0.12 λ from the cylinder. Table 3 summarizes the results for various monopole locations.

Table 3: Results for monopole excitation over infinite ground plane

Distance of Monopole from Cylinder (λ)	Beam Peak (dB)	Polar Angle θ (degrees)
0.12	8.44	90.0
0.20	8.17	90.0
0.26	7.46	90.0
0.36	5.30	90.0

For a monopole above a finite ground plane without a scatterer, distortion in the form of a shift in beam peak towards zenith occurs. In [13], the authors present results for a conical monopole above finite ground plane disks. In particular, for a ground plane radius of 1.5 λ, the peak of the pattern is shown to be at θ= 45 degrees. The ROT2 program was used to verify these results. For a ground plane radius of 1.0 λ, a beam peak at θ= 40 degrees was obtained, while a radius of 1.5 λ produced a beam peak at θ= 80 degrees. Hence, the dipole must be located between 1.0 and 1.5 λ away from the ground plane edge in order to obtain a beam peak at the required θ= 60 degrees in elevation.

For a cylindrical scatterer of radius 0.6 λ placed at the center of a finite ground plane of radius 2.0 λ, appropriate positions of the monopole can produce a beam peak in the required elevation region. The directivity of the beam has increased considerably for monopole positions near the cylinder and decreased as the monopole was shifted farther away. Beam peaks at θ= 60 and θ= 65 degrees were obtained when the monopole distance from the cylinder was increased from 0.12 to 0.25 λ. Figure 3.6

presents the far field patterns for the infinite and finite ground plane results for a monopole placed 0.2 λ in front of a cylinder of diameter 1.2 λ and with a finite ground plane radius of 2.0 λ.

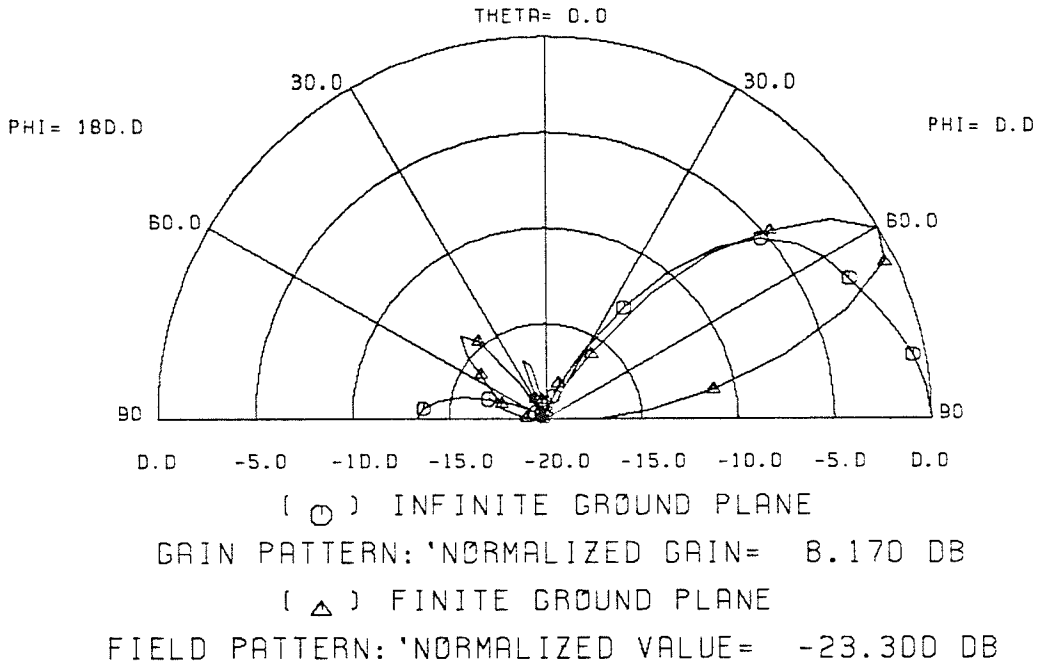

Figure 3.6: Field patterns for finite and infinite ground planes due to the vertical monopole excitation of a cylinder

3.4 Variations of a Scatterer with Monopole and Dipole Excitations

The ROT2 program was further employed for the modelling of two other rotationally symmetric scatterers, namely a truncated cone and an angular corner reflector. Both scatterers are geometric extensions of the cylindrical reflector as they are flanged in either a positive or negative angle. This section briefly summarizes the resultant far field distribution when vertical monopole and horizontal dipole excitations are used.

The conical structure cross-section , as modelled with ROT2, is shown in Fig. 3.7 for both types of excitation sources.

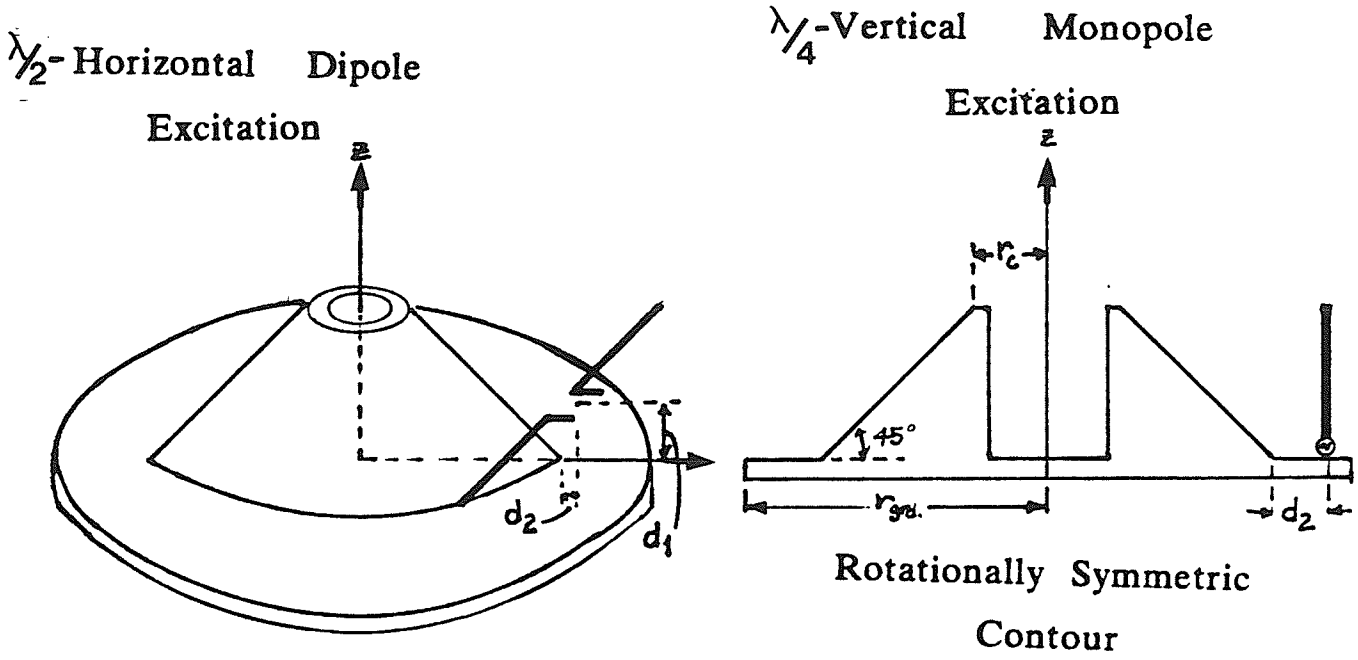

Figure 3.7: The conical scatterer with horizontal dipole and vertical monopole excitations

A conical scatterer was employed to examine the anticipated shift in the beam peak for the horizontal dipole case. For a ground plane radius of 1.5 λ, the beam peak occured at θ= 15 degrees, a shift towards zenith by 5 degrees when compared to the cylindrical scatterer result. The field was very broad over the entire elevation region indicating poor directivity. The vertical monopole excitation, on the other hand, produced a beam peak at θ= 55 degrees when the same geometry was used. The resulting field distribution was nearly identical to that of the cylindrical scatterer result, with the exception of a shift of 5 degrees in the beam peak location. Figure 3.8 shows the field distribution for a conical tilt of 45 degrees, a ground plane radius of 1.5 λ, a horizontal distance of 0.12 λ to the excitation source location, and a distance of 0.1 λ for the location of the horizontal dipole above the ground plane.

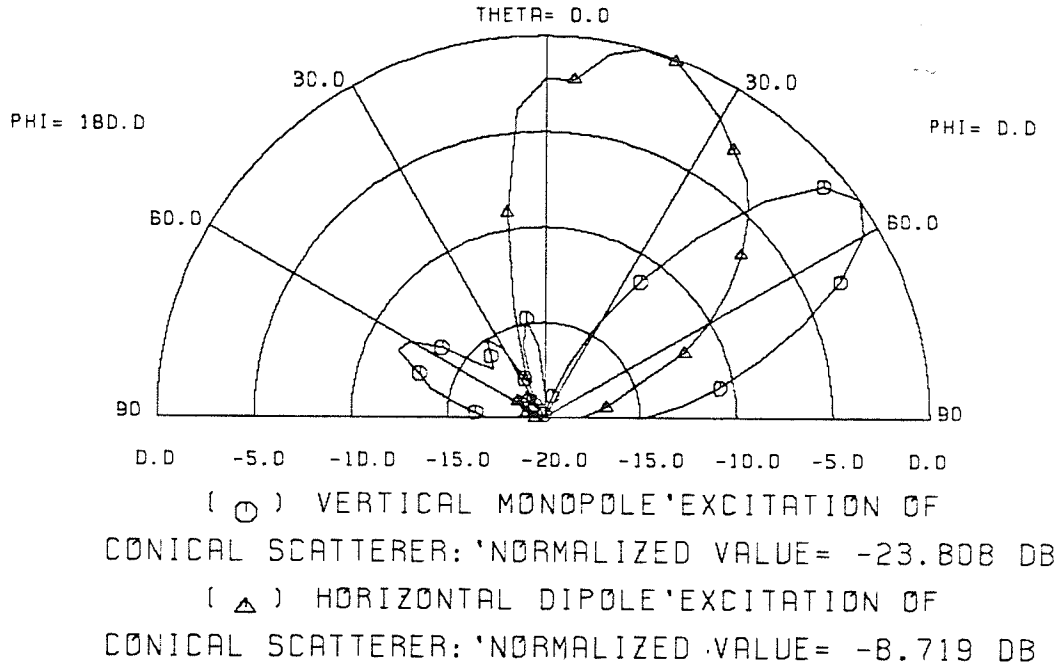

Figure 3.8: Far field patterns for a conical reflector due to horizontal dipole and vertical monopole excitations

The angular corner reflector was also considered since it is known that corner reflectors increase the directivity of the far fields for both horizontal and vertical dipole excitations. It was anticipated that, in addition to increasing the directivity, the angular corner geometry would also cause a beam peak shift for the horizontal dipole excitation. The cross-section for this geometry is shown in Fig. 3.9.

A corner angle of 45 degrees and a ground plane radius of 2.0 λ was chosen for the analysis. The beam peak for the horizontal dipole excitation did indeed shift towards azimuth. The shift, for several dipole locations, was only 5 degrees from that of the cylindrical scatterer, as the beam peak was found to be at θ= 25 degrees. The monopole excitation was also simulated for comparative purposes. The beam peak turned out to be located at θ= 50 degrees, 5 degrees less than that for the conical scatterer. The major difference was that the field strength for the corner reflector was

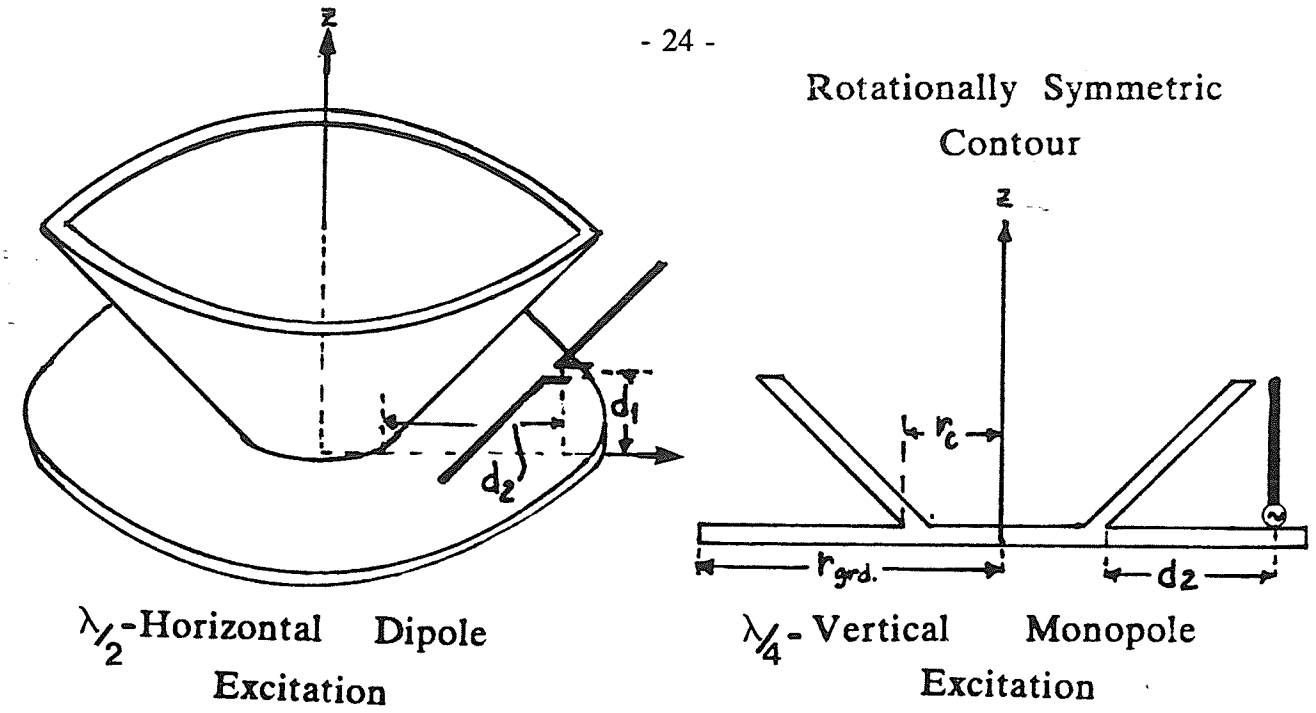

Figure 3.9: The angular corner reflector with horizontal dipole and vertical monopole excitations

much stronger over the elevation region, as expected, indicating a better directivity. Figure 3.10 shows the resultant far field patterns for the two excitations.

3.5 Discussion

Based on the numerical investigations, several conclusions were made regarding the feasibility of the various antenna configurations for their use as a mobile terminal antenna. This section briefly describes these conclusions.

First of all, a circularly polarized field of sufficiently high gain is required. None of the geometries considered produces a circularly polarized field with a single dipole, monopole or slot excitation alone. A combination of these excitations would have to be employed to achieve the required result. The gain requirement, on the other hand, would not be that difficult to achieve since most of the configurations have sufficiently high gain, with the exception of the slotted cylinder. Hence, an array of the exciting

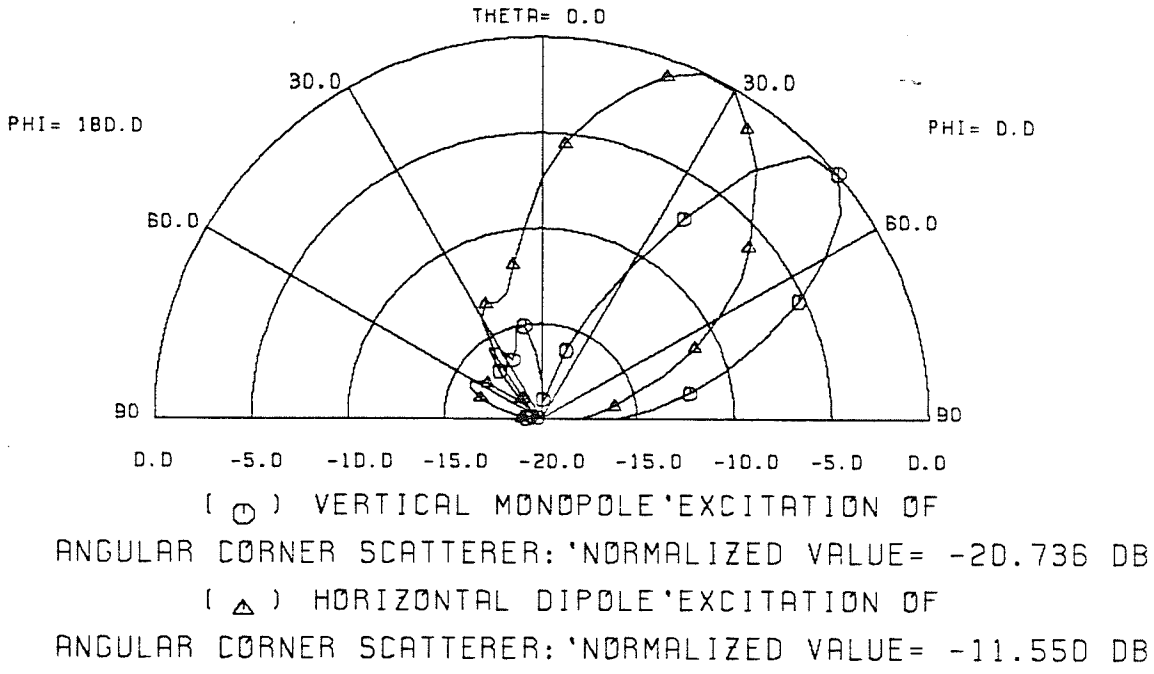

Figure 3.10: Far field patterns for an angular corner reflector due to horizontal dipole and vertical monopole excitations

elements should produce the required amount of gain.

The problem anticipated in the array analysis for the geometries considered is the placement of the horizontal and vertical excitation sources when a finite ground plane is employed. This was apparent from the peak pattern shifts for the various ground plane radii. For the mobile configuration, the size of the ground plane may not be a variable design parameter since it is determined by the roof size of the vehicle. Hence, the control of the beam peak location by this variable could not be taken advantage of.

The monopole excitation for the various scatterers produces the best results in terms of the directivity of the far fields and hence has good potential for further array analysis. The horizontal dipole excitation on the other hand, needs to be analyzed further, since the current configuration does not produce the required far field pattern.

The slotted cylinder configuration also has potential for further analysis but it is anticipated that the array may not have the required gain.

The configuration which would have the best potential for further analysis would be that using the conical scatterer with an appropriate excitation. The term 'appropriate' is used since the horizontal dipole excitation did not produce the required beam peak location and since the vertical monopole resultant beam peak orientation produces a linearly polarized field whose beam peak is dependent on the ground plane size. If a source could be placed parallel to the surface of the cone, and if this source could radiate a circularly polarized field in a broadside direction to the conical surface, the aforementioned problems are rectified. This premise lead to the selection of a circular microstrip patch antenna, operating in its dominant mode, and placed on a conical surface.

CHAPTER 4

THEORETICAL ANALYSIS AND PERFORMANCE OF THE CONICAL PATCH ANTENNA

4.1 Introduction

From the studies performed in Chapter 3, and with the knowledge of the types of single elements previously proposed, the circular patch microstrip antenna was selected as the array element for the mobile antenna. The decision was based on a number of factors, some of which are not immediately obvious. The primary reason for choosing the patch, however, is the ease with which a beam peak can be generated in the desired elevation region. The radiation pattern of the single patch for dominant mode excitation in combination with a conical supporting structure will produce a beam peak at an elevation angle corresponding to the tilt of the cone. Also, unlike the other single element types studied, which produce either a vertical or horizontal linearly polarized field, the circular patch can be excited to produce a circularly polarized far field. This, in conjunction with its simple geometry, and the fact that a simple feed network can be used, further justifies the choice.

The first three sections of this chapter present an analysis for the single element antenna based on an enhanced cavity model approximation. Included in this analysis is the derivation of the far fields due to two excitation probes. Definitions for the axial ratio, co- and cross-polar components and the directivity of the far field are presented. Coordinate transformations are then generated for an array configuration which can include any number of patch elements in any position. Sections five to seven present the numerical results for the array analysis. This analysis covers two and three active

patches for ten and twelve element configurations. Variations of the geometry are then presented for possible superarray configurations to generate higher gains. The eighth section of the chapter then discusses the feeding arrangement and system control of the array and the chapter concludes by presenting the theoretical and experimental calculations for the input impedance of the single element.

4.2 Enhanced Cavity Model Analysis for a Circular Patch

Many methods have been developed for the analysis of microstrip antennas. The analysis for some of these methods is very straightforward, while for others, very complex. The complexity of the techniques results from the various degrees of approximation made in the modelling of the problem. Bahl and Bhartia [14] present several of the current methods employed. One of the simplest is the cavity model technique. This analysis applies to cavities with ideal open circuit boundary conditions or zero aperture wall admittance and therefore assumes an equivalent magnetic current ring as the only radiating source. In reality, the cavity walls have a finite admittance due to the radiated power. This effect can be modelled by an additional equivalent electric source at the cavity aperture. By complementing the cavity model analysis with this additional equivalent electric current source, the resultant enhanced cavity model technique predicts the far fields very accurately.

The circular patch geometry for the cavity model analysis is shown in Fig. 4.1. The patch becomes a cylindrical cavity with electric walls on the top and bottom and magnetic walls on the periphery. This model results from the assumption that the substrate is electrically thin, i.e. $h < 0.1\ \lambda$, and that only TM fields are dominant in the cavity with the electric field invariant in the z-dimension.

In the analysis, only the solution for the dominant cavity mode is considered. Thus, an excitation source is not explicitly included since for a given excitation, only the particular mode excited will be responsible for the majority of the radiation. Kishk

and Shafai [15] studied the effect of the feed position on the excitation efficiency of the dominant mode. Their results show that for any feed position, the maximum relative power of the dominant mode is always at least 24 dB greater than the next excited mode.

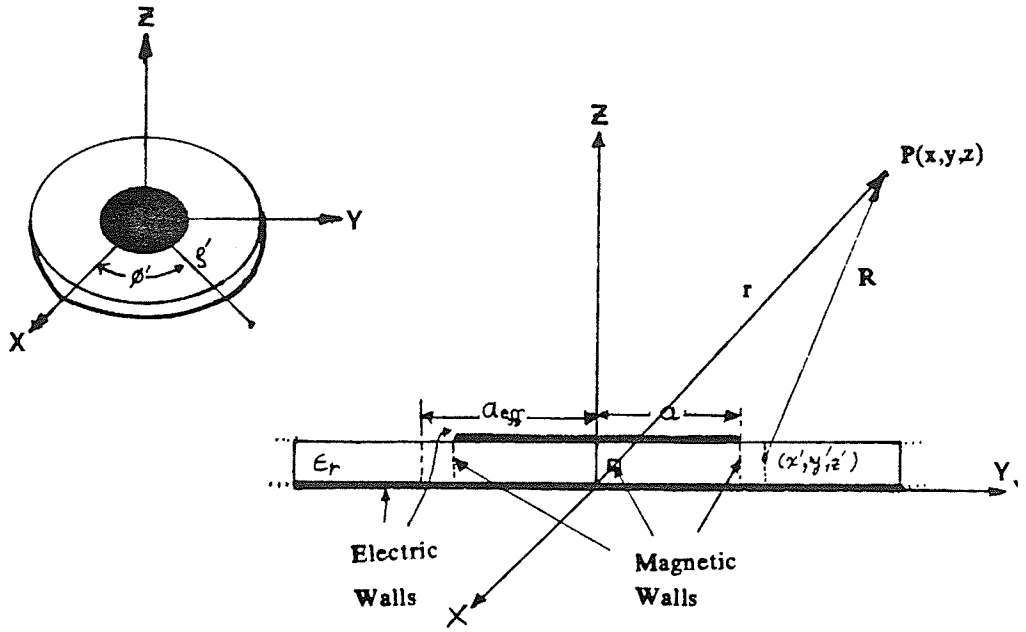

Figure 4.1: The circular patch antenna geometry

Assuming time harmonic fields, the time variation represented by $e^{j\omega t}$ will be implicit in all of the following analysis. The boundary value problem considered is defined as follows:

$$(\nabla^2 + k_d^2) E_z = 0, \quad 0<\rho<a, \quad 0<\phi<2\pi, \quad 0<z<h \tag{4.1}$$

subject to, $\hat{n}\times\vec{H} = 0$ at $\rho = a$ where,

$$\hat{n} = \hat{a}_\rho$$

$$k_d^2 = \omega^2 \mu_o \varepsilon_o \varepsilon_r,$$

$$\nabla^2 = \frac{1}{\rho} \frac{\delta}{\delta\rho} (\rho \frac{\delta}{\delta\rho}) + \frac{1}{\rho^2} \frac{\delta^2}{\delta\phi^2}.$$

The separation of variables technique is now employed to generate two Sturm-

Liouville systems, one for the ϕ-variable, and one for the ρ-variable. The Sturm-Liouville system for the ϕ-variable is periodic with symmetry about $\phi=0$. The Sturm-Liouville system for the ρ-variable turns out to be Bessel's differential equation. The general solution to the problem is then the product of the two general solutions, namely

$$E_z(\rho,\phi,z) = [\frac{C_n}{\sqrt{\pi}} \cos n\phi + \frac{D_n}{\sqrt{\pi}} \sin n\phi\ ]\ [\frac{S_{nm}}{N_n} J_n(k_{nm}\rho) + \frac{T_{nm}}{N_n} N_n(k_{nm}\rho)]$$

$$n > 0,\ m > 0 \qquad (4.2)$$

where C_n, D_n, S_{nm} and T_{nm} are constants and N_n is a normalizing factor. Applying regularity conditions for symmetric and bounded solutions, i.e. for $\phi=0$ and $\rho=0$, the solution for the vertical field E_z becomes,

$$E_z\ (\rho,\phi,z) = \frac{C'_n}{\sqrt{\pi}N_n} \cos n\phi\ J_n(k_{nm}\rho) \qquad n > 0,\ m > 0 \qquad (4.3)$$

where, C'_n= a constant, and

N_n= a normalizing factor for the Bessel function, where

$$N_n^2 = \int_0^a \rho\ [J_n(k_{nm}\rho)]^2\ d\rho \quad = \frac{1}{2}[a^2-(\frac{n}{k_{nm}})^2\ ]\ [J_n(k_{nm}a)]^2$$

The final step in the solution process to determine the eigenvalues k_{nm}, involves the application of the boundary condition,

$$\hat{a}_\rho \times \vec{H} = 0 \ \text{ or } \ \frac{1}{j\omega\mu_o}\frac{\delta E_z}{\delta\rho} = 0 \ \text{ at } \ \rho = a$$

Performing this partial derivative on (4.3) results in the following eigenvalue equation,

$$J_n'(k_{nm}a) = 0 \qquad (4.4)$$

Hence, the problem will have a solution at each zero m of the derivative of the Bessel function of order n. These define the possible modes of operation of the circular microstrip patch antenna whose relative magnitudes are determined by the excitation

source. Equation (4.3) in conjuction with (4.4) defines a solution to the stated problem.

As stated earlier, the far fields will be comprised of the fields due to an equivalent magnetic source and an equivalent electric source. The equivalent magnetic source is obtained by applying the boundary condition

$$\vec{M} = \frac{2}{\mu_o}(\vec{E}_z \times \hat{n}) \,, \quad \hat{n} = \hat{a}_\rho \quad \text{at } \rho = a$$

$$\text{which yields,} \qquad \vec{M} = M_\phi \hat{a}_\phi = 2E_o J_n(k_{nm})\cos n\phi \;\; \hat{a}_\phi \tag{4.5}$$

where $E_o = \dfrac{C'}{\sqrt{\pi N_n}}$ and C' is an arbitrary constant. The equivalent electric source is obtained in a similar fashion to (4.5) but replaces the magnetic field at the patch periphery. It is obtained by applying the following condition

$$\vec{J} = 2\,(\hat{n} \times \vec{H}) \;\; , \hat{n} = \hat{a}_\rho, \;\; \text{at } \rho = a$$

yielding, $\vec{J} = J_z \hat{a}_z = 2H_\phi \;\; \hat{a}_z$ and $H_\phi = - y_a E_z$ at $\rho = a$ such that

$$J_z \hat{a}_z = - 2y_a E_o J_n(k_{nm}\rho)\cos n\phi \;\; \hat{a}_z \tag{4.6}$$

where y_a is the boundary wall admittance of the cavity. This quantity can be obtained from either the far field quantities as defined by Shen [16] or from the near field quantities as defined by Bhattacharyya [17]. The expressions from the latter reference were employed since numerical data for $y_a = g_a + jb_a$ was available. As given in [17], the expression for the wall conductance for the n^{th} mode is

$$g_a = \frac{ah}{2\pi\omega\mu_o}\int_0^{2\pi} \frac{\cos(n\alpha)}{r^3}\left[\left(1+\cos^2\left(\frac{\alpha}{2}\right)\right)(\sin(kr) - kr\cos(kr)) + \right.$$

$$\left. - k^2r^2\sin^2\left(\frac{\alpha}{2}\right)\sin(kr)\right] d\alpha \tag{4.7}$$

where $r = 2a \sin\dfrac{\alpha}{2}$ and k is the free space wavenumber. The susceptance, b_a, for electrically thin substrates was also obtained from [17] and is given for the n^{th} mode

by

$$b_a = \omega\varepsilon_o\varepsilon_r\Delta a(1 - \frac{n^2}{k_d^2 a_{eff}^2}) \tag{4.8}$$

$$\text{where, } \Delta a = a_{eff} - a = a\,(\sqrt{(1+\Delta)}-1)$$

$$\text{and, } \Delta=2\frac{h}{\pi\varepsilon_r a}[\ln(\frac{a}{2h}) + \varepsilon_r(1.41+0.268\frac{h}{a})+3.42]$$

Here, a_{eff} is the effective radius of the patch, and ε_r is the relative dielectric constant of the substrate.

The electric and magnetic vector potentials can now be appropriately generated from the equivalent magnetic and electric sources, respectively. In the far field, only transverse field components exist, that is, transverse to the radial direction of propagation. Hence, the two transverse field components are determined in terms of each of the vector potentials by,

$$E_\theta^m = -jk_oF_\phi, \qquad E_\theta^e = j\omega\mu_oA_\theta$$

$$E_\phi^m = jk_oF_\theta, \qquad E_\phi^e = 0$$

where F_ϕ and F_θ are the electric vector potentials and A_θ is the magnetic vector potential. The total far fields are simply the summations of the respective components. Appendix A presents the definitions for the vector potentials along with the derivations of the transverse components for a general TM_{nm} mode excitation.

For dominant mode excitation, n=m=1, the eigenvalue equation yields a value of $k_{11}a$= 1.84118 for its argument and the expressions for the far fields, as derived in Appendix A become

$$E_\theta^1\,(r,\theta,\phi) = f(\theta)\,e^{j\alpha_1}\cos\phi \tag{4.9}$$

$$\text{and, } E_\phi^1(r,\theta,\phi) = g(\theta)\,e^{j\alpha_1}\sin\phi \tag{4.10}$$

where

$$f(\theta) = E_o k_o h a J_1(k_{11}a)\,\frac{e^{-jk_o r}}{r}\Big[\,\eta y_a J_1(k_o a\sin\theta)\,\sin\theta + \frac{j}{2}\big[\,J_2(k_o a\sin\theta) - J_o(k_o a\sin\theta)\,\big]\,\Big]$$

and,

$$g(\theta) = -\,jE_o k_o h a J_1(k_{11}a)\frac{e^{-jk_o r}}{r}\big[\,J_o(k_o a\sin\theta) + J_2(k_o a\sin\theta)\,\big]\,\sin\theta$$

and where α_1 is the phase excitation of feed #1 and η is the free space impedance.

As was discussed in the solution process of the boundary value problem, a symmetrical excitation was implicitly assumed at ϕ=0 degrees. The far field expressions (4.9,4.10) are superscripted with a 1 to indicate this particular excitation position. If one were now to excite the patch at a similar position, but rotated by 90 degrees, the new phi axis corresponds to the y-axis of the previous problem. Hence, ϕ can be replaced by $\phi - \frac{\pi}{2}$ and the following expressions for the far fields due to the second excitation are generated as

$$E_\theta^2 = f(\theta)\sin\phi\, e^{j\alpha_2} \quad \text{and,} \quad E_\phi^2 = -\,g(\theta)\cos\phi\, e^{j\alpha_2}$$

where α_2 is the phase excitation of feed #2. The expressions for the total fields due to the two types of excitation sources can then be obtained from their sum as,

$$E_\theta^t = f(\theta)\,[\cos\phi\, e^{j\alpha_1} + \sin\phi\, e^{j\alpha_2}] \tag{4.11}$$

$$E_\phi^t = g(\theta)\,[\sin\phi\, e^{j\alpha_1} - \cos\phi\, e^{j\alpha_2}] \tag{4.12}$$

By introducing a phase shift of 90 degrees between the two excitations, a circularly polarized field results. This is explicitly shown when α_1 is set to 0 and α_2 is set to 90 degrees, yielding

$$E_\theta^t = f(\theta)e^{j\phi} \quad , \text{ and} \qquad E_\phi^t = -\,j\,g(\theta)e^{j\phi} \tag{4.13}$$

4.3 Definitions for the Axial Ratio, the Co- and Cross-Polar Fields, and the Directivity

To discuss axial ratio, the implicit time variation $e^{j\omega t}$ is utilized since the far field electric and magnetic components oscillate in time phase. The polarization of an electromagnetic field is described in terms of the direction of the electric field in space, where at some distant point, the electric field can be expressed as

$$\vec{E}(r,\theta,\phi,t) = e^{j\omega t}\,[E_\theta\,\hat{a}_\theta + E_\phi\,\hat{a}_\phi] \tag{4.14}$$

where E_θ and E_ϕ are complex quantities in general. Setting $E_\theta = E_\theta' + j\,E_\theta''$ and $E_\phi = E_\phi' + j\,E_\phi''$ where each primed quantity is a real function, the real part of (4.14) is taken to obtain the expression

$$\begin{aligned}\vec{E}(r,\theta,\phi,t) = {} & [E_\theta'\cos\omega t - E_\theta''\sin\omega t]\,\hat{a}_\theta \\ & + [E_\phi'\cos\omega t - E_\phi''\sin\omega t]\,\hat{a}_\phi\end{aligned} \tag{4.15}$$

The above expression has the general form of $A\cos\alpha - B\sin\alpha$, and can be written in another form as

$$\vec{E}(r,\theta,\phi,t) = |E_\theta|\cos(\omega t + \theta_p)\,\hat{a}_\theta + |E_\phi|\cos(\omega t + \theta_q)\,\hat{a}_\phi \tag{4.16}$$

where

$$|E_\theta| = \sqrt{E_\theta'^{\,2} + E_\theta''^{\,2}}$$

$$|E_\phi| = \sqrt{E_\phi'^{\,2} + E_\phi''^{\,2}}$$

$$\theta_p = \tan^{-1}\frac{E_\theta''}{E_\theta'}$$

$$\text{and,} \qquad \theta_q = \tan^{-1}\frac{E_\phi''}{E_\phi'}$$

Now, proceeding in a fashion as described by Elliot [18] to determine the axial ratio, the magnitude of (4.16) is obtained and then its time derivative is taken and set to zero so that its extremum can be found. The resulting extremum, which are separated by 90 degrees, define the major and minor axes of an ellipse. This resulting locus, derived from the movement of the electric vector, is known as the polarization ellipse. It is shown below in Fig. 4.2 along with a definition for the axial ratio.

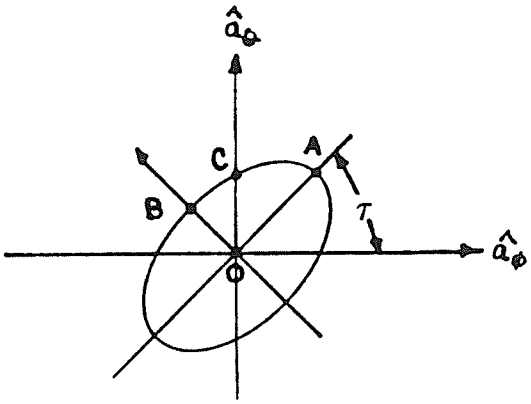

$$\text{Axial Ratio} = \frac{OB}{OA}$$

Figure 4.2: The Polarization Ellipse

Another definition for the axial ratio may be based on the co- and cross-polar field components. For example, knowing that the major axis of the polarization ellipse is the combination of the two components while the minor axis equals the difference, the definition is revised as,

$$\text{Axial Ratio} = \frac{E^{co} - E^{x}}{E^{co} + E^{x}} \tag{4.17}$$

where, E^{co} is the co-polar field component, and E^{x} is the cross-polar field component.

Whether the co-polar or cross-polar field components are right or left hand circular polarized depends on which polarization the user receives. Assuming a left hand sense as the primary polarization, the definitions for the co- and cross-polar fields are [5],

$$E^{co} = \frac{A(\theta,\phi)}{\sqrt{2}} [\hat{a_\theta} + j\, \hat{a_\phi}]$$

$$\text{and,} \quad E^{x} = \frac{B(\theta,\phi)}{\sqrt{2}} [\hat{a_\theta} - j\, \hat{a_\phi}] \tag{4.18}$$

In terms of the transverse components of 4.16,

$$A(\theta,\phi) = \frac{1}{\sqrt{2}} [\, |E_\theta| e^{j\theta_p} - j\, |E_\phi| e^{j\theta_q}]$$

$$\text{and,} \quad B(\theta,\phi) = \frac{1}{\sqrt{2}} [\, |E_\theta| e^{j\theta_p} + j\, |E_\phi| e^{j\theta_q}] \tag{4.19}$$

In the experimental work that will be presented in Chapter 5, the E-plane patterns are in rotating linear form since the test antenna received fields that were generated by a rotating transmitting horn antenna. The tops of the peaks at any arbitrary elevation angle, represent the major axis of the ellipse as the cross-polar components add to the co-polar ones. Correspondingly, the bottom peak represents the minor axis of the polarization ellipse where the cross- and co-polar components are subtracting. Hence, the ellipticity of the fields at any elevation angle is obtained directly from these rotating linear patterns as the axial ratio (in dB) is simply the difference between the top and bottom peaks. To generate the absolute pattern incorporating only the right or left handed circular polarization, a gain correction factor must be added to the peak gains of the rotating linear pattern. This correction factor was derived by Sroka [19] and is expressed as,

$$\text{Correction Factor} = -3.01 \text{ dB} + 20 \log \left(1 + \frac{1}{10^{\frac{AR}{20}}} \right) \tag{4.20}$$

where AR= the axial ratio(dB) at a particular elevation angle. If a perfectly circularly polarized antenna is used, the AR=0 dB and the resulting correction factor would be 3.01 dB. This correction, in conjunction with the network and terminal losses, is used to convert the rotating linear patterns to absolute gain patterns.

The preceeding discussion on the axial ratio and co- and cross-polar components of the far field is important to the design of a circularly polarized mobile antenna. The satellite transmitted fields are expected to be elliptically polarized with a good axial ratio. As the fields propagate through the ionosphere, they will experience Faraday rotation, that is, the tilt angle of the polarization ellipse will shift. The severity of this shift will be dependent on the ellipticity of the transmitted fields. If the circular polarization is poor, the amount of power intercepted by the receiving antenna is then dependent not only upon the efficiency at which it can extract the required polarization sense, but also on the tilt of the received polarization ellipse. If the transmit and receive tilts match up, maximum power will be extracted, but if they are in quadrature, mimimum power is obtained. Assuming however, that the fields incident on the mobile antenna have an axial ratio less than 1 dB, the amount of power lost due to mismatched tilts will be minimal and hence neglected. The design process will only attempt to keep the axial ratio below 3 dB.

The directivity of an antenna is defined as [18],

$$D(\theta,\phi) \equiv \frac{P_r(\theta,\phi)}{P_T(\theta,\phi)} = \frac{\text{(The radiated power density in a particular direction)}}{\text{(the radiated power density averaged in all directions)}} \tag{4.21}$$

where

$$P(\theta,\phi) = \frac{1}{2}\mathrm{Re}\left\{\vec{E}(\theta,\phi) \times \vec{H}(\theta,\phi)\right\}$$

$$= \frac{1}{2}\mathrm{Re}\left\{E_\theta H_\phi^* - E_\phi H_\theta^*\right\} = \frac{1}{2\eta}\left(\left|E_\theta(\theta,\phi)\right|^2 + \left|E_\phi(\theta,\phi)\right|^2\right) \tag{4.22}$$

and $E_\theta = \eta H_\phi$ and $E_\phi = -\eta E_\theta$ in the far field, with η being the intrinsic impedance of free space ($120\pi\ \Omega$). The total radiated power is given by,

$$P_T(\theta,\phi) = \frac{1}{4\pi r^2}\int_0^{\pi}\int_0^{2\pi} P(\theta,\phi) r^2 \sin\theta \, d\phi \, d\theta \tag{4.23}$$

$$\text{Thus, } D(\theta,\phi) = 4\pi \frac{\left|E_\theta(\theta,\phi)\right|^2 + \left|E_\phi(\theta,\phi)\right|^2}{\int_0^{\pi}\int_0^{2\pi}\left[\left|E_\theta(\theta,\phi)\right|^2 + \left|E_\phi(\theta,\phi)\right|^2\right]\sin\theta \; d\phi \, d\theta} \tag{4.24}$$

For the numerical results presented in this thesis, the integrals were replaced by finite sums with $\Delta\theta_n$= 5 degrees, and $\Delta\phi_n$= 3 degrees,

$$D(\theta,\phi) = 4\pi \frac{\left|E_\theta(\theta,\phi)\right|^2 + \left|E_\phi(\theta,\phi)\right|^2}{\sum_{m=1}^{360}\sum_{n=1}^{181}\left[\left|E_\theta(\theta,\phi)\right|^2 + \left|E_\phi(\theta,\phi)\right|^2\right]\sin\theta_n \, \Delta\theta_n \, \Delta\phi_n} \tag{4.25}$$

4.4 Coordinate Transformations for the Array

The expressions for the far fields obtained in Section 2 were generated with respect to a single element's associated coordinate system. For array analysis, particularly for a symmetric ring array geometry, the contribution from each element at a distant point may be summed up and expressed in array factor form. For an arbitrary placement of the elements, on the other hand, a method based on a transformation of coordinates is necessary in general. This latter approach was employed in generating the fields from a conical array of circular microstrip patch antennas.

Assuming a global coordinate system at some origin (0,0,0) with respect to several element local coordinate systems, as shown in Fig. 4.3, the method employed in generating the total fields can be summarized in the following four steps:

[1] The position of each local coordinate system with respect to the global coordinate system is given in terms of a pitch-yaw-roll rotation (ψ_p,ψ_y,ψ_r), and a translation (r_t,θ_t,ϕ_t) where

ψ_p = the pitch angle rotation

ψ_y = the yaw angle rotation

ψ_r = the roll angle rotation

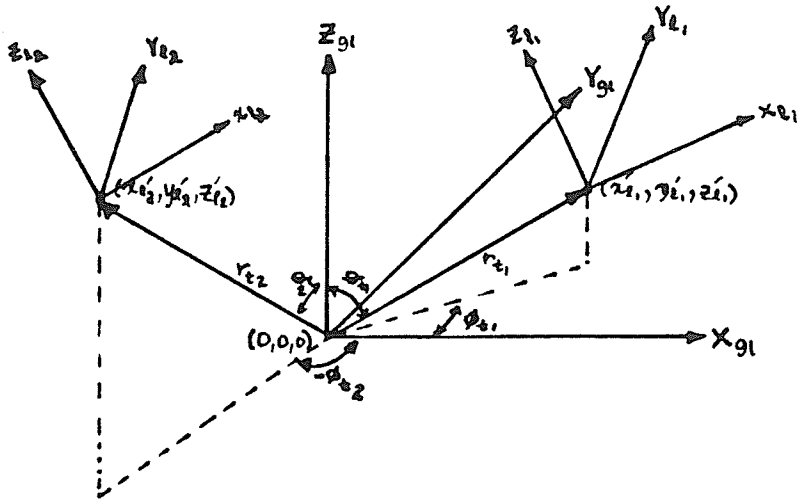

Figure 4.3: Global-Local Coordinate System Orientations

r_t = the radial translation distance

θ_t = the elevation translation angle

ϕ_t = the azimuthal translation angle.

The transverse far field components with respect to each of the individual element's local coordinates are then generated.

[2] The transverse far field components for each individual element are converted to the local coordinate system's Cartesian components by using the appropriate direction cosines,

$$\vec{E} = E_\theta \, \hat{a}_\theta + E_\phi \, \hat{a}_\phi$$

Then for the l^{th} element,

$$E_{x_l} \, \hat{a}_{x_l} = E_\theta \, (\hat{a}_\theta \cdot \hat{a}_x) + E_\phi \, (\hat{a}_\phi \cdot \hat{a}_x) \qquad (4.26)$$

$$= E_\theta \cos\theta_l \cos\phi_l - E_\phi \sin\phi_l$$

$$E_{y_l} \, \hat{a}_{y_l} = E_\theta (\hat{a}_\theta \cdot \hat{a}_y) + E_\phi (\hat{a}_\phi \cdot \hat{a}_y)$$

$$= E_\theta \cos\theta_l \sin\phi_l + E_\phi \cos\phi_l$$

$$E_{z_l}\,\hat{a}_{z_l} = E_\theta(\hat{a}_\theta \cdot \hat{a}_z) + E_\phi(\hat{a}_\phi \cdot \hat{a}_z)$$

$$= -\,E_\theta \sin\theta_l$$

[3] The local Cartesian components are then converted to the global coordinate system's Cartesian components by an appropriate translation and by a transformation matrix of direction cosines which is denoted by

$$T = \begin{Bmatrix} \alpha_{11} & \alpha_{12} & \alpha_{13} \\ \alpha_{21} & \alpha_{22} & \alpha_{23} \\ \alpha_{31} & \alpha_{32} & \alpha_{33} \end{Bmatrix} \tag{4.27}$$

and whose derivation is given in Appendix B. This transformation matrix takes into account the pitch, yaw, and roll orientation of the individual element coordinate system. For instance, for the l^{th} element,

$$\vec{E}_l = E_{x_l}\,\hat{a}_{x_l} + E_{y_l}\,\hat{a}_{y_l} + E_{z_l}\,\hat{a}_{z_l}$$

with,

$$E_{x_{gl}}\,\hat{a}_{x_{gl}} = E_{x_l}(\hat{a}_{x_{gl}} \cdot \hat{a}_{x_l}) + E_{y_{gl}}(\hat{a}_{x_{gl}} \cdot \hat{a}_{y_l}) + E_{z_l}(\hat{a}_{x_{gl}} \cdot \hat{a}_{z_l})$$

$$= E_{x_l}\alpha_{11} + E_{y_l}\alpha_{12} + E_{z_l}\alpha_{13}$$

$$E_{y_{gl}} = E_{x_l}\alpha_{21} + E_{y_g}\alpha_{22} + E_{z_l}\alpha_{23}$$

$$E_{z_{gl}} + E_{x_l}\alpha_{31} + E_{y_l}\alpha_{32} + E_{z_l}\alpha_{33}$$

where

$$\alpha_{11} = \cos\psi_p \cos\psi_y \cos\psi_r - \sin\phi_y \sin\psi_r$$

$$\alpha_{12} = -\cos\psi_p \cos\psi_y \sin\psi_r - \sin\phi_y \cos\psi_r$$

$$\alpha_{13} = \sin\psi_p \cos\psi_y$$

$$\alpha_{21} = \cos\psi_p \sin\psi_y \cos\psi_r + \cos\phi_y \sin\psi_r$$

$$\alpha_{22} = -\cos\psi_p \sin\psi_y \sin\psi_r + \cos\phi_y \cos\psi_r$$

$$\alpha_{23} = \sin\psi_p \sin\psi_y$$

$$\alpha_{31} = -\sin\psi_p \cos\psi_r$$

$$\alpha_{32} = \sin\psi_p \sin\psi_r$$

$$\alpha_{33} = \cos\psi_p$$

[4] Finally, the transverse far field components with respect to the global coordinate system are obtained by using the appropriate direction cosines between the Cartesian and spherical coordinate systems as in step 2.

$$E_{\theta_{gl}} = E_{x_{gl}} \cos\theta_{gl} \cos\phi_{gl} + E_{y_{gl}} \cos\theta_{gl} \sin\phi_{gl} - E_{z_{gl}} \sin\theta_{gl} \tag{4.28}$$

$$E_{\phi_{gl}} = -E_{x_{gl}} \sin\phi_{gl} + E_{y_{gl}} \cos\phi_{gl} \tag{4.29}$$

4.5 Ten-Element Configuration

In the design of an antenna array, there are usually four parameters that are available for variation, namely the total number of elements, the spatial distribution, the phase excitation and the amplitude excitation. With the exception of the amplitude excitation, which is set to unity for all elements, the remaining three parameters will be varied in the design process at hand.

The top and side views for the ten-patch array as well as the defining parameters of the array are shown in Fig. 4.4.

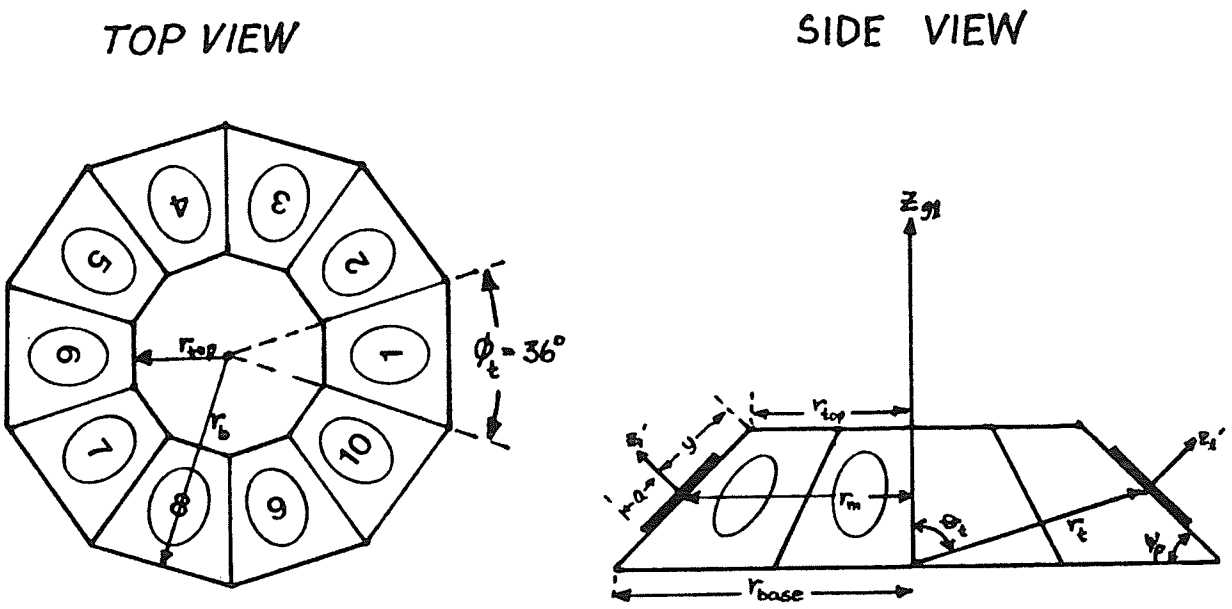

Figure 4.4: Geometry and definition of a ten-element array

In defining the geometry, various restrictions were placed on the parameter values. First, the patch centers were spaced by 36 degrees since the ten elements span 360 degrees. Then, the minimum allowable distance from the patch center to the ground (θ= 90 degrees) denoted by y, was set to a value corresponding to the physical radius of the patch plus twice the substrate thickness, i.e. y= a+2h. This was done to allow the effective radiating aperture of the patch to form above the θ= 90 degree plane so

that its primary radiation would be in the upper sphere. As well, if a ground plane is present, the effective radius of the patch must be kept above the ground plane by a minimal distance. In this case, the distance was twice the substrate thickness h. The same holds true for the distance between patch centers in azimuth. In mathematical terms, then, we have the restrictions

$$\text{(i) } r_t \frac{\cos\theta_t}{\sin\psi_p} \leq a + 2h \qquad \text{(ii) } r_t \geq \frac{2(a+2h)}{\phi_t}$$

$$\text{and, } \quad \text{(iii) } \cos\theta_t \leq \sin\psi_p\left(\frac{\phi_t}{2}\right) \tag{4.30}$$

where ψ_p, θ_t, r_t are the pitch angle, translation angle, and translation distance respectively as defined in Section 4.4. The angle ϕ_t is the azimuth translation angle separating the patch centers and is given in radians. For $\phi_t = \frac{\pi}{5}$ (36 degrees), $\psi_p = \frac{\pi}{4}$ (45 degrees), $\varepsilon_r = 2.52$, a=0.18533 λ_o, and h=0.0159 λ_o, the following restrictions must hold

$$\theta_t \leq 77.16 \text{ degrees, and } r_t \geq 0.6377\ \lambda_o \tag{4.31}$$

4.5.1 Two-Element Excitation

The first case considered with the 10-element configuration is with two of the ten elements radiating. For appropriate spacings, the beam peak is expected to occur at an azimuth angle corresponding to $\frac{\phi_t}{2}$ in the horizontal plane, and at an elevation angle corresponding to the tilt angle in the elevation plane. In the simulated results, the two elements were centered about ϕ=0 so that a beam peak would occur in this plane. Moreover, for a circularly polarized wave, one probe of each element is excited with a zero phase excitation, while the second probe is fed a 90 degree phase excitation. Computer optimization of the 2 element excitation was employed in an attempt to

generate the required far field patterns. Table 4 lists the results.

Table 4: 10-Patch 2-Element excitation results

Element Translations		Coverage Area Characteristics						
r_t (λ_o)	θ_t (deg.)	Peak Gain (dBic)	Polar. Angle (deg.)	Max. Azim. Polar BW (deg.) from	to	Worst-Case Azim. Polar BW (deg.) from	to	Ripple Value (dB)
0.650	60.0	9.020	45.0	22.5	67.5	25.0	57.5	0.56
0.700	65.0	9.270	45.0	20.0	70.0	20.0	60.0	0.64
0.724	77.3	9.530	45.0	16.0	74.0	18.0	62.0	0.80
0.800	70.0	9.700	45.0	15.0	75.0	17.5	62.5	0.80
0.800	77.0	9.810	45.0	14.0	76.0	16.0	64.0	0.80
0.900	75.0	10.13	45.0	11.0	79.0	12.5	65.0	0.96
2.500	77.0	10.99	45.0	5.00	85.0	5.0	25.0	7.09

For this case and for the upcoming three-element excitation, the maximum azimuth elevation beamwidth is the 8 dBic beamwidth in the $\phi = 0$ degree plane, whereas the worst case azimuth elevation beamwith is the 8 dBic beamwidth in the $\phi = +/- 18$ degree planes.

With the antenna in free space and a tilt angle of 45 degrees, the beam peak for all orientations occured at the tilt value in the expected azimuth plane, but the required elevation coverage was not achieved for any of the configurations. The peak gain and coverage region increased to a certain point, as the radial translation distance was increased. However, several undesirable characteristics resulted. Besides an increase in the physical size of the array, the ripple value increased and the elevation 8.0 dBic beamwidth decreased causing a shift in the scan volume further out of the required elevation region. Moreover, none of the arrangements investigated with the 2-patch

excitation produced a large enough gain in the specific coverage area. Hence, the two-patch excitation optimization was abandoned and three-element exciation was then considered.

4.5.2 Three-Element Excitation

The expression (4.25) determining the directivity of the antenna was given earlier in the chapter. This gain is considered absolute since losses are not accounted for. Since the gains produced by the 2-patch excitation for a reasonably sized array were not acceptable, an investigation into exciting three of the 10 elements was undertaken. Following the same procedure as for the two-element excitation, many orientations were simulated in the optimization process to find an arrangement which satisfied the outset goals. Table 5 lists the results for the case when each of the three elements are in equal phase excitation.

The results show that an increase in peak gain of up to 1.5 dBic can be obtained with the three-element excitation over that of the two-element excitation. Moreover, the elevation beamwidths in the best and worst-case azimuth planes increased or remained the same. The two most noticable differences were the increase in the ripple value, and the shift in elevation angle of the beam peak. The ripple value increase was below the maximum limit of 2.0 dB but the value of the gain at these minimum points was below the minimum specified value of 10.0 dBic. For radial translations less than or equal to 0.67 λ_o, the beam peak occured at the corresponding tilt angle. For the greater translations, which increased the array size, the beam peak shifted up towards zenith. This shift was 5 degrees for moderate distances and up to 15 degrees for the larger translations. The array factor influence is therefore noticed for base radii greater than 0.93 λ_o.

The other drawback to the larger radial translations is of course the larger array size. The size of the array, as discussed in Chapter two, is to be minimized. A

Table 5: 10-Patch 3-Element excitation results

Element Translations		Coverage Area Characteristics						
r_t (λ_o)	θ_t (deg.)	Peak Gain (dBic)	Polar Angle (deg.)	Max. Azim. Polar BW (deg.) from	to	Worst-Case Azim. Polar BW (deg.) from	to	Ripple Value (dB)
0.650	60.00	10.10	45.0	10.0	72.5	10.0	62.5	0.96
0.700	65.00	10.46	40.0	7.50	80.0	7.50	62.5	1.00
0.724	77.16	10.82	40.0	5.00	80.0	5.00	62.5	1.10
0.800	70.00	11.03	40.0	2.50	82.5	2.50	62.5	1.16
0.825	77.16	11.24	40.0	0.0	82.5	0.00	62.5	1.29
0.900	75.00	11.46	40.0	0.00	85.0	0.00	60.0	1.48
1.500	77.00	12.10	30.0	-7.5	77.5	-7.5	40.0	2.36
2.000	77.00	10.87	25.0	-5.0	57.5	-5.0	25.0	2.97

designer's choice after considering the average size of a vehicle's roof, was to keep the base radius below 1.0 λ_o. At the L-Band center frequency of 1.6 GHz, which corresponds to a wavelength of λ_o= 18.75 cm, the array base becomes 18.75 cm and the total horizontal displacement about 40.0 cm. An optimized geometry which meets the designer's size criterion and part of the coverage area goals is listed in Table 5 as the fifth entry. This geometry with its physical dimensions referenced to the L-Band center frequency, is shown in Fig. 4.5.

The E- and H-plane patterns for this geometry are shown in Fig. 4.6. The elevation E-plane pattern shown is in the plane intersecting the center of the central patch. The resulting far fields retain the smooth broad characteristics of the corresponding field patterns for the single circular patch element. A peak gain of 11.24 dBic in combination with a ripple of 1.29 dB still results in a gain of 9.95 dBic for the worst case

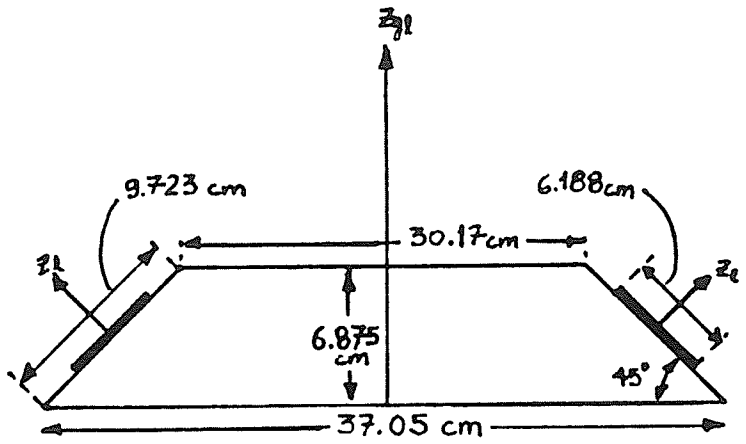

Figure 4.5: Dimensions for the optimized 10-element 3-patch excitation array

H-plane pattern. The 5 degree shift in beam peak to θ= 40 degrees is also acceptable, for the moment, since the position can be controlled by adjusting the tilt angle of the conical supporting structure. Furthermore, the ellipticity of the far fields is nearly perfect, as is shown in Fig. 4.7. This result also reflects the single element's characteristic. Thus, the stated gain values can be continued to be denoted as absolute circularly polarized since no adjustment for the ellipticity is required.

The one characteristic which was below specification is the elevation beamwidth in the worst case azimuth planes, i.e. ϕ= +/- 18 degrees. The beam, for gains greater than 8.0 dBic, extended only to an elevation angle of θ= 62.5 degrees. This signifies that the coverage region for gains greater than 10 dBic is very narrow in terms of the azimuthal coverage. The gain contour plot, shown in Fig. 4.8, supports the latter statement. Without stressing the elevation peak position, the coverage for a minimum gain of 10.0 dBic extended for 18 degrees of elevation in the worst case azimuth planes. In the figure, this occurs between θ= 20 to 38 degrees. Even with the beam peak shifted to a lower elevation angle, the horizontal coverage would not be met.

At this point, it should be noted again that the simulation results are those for an array located in free space. Hence, it is fairly straightforward to adjust the tilt angle of

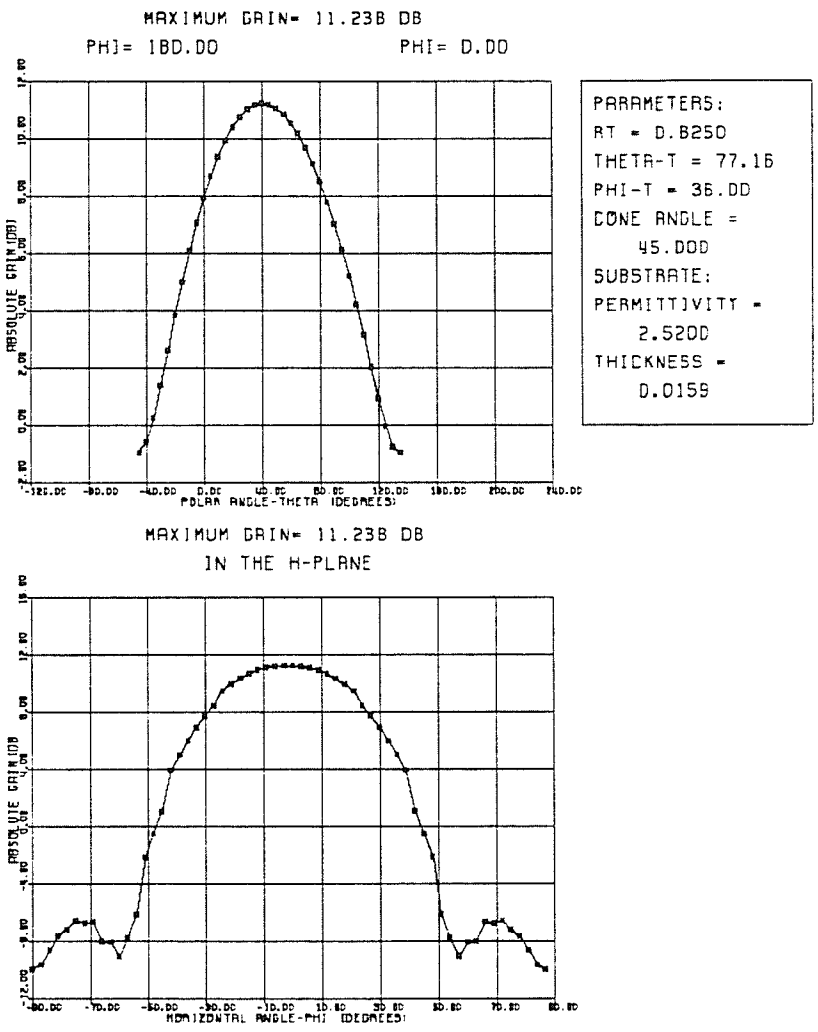

Figure 4.6: Far field radiation characteristics for the optimized 10-element 3-patch excitation configuration

the cone to allow the antenna to radiate with a beam peak in an appropriate elevation direction. With a ground plane, however, such actions may not be necessary. The experimental results included in Chapter 5 will demonstrate this point, as the effects of two different ground plane radii were investigated. The optimization to be done, then, is to obtain a configuration which achieves the required 10.0 dBic for the elemental group azimuth coverage over 25 degrees in elevation. For the 10 element configuration, with three of them active, the group azimuth coverage would be 36 degrees. Intentionally placing the central element at $\phi = 0$ degrees and the adjacent

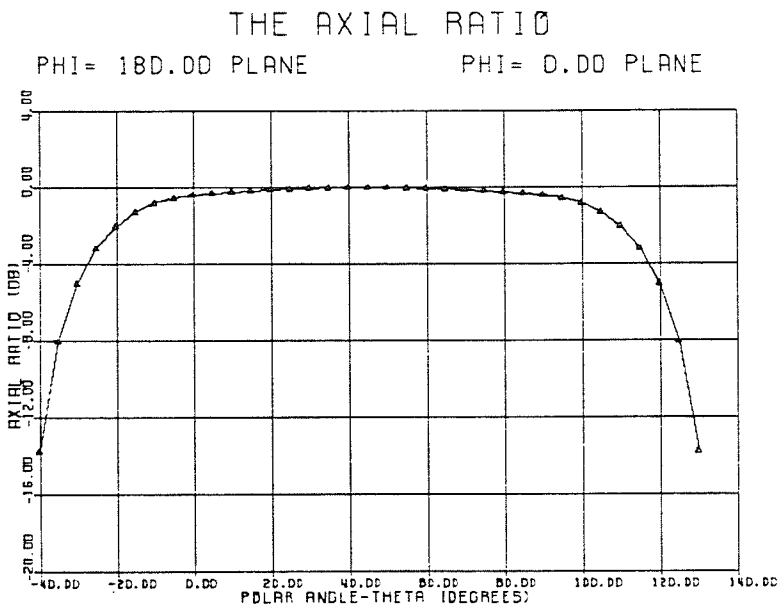

Figure 4.7: Axial ratio for the selected geometry

element centers at ϕ= +/- 36 degrees, the group azimuth coverage sought after is between ϕ= +/- 18 degrees.

In an attempt to improve the coverage and possibly shift the beam peak to a lower elevation region, while keeping the tilt of the array fixed at θ= 45 degrees, phasing of the array elements was studied. The array factor for a ring of N elements is given by Ma [20] as

$$S(\theta,\phi) = \sum_{n=1}^{N} I_n \, e^{[jkr_b\sin\theta\cos(\phi-\phi_n) + j\alpha_n]} \tag{4.33}$$

where r_b= radius of the ring,

I_n= amplitude excitation of the n^{th} element,

ϕ_n = azimuth angle location of the n^{th} element,

and α_n = phase excitation of the n^{th} element.

An introduction of a cophasal excitation between the elements, given by,

$$\alpha_n = -\, kr_b\sin\theta_o\cos(\phi_o - \phi_n) \tag{4.34}$$

should produce a beam peak at elevation and azimuth angles of θ_o and ϕ_o,

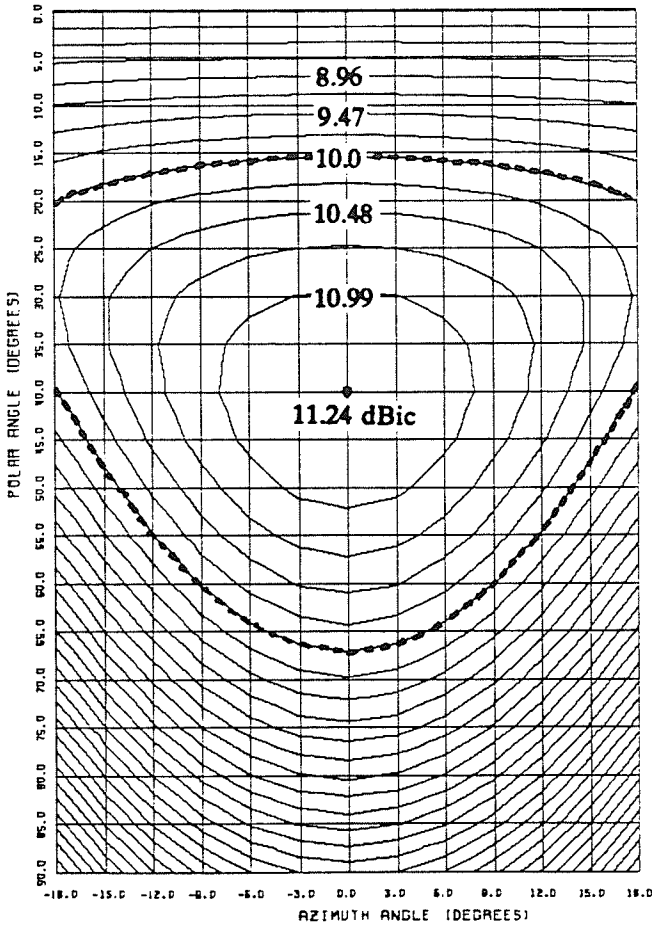

Figure 4.8: Gain contour plot for r_t= 0.825 λ_o and θ_t= 77.16 degrees

respectively. This result is for elements oriented in the same plane. The conical array, on the other hand, has the elements positioned in different planes so that the exact results dictated by the array factor with cophasal excitation are not to be expected in general. However, the cophasal excitation should still produce the desired beam shift behavior. In an attempt to increase the worst case azimuth coverage for a minimum span in elevation of 25 degrees, the outer two elements of the three element excitation were phased. The central patch was used as the zero phase reference while the outer two elements were excited by appropriate phase differences. Five phase differences were simulated in this way with the results listed in Table 6.

Table 6: 10-Patch 3-Element excitation results with phase differences

Element Translations			Coverage Area Characteristics						
Δ_ϕ (deg.)	r_t (λ_o)	θ_t (deg.)	Peak Gain (dBic)	Polar Angle (deg.)	Max. Azim. Polar BW (deg.) from	to	Worst-Case Azim. Polar BW (deg.) from	to	Ripple Value (dB)
22.5	0.825	77.16	11.33	45.0	7.50	82.5	7.50	65.0	1.56
45.0	0.825	77.16	11.36	45.0	7.50	85.0	7.50	67.5	1.58
60.0	0.825	77.16	11.32	45.0	7.50	87.5	7.50	65.0	1.60
90.0	0.825	77.16	11.18	50.0	12.5	87.5	15.0	65.0	1.95
135.0	0.825	77.16	10.94	55.0	17.5	87.5	17.5	62.5	2.08

The greatest improvement was shown by phasing the outer two elements with an additional 45 degree phase shift. The gain increase was only 0.12 dBic, but the beam peak location shifted to θ= 45 degrees and the worst case elevation beam coverage increased to θ= 67.5 degrees. The azimuth coverage, however, did not improve as anticipated. In fact, as the phase excitation was increased beyond 45 degrees, the azimuth coverage area was further degraded. For Δ_ϕ= 45 degrees, for example, the elevation coverage for the minimum value of 10 dBic of gain, decreased to 15 degrees between θ= 27 and 42 degrees. The narrowing of the 10 dBic gain coverage can be seen from Figs. 4.9 and 4.10 which depict the gain contour patterns for the 45 and 90 degree phasing of the two outer elements.

Since variations of the phase excitation for the outer elements did not produce a broadening of the main beam over the required group azimuth coverage, the only alternative left is to phase the elements in a manner such that a beam could be scanned over the required area. At the beginning of the thesis, it was made clear that a phased

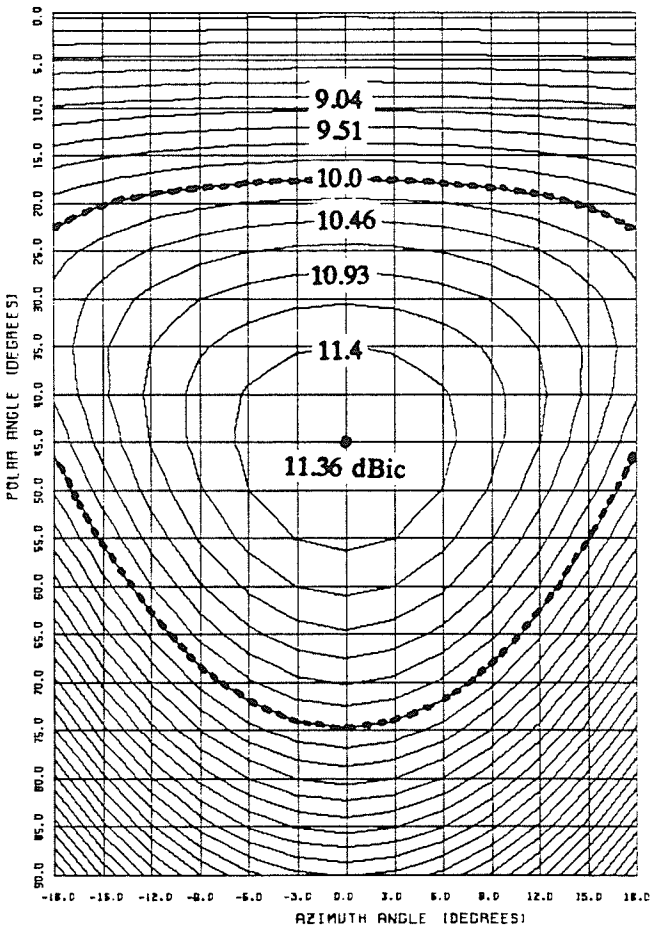

Figure 4.9: Gain contour pattern for $r_t = 0.825\ \lambda_o$, $\theta_t = 77.16$ degrees, and with $\Delta_\phi = 45$ degrees

array design was to be avoided. However, the proposed phase shifting required to make the array meet the design specifications is simple to implement as only single bit phase shifters will be required, and the term 'electronically switchable array' may still be employed.

First, the tilt angle of the cone was increased to $\psi_p = 55$ degrees such that with the elements having equal phase excitation, a beam peak in the $\phi = 0$ degree plane occured at $\theta = 50$ degrees. The resulting far field patterns are similar to those given earlier for $\psi_p = 45$ degrees, but the coverage narrows. As a result of increasing the tilt angle of the array, the spacing between the elements increases. This causes a decrease in the elevation coverage and in the beam peak value. The resulting gain contour

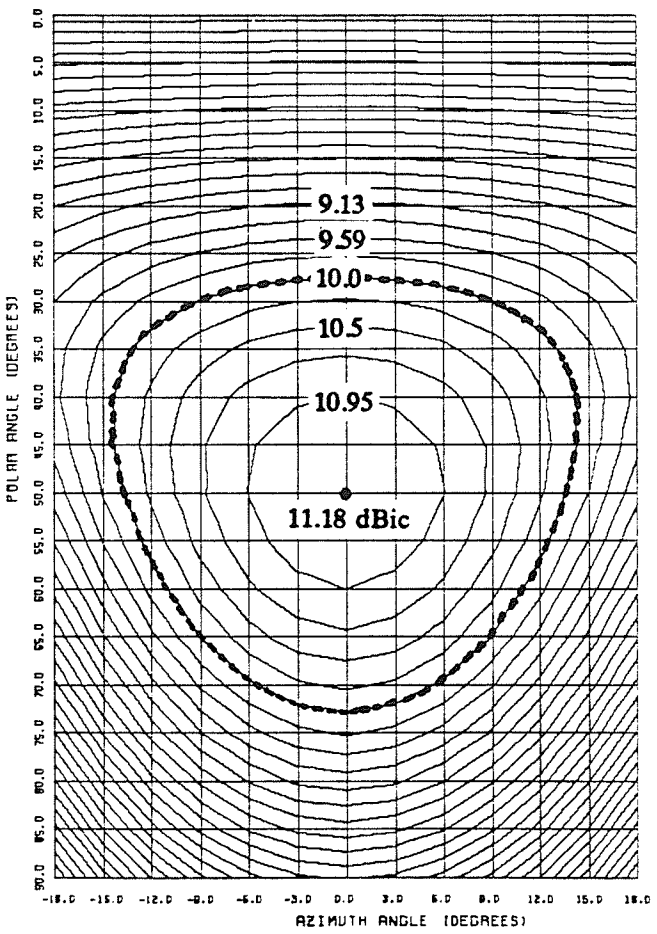

Figure 4.10: Gain contour pattern for r_t= 0.825 λ_o, θ_t=77.16 degrees, and with Δ_ϕ = 90 degrees

pattern is shown in Fig. 4.11. The figure shows that complete coverage for the azimuth region ϕ = +/- 9 degrees is achieved for elevation angles between 27 and 68 degrees. The beam must now be scanned to the left and right of the central patch in order to achieve an azimuth coverage of ϕ = +/- 18 degrees. By switching on an additional 45 degree phase shift to the left element, while keeping the other two elements the same, the resultant beam peak location shifts in azimuth from the ϕ=0 plane to the ϕ = 9 degree plane. Similarly, exciting the right element with the additional 45 degrees of phase excitation, causes the beam peak to shift from the ϕ = 0 to the ϕ = -9 degree plane. The gain contour patterns for the phase switching scheme mentioned are shown

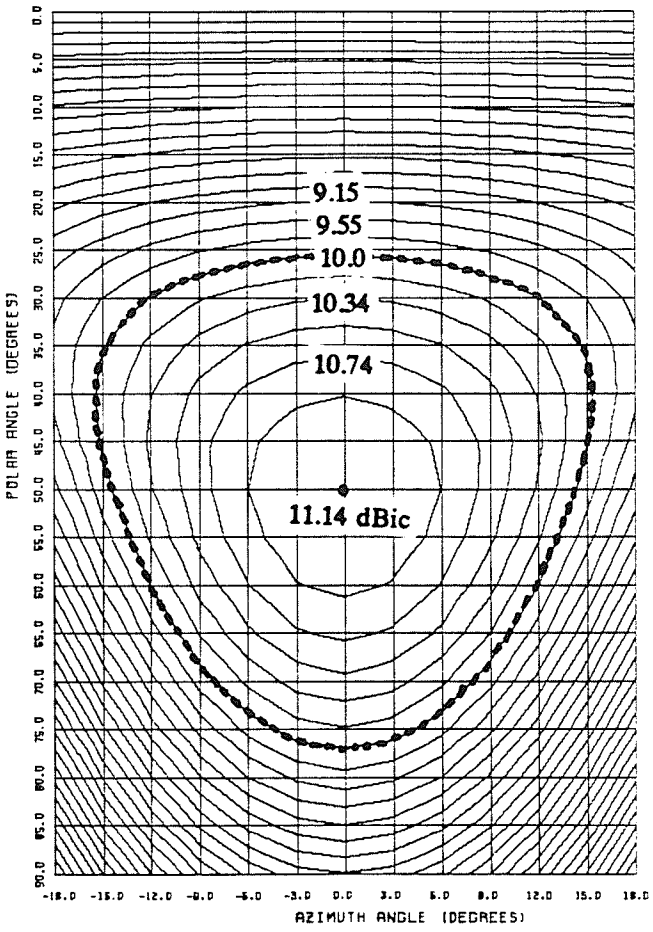

Figure 4.11: Gain contour pattern for r_t= 0.825 λ_o, θ_t= 77.16 degrees, and ψ_p= 55 degrees

in Figs. 4.12 and 4.13.

With this simple phase manipulation, the entire group element coverage region in azimuth and elevation is blanketed with at least the minimum absolute gain of 10 dBic. Two such beams per three element excitation produces the equivalent omnidirectional coverage for the array configuration. Figure 4.14 shows the 10 dBic contours for each of the 20 beams now spanning the global aximuth and elevation regions.

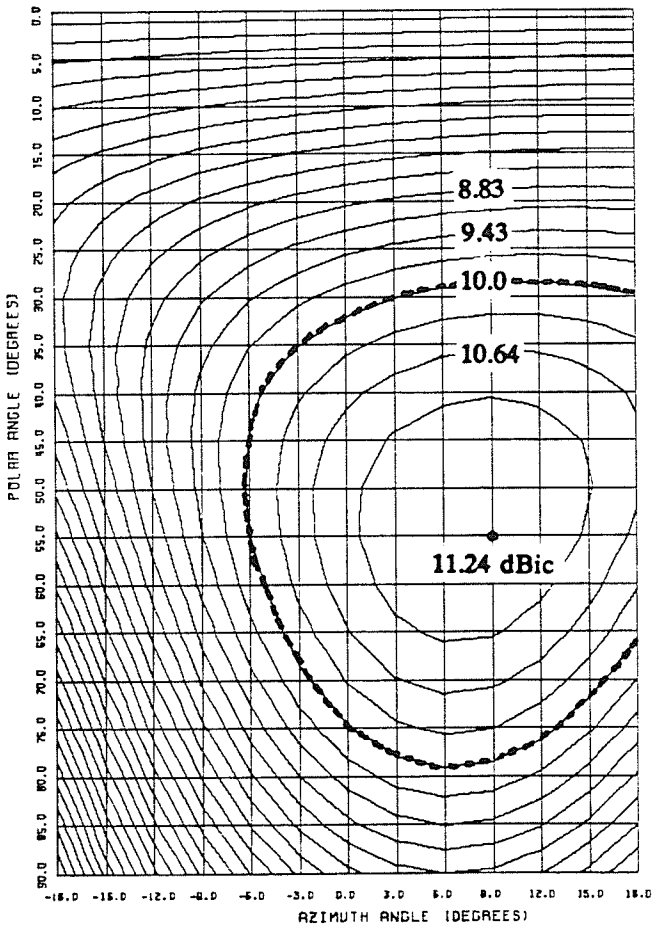

Figure 4.12: Gain contour pattern for r_t=0.825 λ_o, θ_t= 77.16 degrees, ψ_p=55 degrees. amd Δ_ϕ= 45 degrees to the left element

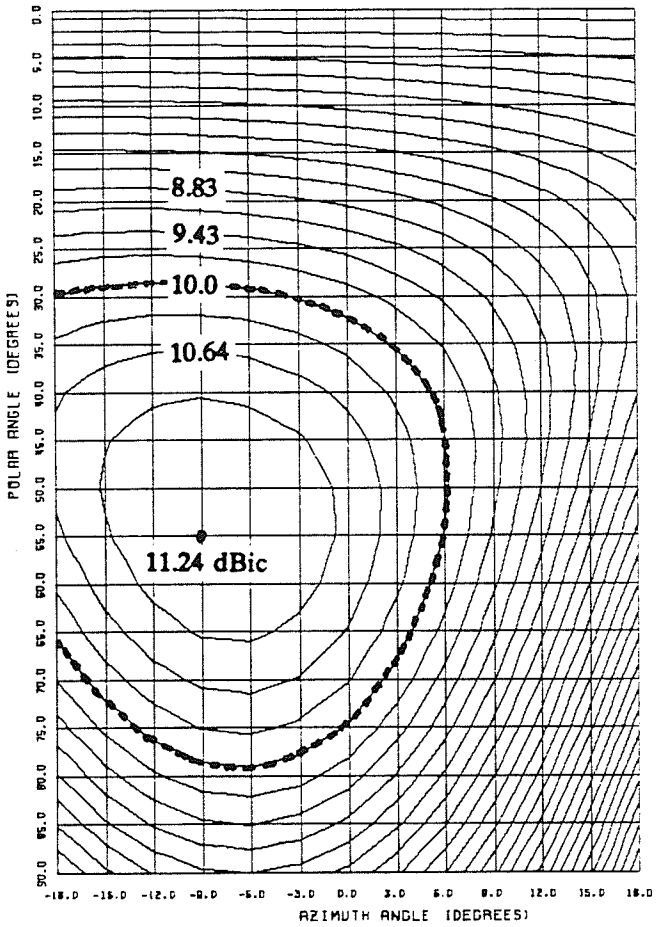

Figure 4.13: Gain contour pattern for r_t=0.825 λ_o, θ_t=77.16 degrees, ψ_p=55 degrees, and Δ_ϕ = 45 degrees to the right element

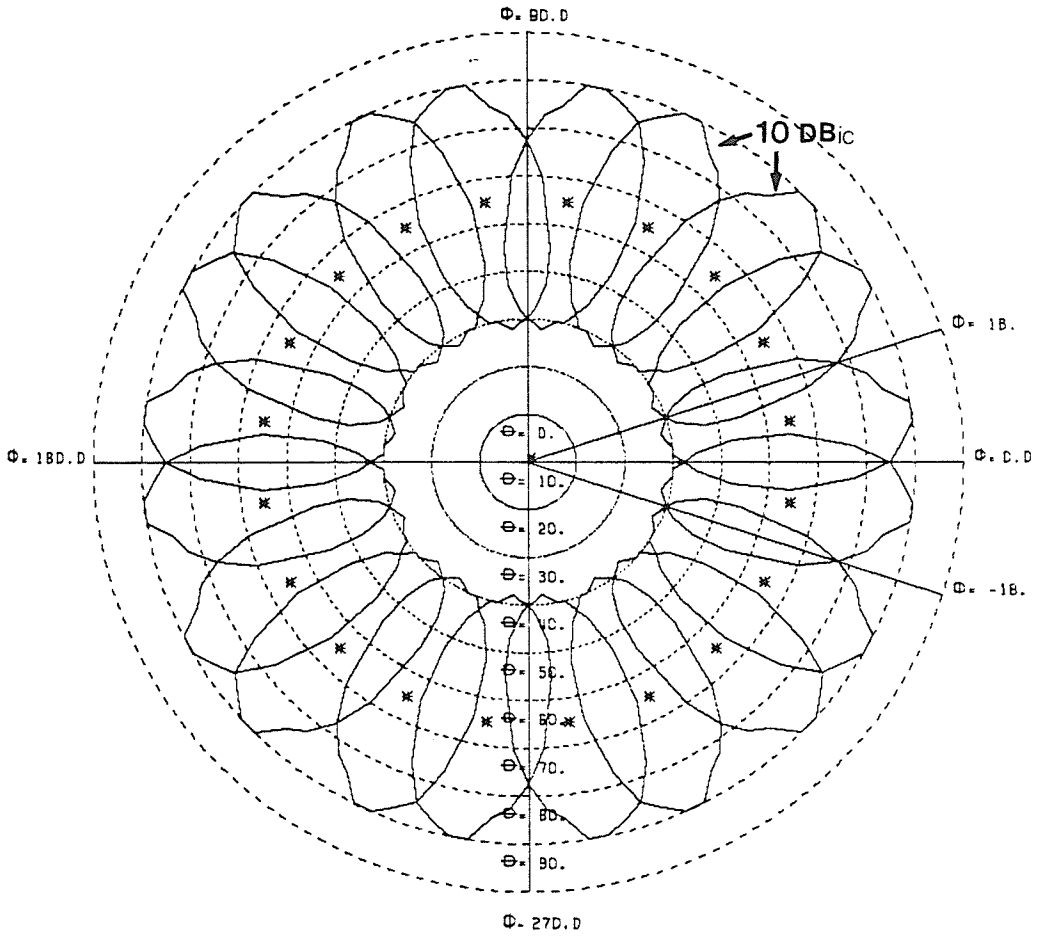

Figure 4.14: Global azimuth coverage for the optimized 10-element, 3-patch excitation configuration

Table 7 lists the required phasing for each of the two array element feeds, required to produce a beam peak in a particular azimuth plane. The element numbers indicated in the table are the same as was shown in Fig. 4.4. The availability of a 0, 45, 90, and 135 degree relative phase excitation is thus required for each probe. Whether the 0 or 90 degree phase inputs, for example, are fed to probes 1 and 2, or 2 and 1, determines the sense of polarization, since the electric vector will be delayed in either the counter clockwise or clockwise sense. A simple feed network for this particular case will be presented in Section 4.8.

Table 7: The required phase switching scheme for omnidirectional coverage

Azimuth	Element No. and Phase Per Probe									
Beam pk. (deg.)	no. 1	no. 2	no. 3	no. 4	no. 5	no. 6	no. 7	no. 8	no. 9	no. 10
9	0,90	0,90	off	off	off	off	off	off	off	45,135
27	0,90	0,90	45,135	off	off	off	off	off	off	off
45	45,135	0,90	0,90	off	off	off	off	off	off	off
63	off	0,90	0,90	45,135	off	off	off	off	off	off
81	off	45,135	0,90	0,90	off	off	off	off	off	off
99	off	off	0,90	0,90	45,135	off	off	off	off	off
117	off	off	45,135	0,90	0,90	off	off	off	off	off
135	off	off	off	0,90	0,90	45,135	off	off	off	off
153	off	off	off	45,135	0,90	0,90	off	off	off	off
171	off	off	off	off	0,90	0,90	45,135	off	off	off
189	off	off	off	off	45,135	0,90	0,90	off	off	off
207	off	off	off	off	off	0,90	0,90	45,135	off	off
225	off	off	off	off	off	45,135	0,90	0,90	off	off
243	off	off	off	off	off	off	0,90	0,90	45,135	off
261	off	off	off	off	off	off	45,135	0,90	0,90	off
279	off	off	off	off	off	off	off	0,90	0,90	45,135
297	off	off	off	off	off	off	off	45,135	0,90	0,90
315	45,135	off	off	off	off	off	off	off	0,90	0,90
333	0,90	off	off	off	off	off	off	off	45,135	0,90
351	0,90	45,135	off	off	off	off	off	off	off	0,90

4.6 Twelve-Element Configuration

The top and side views for a 12-patch array arrangement are given in Fig. 4.15 along with the defining parameters.

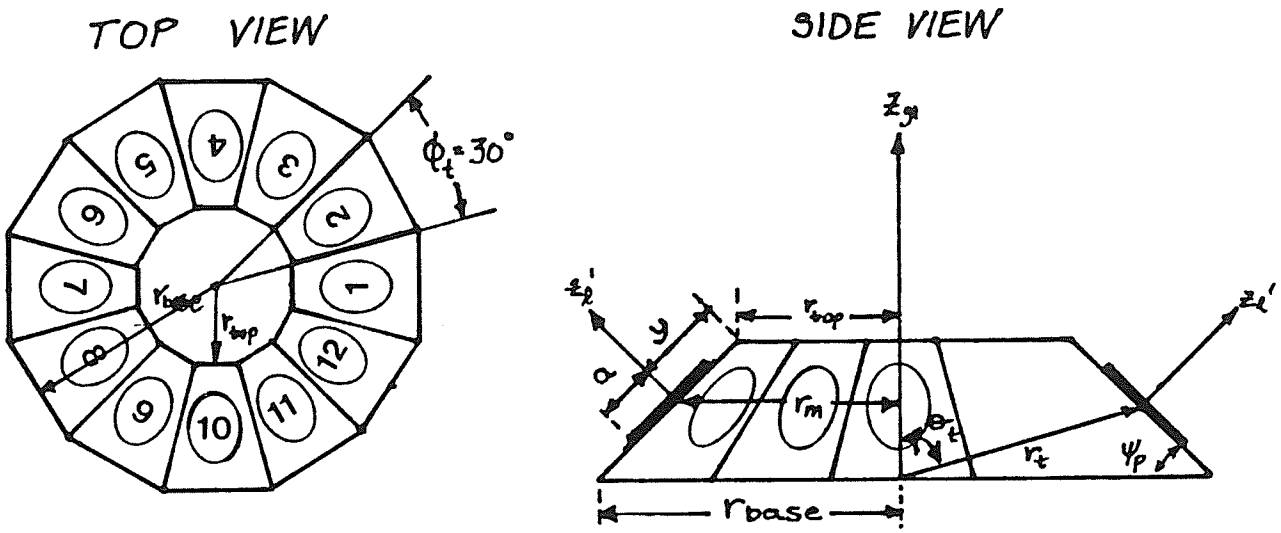

Figure 4.15: Twelve-Element Array Configuration with Defining Parameters

The 12-element configuration has its elements spaced by 30 degrees. The increase in the number of elements increases the number of scanning beams by two over the 10-element case. Hence, the element group scan area is decreased by a total of 6 degrees from $\phi = 36$ to 30 degrees suggesting that complete azimuth coverage may be obtained without any phase switching between elements. The same restrictions on element orientation are imposed for the 12-patch array as for the 10-patch array, with ϕ_t now given by $\frac{\pi}{6}$ or 30 degrees. The resulting numerical values for the translation parameter restrictions are

$$\text{(i) } r_t \geq 0.8294\ \lambda_o \quad \text{and} \quad \text{(ii) } \theta_t \leq 79.33 \text{ degrees.} \tag{4.34}$$

4.6.1 Two-Element Excitation

In this section, the results for two active elements are presented. The elements are separted by ϕ_t= 30 degrees, and are centered about ϕ= 0 degrees so that a beam peak occurs in this same plane. Here, the worst-case azimuth planes correspond to those planes intersecting the patch centers at ϕ= +/- 15.0 degrees. The results for the various spatial orientations are listed in Table 8.

Table 8: 12-Patch 2-Element excitation results

Element Translations		Coverage Area Characteristics						
r_t (λ_o)	θ_t (deg.)	Peak Gain (dBic)	Polar Angle (deg.)	Max. Azim. Polar BW (deg.) from	to	Worst-Case Azim. Polar BW (deg.) from	to	Ripple Value (dB)
0.83	65.00	9.25	45.0	20.0	70.0	20.0	62.0	0.43
0.85	79.33	9.50	45.0	18.0	72.0	20.0	65.0	0.48
0.90	75.00	9.61	45.0	15.0	75.0	20.0	65.0	0.51
1.00	79.00	9.96	45.0	15.0	76.0	15.0	65.0	0.58
1.25	77.33	10.67	45.0	10.0	80.0	10.0	70.0	0.80
1.50	79.00	11.14	45.0	5.0	85.0	5.0	70.0	1.06
2.00	79.00	11.20	45.0	5.0	85.0	5.0	60.0	1.78

In comparison with the 10-element 2-patch excitation results, the peak gains for the current geometry are smaller by an average of 0.5 dBic. The elevation beamwidth in the maximum gain azimuth plane is also smaller in coverage by about 10 degrees, but that in the worst-case azimuth plane is better for most cases. In the horizontal plane, a broader beam was produced, and as expected, the corresponding ripple value

was smaller by 0.4 dB on average.

Increasing the elements' radial and elevation translations increased the peak gain since both translations increase the spacing between the elements. At distances greater than approximately 1.75 λ_o, however, sidelobe beams formed causing radiation of energy into unwanted regions. Moreover, the larger translations decreased the azimuth coverage area, and narrowed the elevation pattern with a modest increase in peak gain. An arrangement was found which produced a pattern covering the horizontal azimuth plane from ϕ= -15 to 15 degrees for 22.5 degrees of elevation. The translations for this geometry are defined by a radial distance of 1.5 λ_o and an elevation angle of 79 degrees. This spaces the patch edges by 7 cm in azimuth, and locates them 3.5 cm above the horizontal ground corresponding to θ= 90 degrees. The gain contour plot for a 45 degree tilt angle is shown in Fig. 4.16. The 10 dBic coverage was quite broad and almost satisfied the 25 degrees of elevation required in the ϕ = +/- 15 degree worst case azimuth planes. The coverage must, however, be shifted to the required elevation regions, between θ= 40 and 65 degrees. To do this, the tilt angle of the cone would have to be increased to ψ_p= 62 degrees.

The two drawbacks associated with this configuration are the array size and the corresponding large cone angle. The radius of the base of the array, again referring to the L-Band center frequency, is approximately 32 cm. In comparison with the 10-element configuration, which has a base radius of 18.75 cm, the former is almost twice as large making it undesirable. Furthermore, the tilt angle necessary to cover the elevation angles between θ= 40 and 65 degrees is too large since the larger angle will further degrade the elevation coverage.

4.6.2 Three-Element Excitation

Since improvements in the field coverage were obtained with the 2-element excitation of the 12-element array, similar results were anticipated for the 3-patch

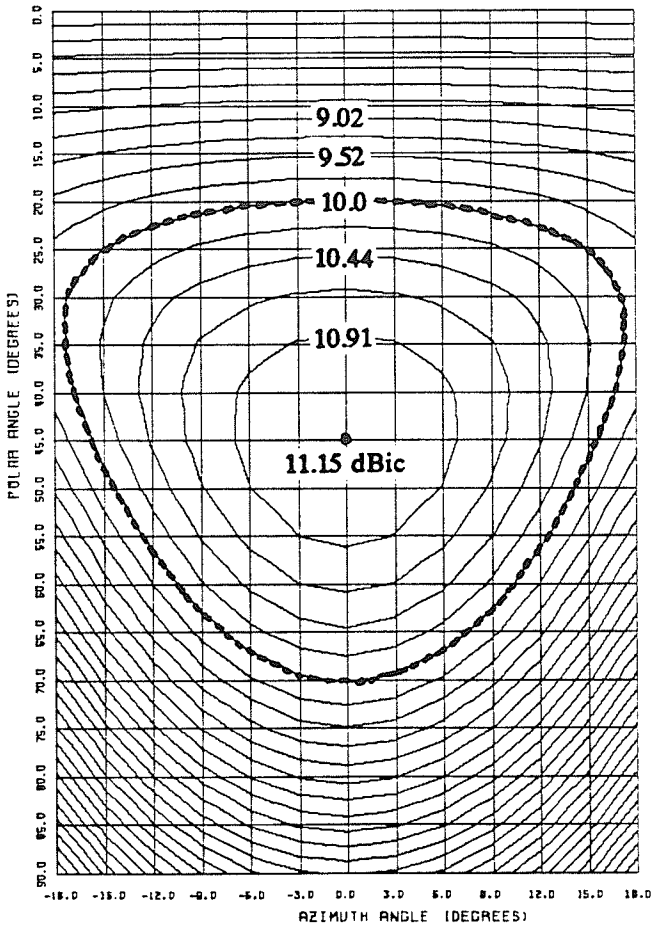

Figure 4.16: Gain contour plot for r_t= 1.5 λ_o, θ_t= 79.0 degrees

excitation. As in Section 4.5, the 3-elements were centered about the ϕ= 0 degree plane and the cone angle was set to θ= 45 degrees. The results from the computer optimization, when each of the elements were phased equally, are listed in Table 9.

The expected changes by exciting the additional element include an increase in peak gain by 1.5 dBic and an increase in elevation beamwidth in the maximum gain azimuth plane. Other differences include an increase in ripple value by about 0.5 dB and a shift in beam peak towards zenith. This shift in beam peak is as much as 15 degrees for the larger translation cases. Hence, the variations in performance follow suit with the 10-element 3-patch excitation.

Table 9: 12-Patch 3-Element excitation results

Element Translations		Coverage Area Characteristics						
r_t (λ_o)	θ_t (deg.)	Peak Gain (dBic)	Polar Angle (deg.)	Max. Azim. Polar BW (deg.) from	to	Worst-Case Azim. Polar BW (deg.) from	to	Ripple Value (dB)
0.83	65.00	10.49	45.0	7.50	80.0	7.50	70.0	0.75
0.85	79.33	10.84	45.0	5.00	82.5	5.00	70.0	0.88
0.90	75.00	10.97	45.0	2.50	82.5	2.50	70.0	0.94
1.00	79.00	11.36	40.0	0.00	85.0	0.00	70.0	0.97
1.25	79.33	11.97	40.0	-5.0	87.5	-5.0	65.0	1.43
1.50	79.33	12.35	40.0	-7.5	87.5	-7.5	57.5	2.01
2.50	79.33	11.06	30.0	-5.0	65.0	-5.0	27.5	3.36

It is apparent from Table 9 that the optimized patch translations for the 2-element excitation are no longer optimal for the 3-element excitation. The geometry which does meet the required criterion is listed as entry 4 in Table 9. The translation parameters are smaller, i.e. r_t= 1.0 λ_o, and θ_t= 79.0 degrees, which correspond to a base radius of 1.17 λ_o or 21.94 cm at the L-Band center frequency of 1.6 GHz. Figure 4.17 presents the far field E- and H-plane patterns for this newly optimized geometry. The ellipticity of the fields is shown by the axial ratio plot of Fig. 4.18.

With this geometry, the peak gain is 11.36 dBic at an elevation angle of 40.0 degrees. These results are very comparable to the 10-element 3-patch excitation results. The overall performance, however, is slightly better as the worst case azimuth coverage is broader, the peak gain higher by 0.12 dBic and the ripple value smaller by 0.3 dB. But again, these improvements are at the expense of a larger structure. In this

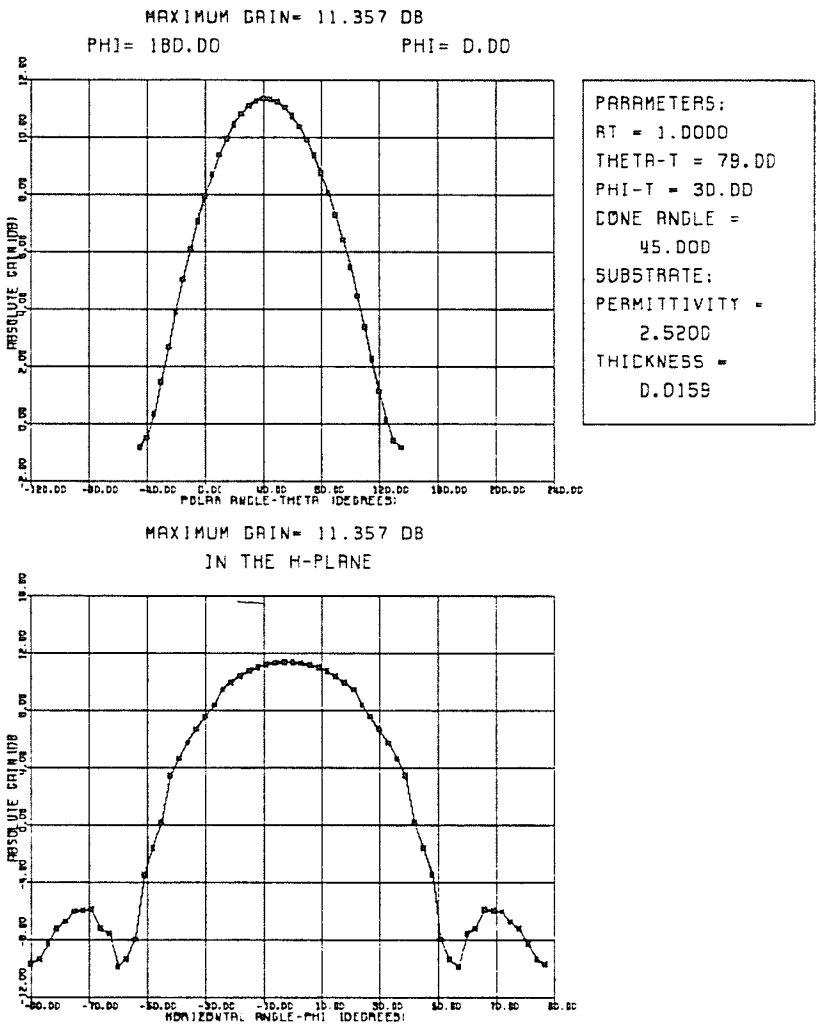

Figure 4.17:Far field characteristics for the optimized 12-element 3-patch excitation

case, the additional horizontal displacement is about 6.5 cm and the vertical height is 0.35 cm larger.

The gain contour plot, given in Fig. 4.19, shows that the fields broaden considerably, especially in comparison to the 2-element excitation. The elevation coverage is extended to 35 degrees over the 30 degrees of the group azimuth coverage. However, in order to shift the coverage between θ= 40 and 65 degrees, it is once again necessary to increase the cone angle to ψ_p= 62 degrees, thereby degrading the elevation coverage. Since the larger tilt angle is not desired, the elements can be phased in the same way as the 10-element array of Section 4.5.2.

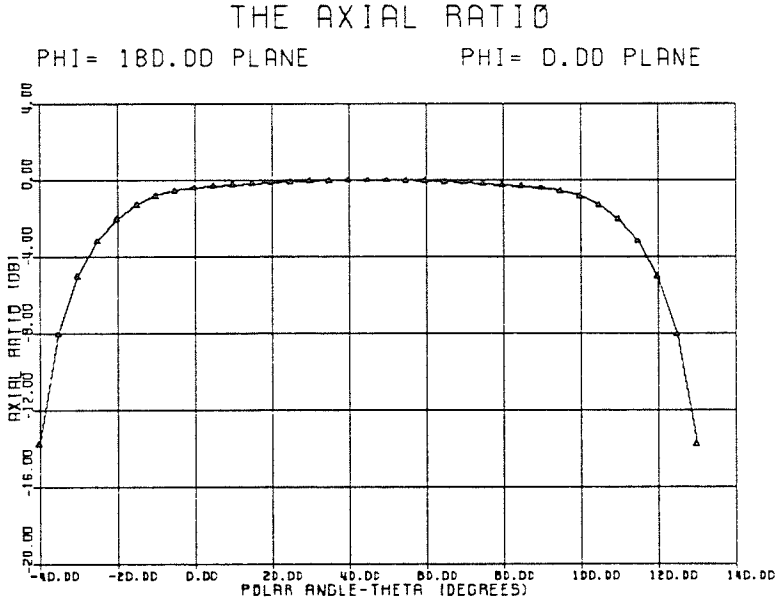

Figure 4.18: Axial Ratio for the optimized 12-element 3-patch excitation

By adjusting the tilt angle of the conical support to ψ_p= 55 degrees, a beam peak at θ= 50 degrees is obtained with azimuth coverage satisfied for elevation angles between θ= 25 to 50 degrees. Proceeding in the same fashion as that presented for the 10-element 3-patch excitation optimization, two beams covering the entire group azimuth and global elevation coverage are obtained when the left and right elements are each phased by an additional 45 degrees of phase excitation. In this case, a shift of 6 degrees in azimuth occurs, as the beam peak relocates to ϕ= 6 degrees for left element phasing, and to ϕ= -6 degrees for right element phasing. The gain contour plots for these two cases are shown in Figs. 4.20 and 4.21.

Moreover, the switching control of the phase excitation is the same as that presented in Table 7, Section 4.5.2. The difference is that the two beam peaks are now separated by 12 degrees for each set of three radiating elements. Hence, the first two beam peaks are at +/- 6 degrees, the second set at 36 and 24 degrees and so on. The global azimuth coverage for all 24 beams spanning the horizontal plane are shown in Fig. 4.22.

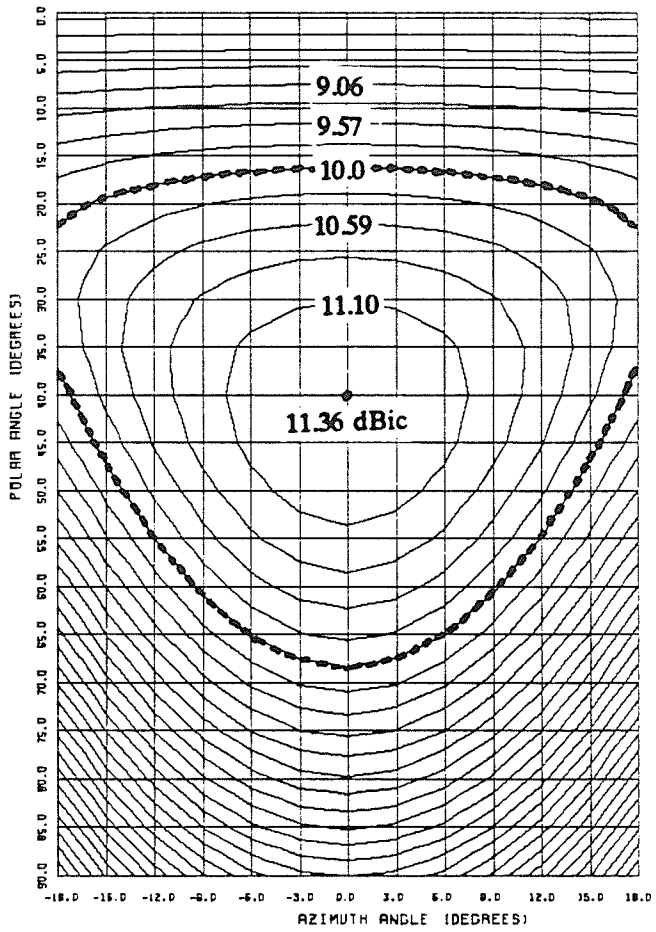

Figure 4.19: Gain contour plot for r_t= 1.0 λ, θ_t= 79 degrees and ψ_p= 45 degrees

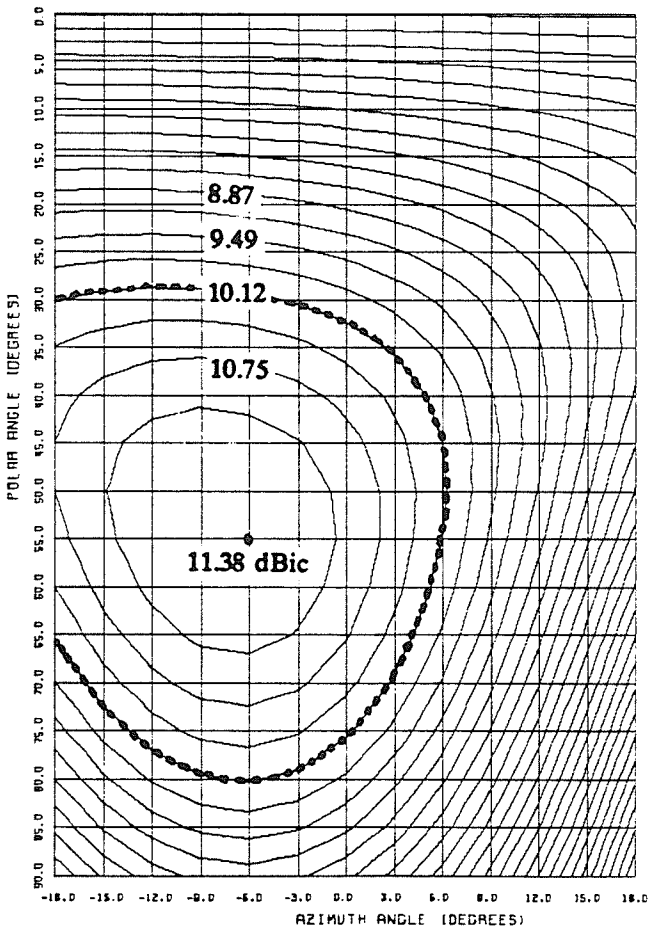

Figure 4.20: Gain contour plot for r_t= 1.0 λ_o, θ_t= 79 degrees, ψ_p=55 degrees and Δ_ϕ= 45 degrees to the right element

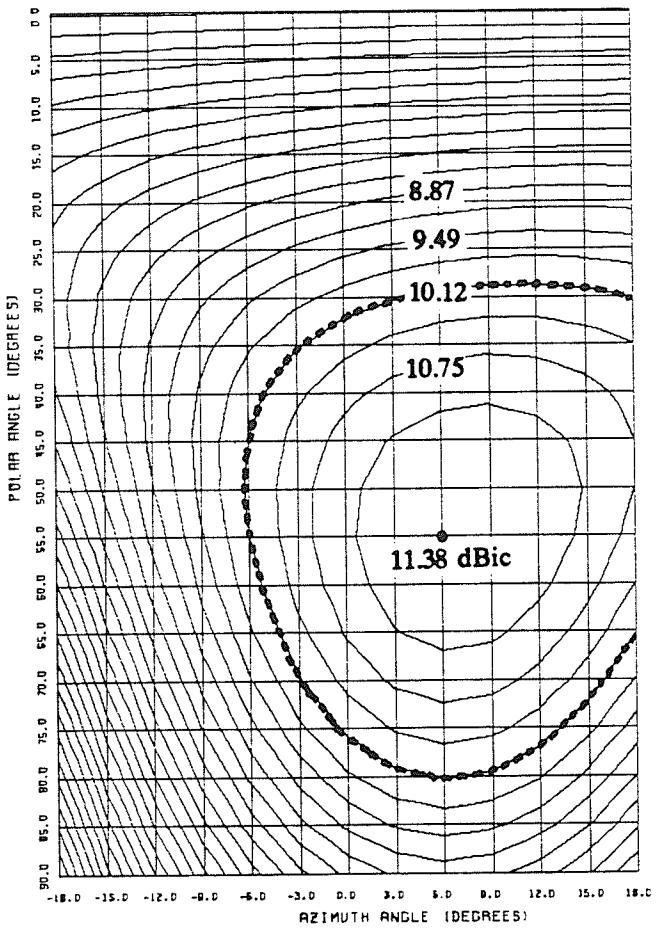

Figure 4.21: Gain contour plot for r_t= 1.0 λ_o, θ_t= 79 degrees, ψ_p=55 degrees and Δ_ϕ= 45 degrees to the left element

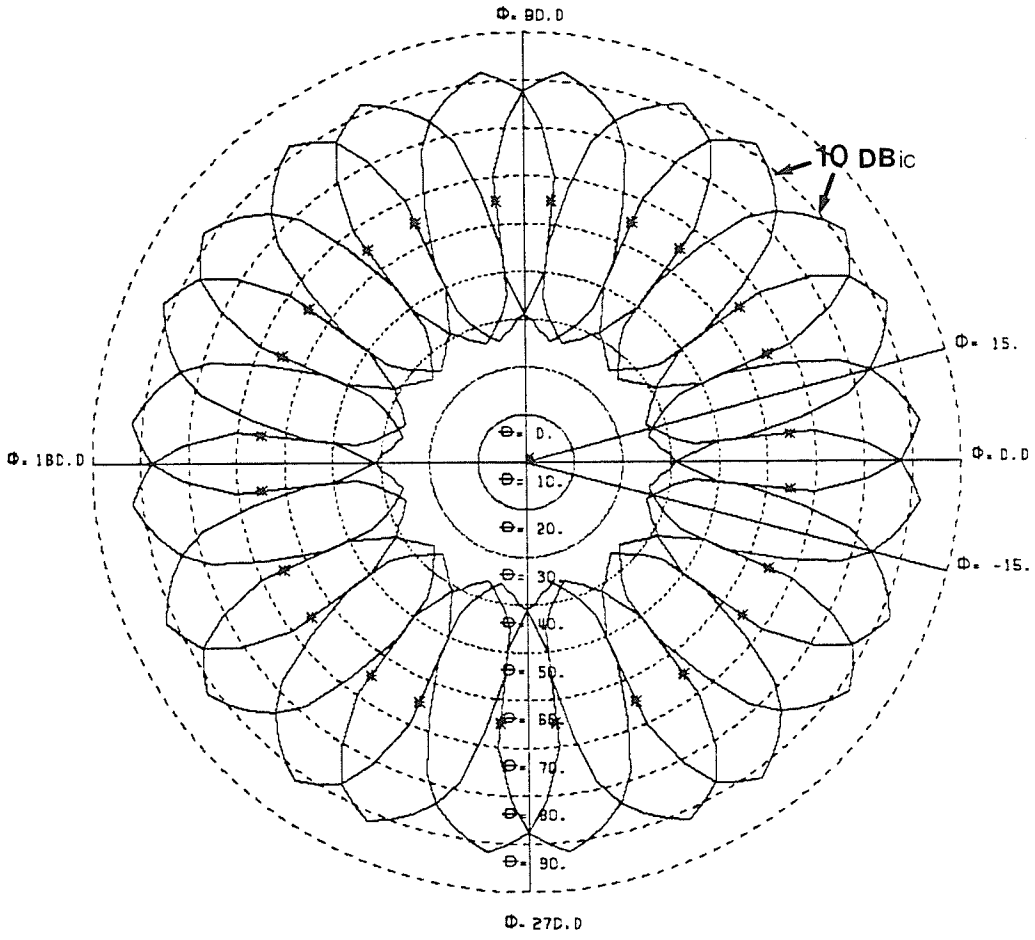

Figure 4.22: Global azimuth coverage for the optimized 12-element 3-patch excitation configuration

4.7 Possible Superarray Configurations

The numerically optimized array configurations presented in the last two sections had peak gains on the order of 11.3 dBic. If higher gains were required over the elevation region, additional elements must be optimally added to the array. The word 'optimal' is used since it would be beneficial to find an arrangement which would not degrade the smooth broadside directed pattern associated with the previously presented array configurations. If degradation does occur, complex phasing of the elements will undoubtedly result if the coverage over the entire azimuth and elevation regions is to be realized. This section presents two possible superarray configurations and the resulting field patterns. All elements are phased equally and no attempt is made to optimize the patterns by phasing the elements since this becomes another design problem. The intent of this section is to show the additional gain generated with the added elements.

The addition of elements to the truncated cone geometry is not a simple one if the size of the array is to be minimized, but two superarray configurations were conceived possible with only a slight increase in array size. The first possibility has the elements placed on the top of the truncated cone with the corresponding pitch angles set to zero. This is shown in Fig. 4.23a. The second possible geometry is to place the additional elements along another conical support on top of the existing array as shown in Fig. 4.23b.

The additional elements must have the same restrictions imposed on them as for the original array of elements, but now, the added elements influence the size of the overall array. New restrictions must therefore be implemented. Denoting the translations for the second array of elements with a subscript 2, and the original element translations with a 1, the following new parameter restrictions must be abided by in the design process,

$$\text{(i) } r_{t_2} = \sqrt{[r_m - (a+2h)\cos\psi_{p_2}]^2 + [(a+2h)(2\sin\psi_{p_1} + \sin\psi_{p_2})]^2}$$

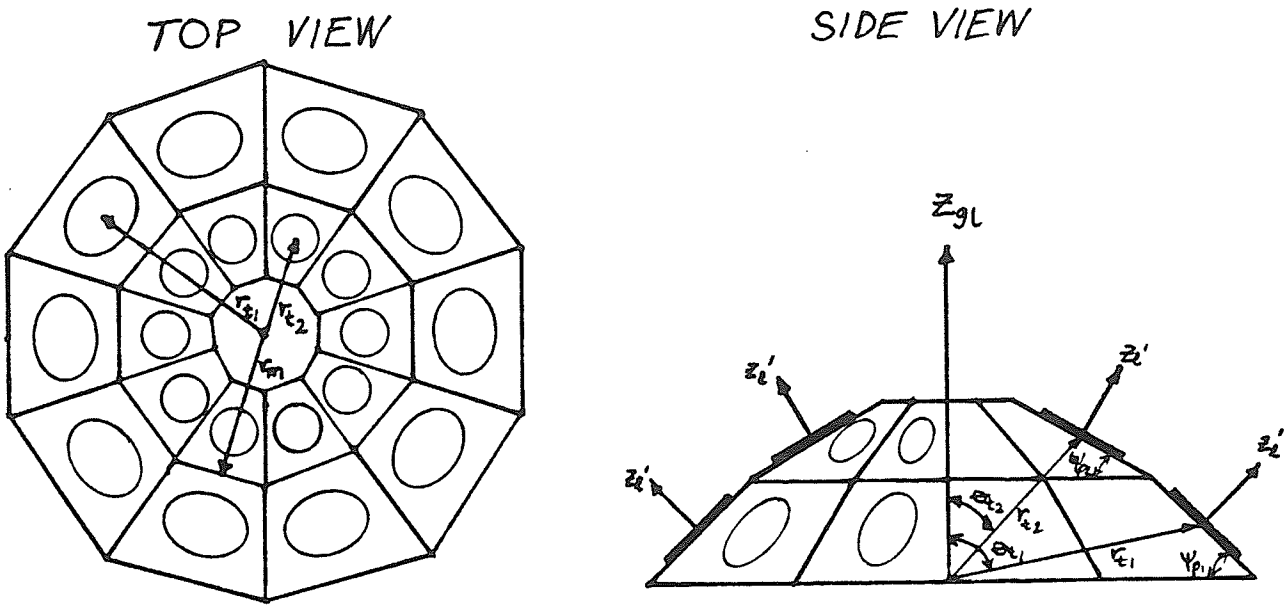

(a) $\psi_{p1}= 45$, $\psi_{p2}= 0$ (b) $\psi_{p1}= 45$, $\psi_{p2}= 22.5$

Figure 4.23: Two possible superarry geometries

$$\text{(ii) } \theta_{p_2} = \tan^{-1}\left[\frac{r_m - (a+2h)\cos\psi_{p_2}}{(a+2h)(2\sin\psi_{p_1} + \sin\psi_{p_2})}\right]$$

$$\text{(iii) } r_{t_1} = \sqrt{[r_m + (a+2h)\cos\psi_{p_1}]^2 + [2(a+2h)\sin\psi_{p_1}]^2}$$

$$\text{(iv) } \theta_{p_1} = \tan^{-1}\left[\frac{r_m + (a+2h)\cos\psi_{p_1}}{2(a+2h)\sin\psi_{p_1}}\right] \qquad (4.35)$$

where, $r_m \geq (a + 2h)[\ 1 + \text{cotan}\ \frac{\phi_t}{2}\ ]$. For the 10-element configuration and the first possible superarray geometry mentioned corresponding to Fig. 4.23a, $\phi_t= 36$ degrees, $\psi_{p_1}= 0$ degrees, $\psi_{p_2}= 45$ degrees, and $(a + 2h)= 0.21713\ \lambda_o$. With $r_m= 0.89$, the following translations were set: (i) $r_{t_2}= 0.74\ \lambda_o$, (ii) $\theta_{t_2}= 65.5$ degrees, (iii) $r_{t_1}= 1.09\ \lambda_o$, and (iv) $\theta_{t_1}= 73.6$ degrees.

Ten additional elements were placed in a ring fashion on the truncated cone of the original array of elements. Three of the original array elements, those centered about $\phi= 0$ degrees, were excited, and then one, two and three of the additional

elements were also excited. Table 10 lists some of the coverage area characteristics obtained, and Fig. 4.24 presents the gain contour plot for the situation when one of the additional elements is excited along with the original three. In lieu of tabulating the E-plane 8.0 dBic elevation beamwidth, which becomes distorted, the undistorted H-plane 8.0 dBic beamwidth is presented in Table 10.

Table 10: Results for the first superarray configuration

Addition of Elements		Coverage Area Characteristics				
Total Number	Location ϕ (deg.)	Pk.Gain (dBic)	PolarAng. (deg.)	Az.Angle (deg.)	H-Plane Az. BW.(deg.)	Ripple Value(dB)
1	0	12.78	30.0	6.00	56.00	1.28
2	-18,18	13.00	20.0	6.00	72.00	0.64
3	-36,0,36	13.56	15.0	9.00	90.00	0.34

An increase of 1.58 dBic is obtained with the additional excitation of one patch, and the beam shifts to θ=30.0 degrees, and ϕ= 6 degrees. Two beam peaks exist, in fact, as the second is generated at θ=50 degrees and ϕ= -3 degrees and has a peak value of 12.04 dBic. The field pattern in the H-plane is fairly broad as noted from the ripple value, but the E-plane field is distorted between the elevation angles of 40 and 55 degrees. Thus, the addition of a single element degrades the smooth broadside patterns associated with the single element and the previously presented array configurations, and it is anticipated that a complex phasing scheme will be necessary to scan the beams over the entire region of interest.

The results with the excitation of one and two additional patches did not rectify the distorted beam patterns. The H-plane patterns broadened considerably, and the E-plane patterns continued to show the distortion between the elevation angles of θ= 40

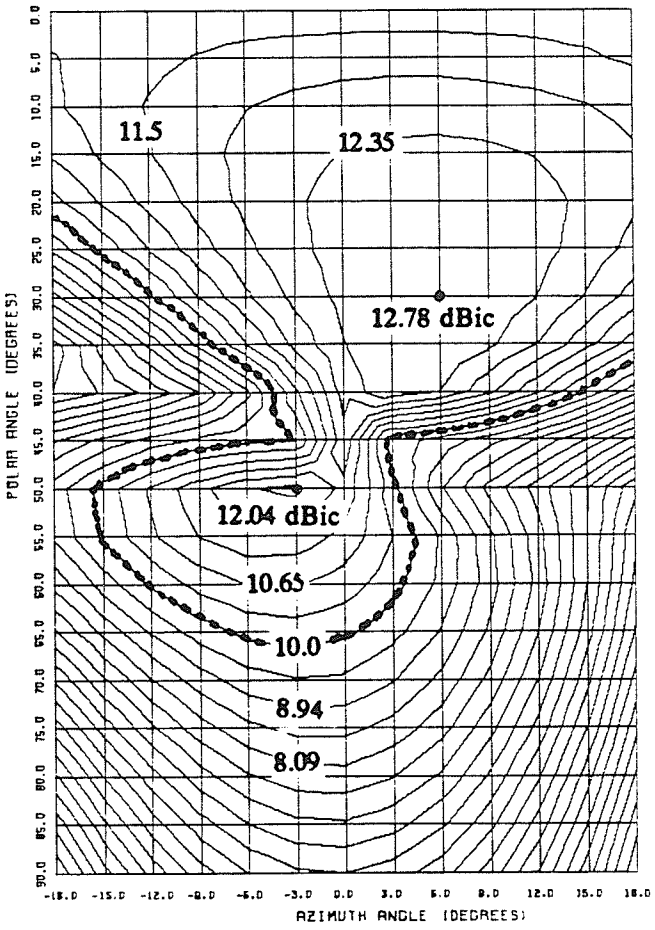

Figure 4.24: Gain contour pattern for the first superarray configuration with one added active element

and 55 degrees. The main beam peak shifted up, in fact, towards the zenith axis. As well, the peak gains of the resultant fields did not increase as greatly as did the additional excitation of one element. Peak gains of 13.0 and 13.56 dBic were generated. A larger gain will undoubtedly result when the elements are phased properly.

For the second possible super array configuration, the pitch angle for the additional elements was set to ψ_p= 22.5 degrees, half the value of the pitch angle of the original elements. This changes the translation vector to, (i) r_{t_2}= 0.792 λ_o and (ii) θ_{t_2}= 60.25 degrees. The translations for the original elements remain the same. Three of the original array elements are once again excited and the addition of one, two and three

of the added elements with every one fed with 0 and 90 degrees of phase excitation is simulated. Table 11 lists the results. The gain contour plot for one additional active element is similar to that of the previous geometry, but has different peak locations.

Table 11: Results for the second superarray configuration

Addition of Elements		Coverage Area Characteristics				
Total Number	Location ϕ (deg.)	Pk.Gain (dBic)	Polar Ang. (deg.)	Az.Angle (deg.)	H-Plane Az. BW.(deg.)	Ripple Value(dB)
1	0	13.12	35.0	3.00	36.00	5.12
2	-18,18	13.45	35.0	3.00	32.00	6.95
3	-36,0,36	13.92	30.0	3.00	36.00	5.92

With the additional tilted elements, it was hoped that the field patterns would broaden out and mimick the corresponding individual element patterns. For the second pitch or tilt of 22.5 degrees, such was not the case. Two beam peaks form again, one in the $\phi = 3$ and one in the $\phi = -3$ degree planes. The elevation angle location of the beam peaks is 35 degrees for the former and 50 degrees for the latter. Hence, degradation in the field patterns is once again present. In this case, the H-plane patterns are narrower but the E-plane patterns continue to show distortion for the elevation angles between $\theta = 40$ and 55 degrees. The gain increase for one additional elment is 1.9 dBic, and the relative increases with the addition of two and three patches is 2.2 and 2.7 dBic respectively. Optimization in the form of phasing the elements to radiate over the required regions will definitely be necessary. If the gain increases mentioned are not cancelled by additional losses in the feed network design, such superarray configurations may be feasible. Otherwise, the superarray geometries presented here must be modified in some way until the field patterns and gain values are acceptable.

4.8 Proposed Feeding Arrangement and Beam Positioning Control

This section describes the antenna feed network and beam positioning control from a system approach that would be required for the 10-element array arrangement. In the descriptions, the restrictions and components which should be incorporated into the design are mentioned, although these may be changed or substituted in the final design.

First of all, several considerations must be kept in mind in designing the feed network. The feed line structure must be such that each element is fed equal signal power when transmitting. This implicitly requires that no imbalances in feed line impedance be present to distort the power distribution. The feed line lengths to each element should also be of equal length such that no unwanted differential phase shifts are obtained. Finally, the feed network must be as simple as possible in order to minimize the network losses.

For the particular numerically optimized 10-element array, several other considerations must also be taken into account. Since each patch is fed with two probes, 2 feed lines per element are required. In addition, each feed must have 0, 45, 90, and 135 degrees of phase excitation available to it so that both right and left hand circular polarizations may be generated. Finally, the feed network must incorporate a satellite detection scheme in order to position the beam peak in the required direction.

A block diagram of the proposed feed network and satellite detection scheme is shown in Fig. 4.25. The actual antenna feed network begins with a duplexor. This component is comprised of two bandpass filters covering the uplink and downlink frequency bands as well as the pilot signal frequency. The duplexor allows for the simultaneous transmission and reception of a signal. The ouptut of the duplexor is then fed into a two-way power divider whose outputs are fed into the first of two polarization switches. This polarization switch yields a zero or 90 degree phase excitation to each line. Thus, only a single control line needs to be generated for this switch.

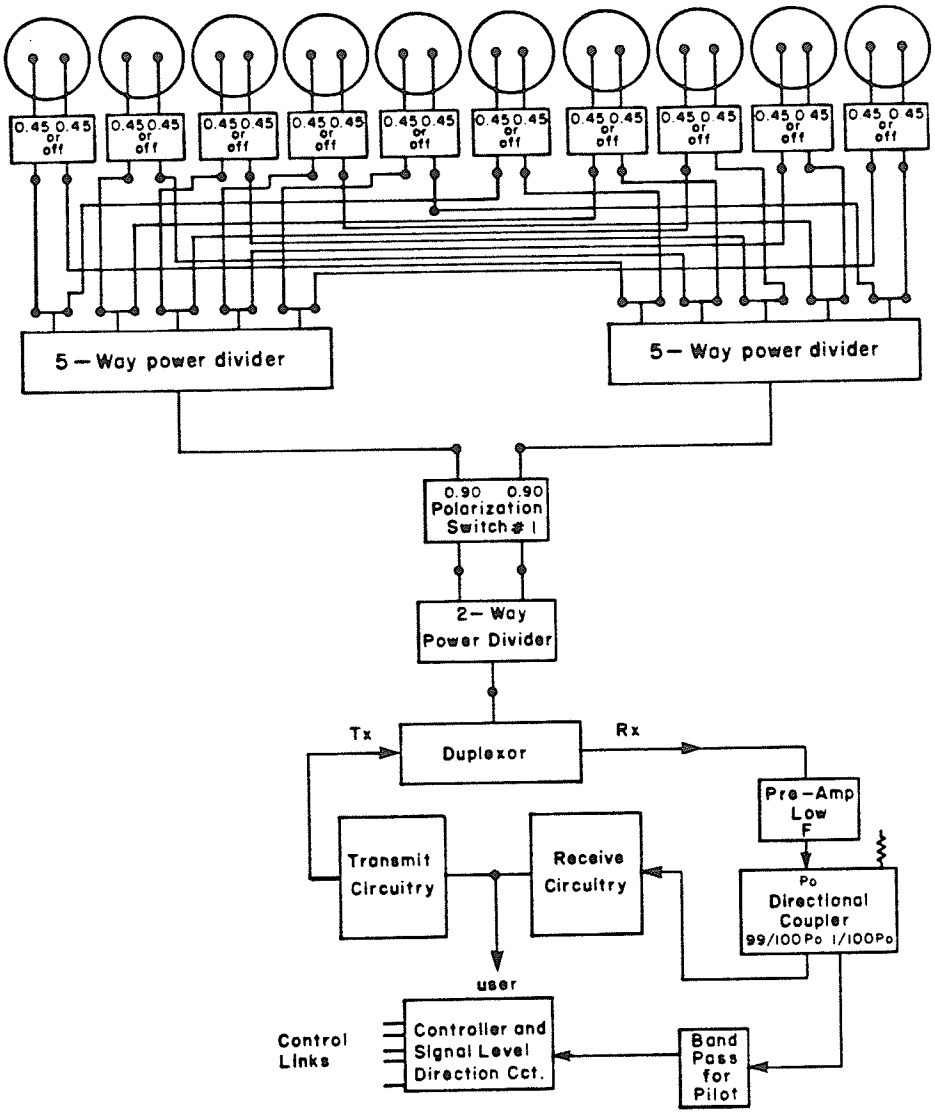

Figure 4.25: A feed network and beam positioning control system

The two outputs of the polarization switch are then fed into two five-way power dividers. Each output of the dividers is then split into two again so that 10 feed lines are available from each power divider. Each of these 10 lines is then fed into a second polarization switch which is present at the input to each of the 10 elements. This second switch should have three states. When it is on, zero and 45 degrees of relative phase excitation should be available, and when it is off, it should dissipate any energy

incident upon it. By constructing it in this way, the switching control of the element to be excited is accomplished, and further, by the appropriate switching of the two polarization switches, all the required phase excitations are generated for each of the feeds.

The remaining task in the feed line design is to construct them and the second polarization switch in a balanced and even manner as described earlier in this section. With the circular symmetry present, a multi-layer structure would be very beneficial and convenient. Such a space conserving scheme has been suggested by Abouzahra [21] for a particular planar array. Moreover, the 5-way dividers used in the system design may be based on the type constructed by Yau et al [22]. They based their design on a tapered transmission line scheme and obtained a mismatch loss of 0.09 dB and an insertion loss of 0.2 dB over a broad frequency range from 2 to 18 GHz.

On the other side of the duplexor, the receive and transmit circuitry are broken into two separate but interconnected blocks. Only the receive block is expanded here to show that it includes a pre amp with a very low noise figure, a directional coupler, and the appropriate blocks that process the pilot signal to determine the direction of the maximum signal and to determine the appropriate elements to be excited with the proper phases. The proposed beam switching scheme is to excite a fourth element on either side of the primary active three elements whenever the received signal falls below a set threshold. In this way, a comparison can be made between the two directions, and the appropriate switching can be performed to direct the beam in the direction of the higher signal level.

The scheme described is a first order system design and much improvement is possible. It does, however, perform the required tasks with a fairly straightforward control.

4.9 Single Element Input Impedance: Theoretical and Experimental

The input or driving point impedance of an antenna is that seen by the source and is defined as,

$$Z_{in} = \frac{\text{Complex Terminal Voltage}}{\text{Complex Terminal Current}} = R_{in} + jX_{in}$$

For the circular patch microstrip antenna, the cavity model is used to evaluate this driving point impedance. As shown by Bahl and Bhartia [14], the cavity can be modelled by passive network elements, which, when referenced to the probe location, give an approximate value for the input impedance of the antenna. This basic model, with the addition of two other components to model the probe reactances and feed connector length, will be presented in this section. A profile of the typical element used in the experimental work is shown in Fig. 4.26. Note that only one of the two probes is visible in this view.

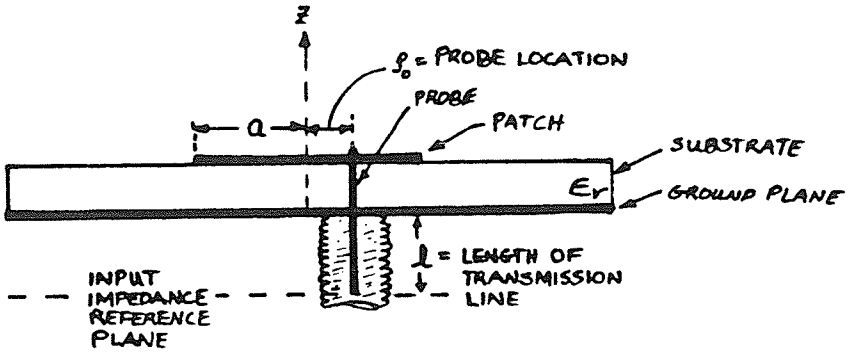

Figure 4.26: A profile of the circular microstrip patch antenna

To begin, the ideal cavity formed by the two electric and two magnetic walls, is replaced by a parallel resonant L-C circuit referenced to the probe location. Then,

some additional compensating components must be added to account for the actual leaky cavity walls which have an admittance. Based on the expressions for the aperture admittance given in section 4.2, the compensating components are modelled as a resistor R_a in parallel with a capacitor C_a. Since this R-C impedance is located at the aperture wall, it must be referenced back to the probe. The transition between the probe and the aperture is of the form of a radial waveguide. Thus, this section is modelled as an ideal transformer with a step down coefficient n, which causes the wall impedances to be stepped down in value by n^2.

Furthermore, the small section of probe located within the cavity presents some reactance. Based on an expression for the reactance of a probe in a homogeneous parallel plate waveguide [23], this reactance is modelled by an inductor. Since two such probes exist in the cavity, the mutual impedance presented by the second probe is taken into account by doubling the value of the inductor. Finally, in the experimental recording of the input impedance of the patch element, the reference plane was set at the output of the probe connector. Thus, all recorded impedances are referenced at this point. To account for this in the simulation, the short length of probe from the connector input to the base of the substrate is modelled as a short length of transmission line. The length was measured to be 7.0 mm for a characteristic impedance of $Z_o = 50\ \Omega$. The equivalent circuit with all the elements is shown in Fig. 4.27. Figure 4.28 shows all the elements when referenced to the probe location.

Before the values for each of the elements are given, the general symbolic expression for the equivalent input impedance will be derived. This derivation will be in three steps. Firstly, the equivalent admittance seen at the terminals denoted by 3-3 is simply the sum of the four elemental admittances, namely,

$$Y_{eq} = \frac{1}{X_L} + \frac{1}{X_C} + \frac{1}{n^2 X_{Ca}} + \frac{1}{n^2 R_a}$$

$$\text{or,}\quad Y_{eq}(\omega) = \frac{n^2 R_a - \omega^2 L R_a (n^2 C + C_a) + j\omega L}{j\omega L n^2 R_a} \qquad (4.36)$$

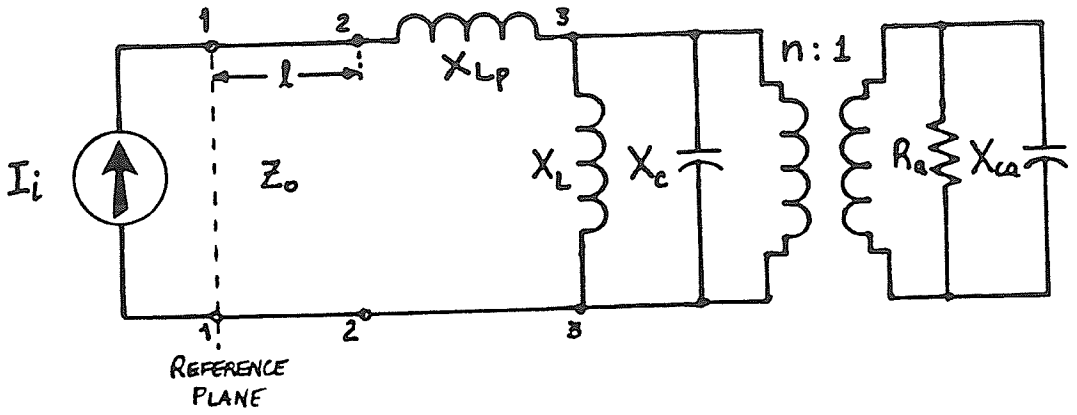

Figure 4.27: Equivalent circuit representation for the circular patch antenna

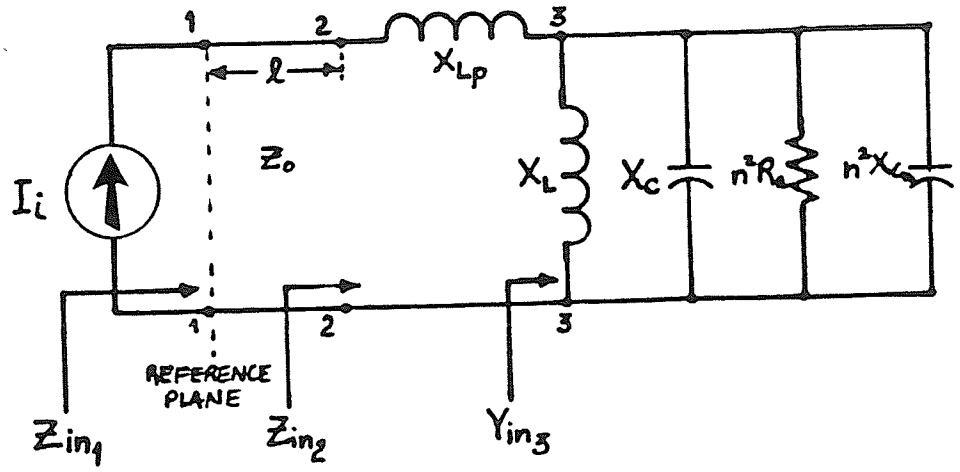

Figure 4.28: Equivalent circuit parameters referenced to the probe location

The impedance at the terminals denoted by 2-2 is then obtained as,

$$Z_{in_2} = R_{in_2} + j\omega X_{in_2}$$

$$\text{where, } R_{in_2} = \frac{\omega^2 L^2 n^2 R_a}{R_a^2(n^2 - \omega^2 L C_{eq})^2 + \omega^2 L^2} \tag{4.37}$$

$$\text{and, } X_{in_2} = L_p + \frac{L n^2 R_a^2 (n^2 - \omega^2 L C_{eq})}{R_a^2 (n^2 - \omega^2 L C_{eq})^2 + \omega^2 L^2} \tag{4.38}$$

In the above expressions, $C_{eq} = n^2C + C_a$. Finally, the total impedance at terminals 1-1, the output of the SMA female connector, can be obtained by using the expression for referencing impedances along transmission lines [24] namely,

$$Z_{in_1} = Z_o \left\{ \frac{Z_{in_2} + jZ_o\tan\beta l}{Z_o + Z_{in_2}\tan\beta l} \right\} \tag{4.39}$$

where, β= the wave number along the transmission line,

Z_o= the characteristic impedance = 50.0 Ω ,

and l = the length of the transmission line = 7.0 mm.

The result is, $Z_{in_1} = R_{in_1} + j\omega X_{in_1}$,

$$\text{where,} \quad R_{in_1} = \left[\frac{R_{in_2}Z_o^2(1 + \tan^2\beta l)}{Z_o^2 - 2Z_oX_{in_2}\tan\beta l + (X_{in_2}^2 + R_{in_2}^2)\tan^2\beta l} \right] \tag{4.40}$$

$$\text{and,} \quad X_{in_1} = Z_o \left[\frac{Z_oX_{in_2} - (X_{in_2}^2 + R_{in_2}^2 - Z_o^2)\tan\beta l - X_{in_2}Z_o\tan^2\beta l}{Z_o^2 - 2Z_oX_{in_2}\tan\beta l + (X_{in_2}^2 + R_{in_2}^2)\tan^2\beta l} \right] \tag{4.41}$$

The values for the equivalent network elements will now be presented. Starting with the aperture impedance, the expression for the wall conductance, g_a, was computed as the ratio of the fields at the aperture. To consider it as a circuit element, we use the fact that the radiated power from the antenna in terms of the conductance, is [16],

$$P_r = \frac{1}{2}\pi ha(E_z \mid_{\rho = a})^2 g_a = G_a V_o^2 \quad \text{(W)} \tag{4.42}$$

where $V_o = E_z h$ is the voltage across the cavity gap. Hence,

$$R_a = \frac{1}{G_a} = \frac{2h}{\pi a g_a} \quad (\Omega) \tag{4.43}$$

Note that the exact expression for the aperture capacitance is not required at this point since it will be incorporated into the cavity capacitance to produce the equivalent

capacitance C_{eq}. The transformer step coefficient, n, can be derived from the Green's function representation of the fields within the cavity, and is simply given as the ratio of the ρ-variable eigenfunctions at the probe location to the physical patch location as [25]

$$n^2 = \frac{J_n^2(k_{nm}\rho_o)}{J_n^2(k_{nm}a)} \tag{4.44}$$

As mentioned earlier, the expression for the probe reactance is that for a probe in a homogeneous parallel plate waveguide and is given as,

$$L_p' = \frac{\mu_o h}{2\pi}\ln\left(\frac{4c}{\omega\gamma\sqrt{\varepsilon_r}d}\right) \quad (\Omega) \tag{4.45}$$

where, $\gamma = 1.781$ and d is the probe diameter. Since the mutal inductance of the other probe is also included, $L_p = 2.0 \times L_p'$. Finally, to determine the values for the inductance L and capacitance C_{eq} of the parallel resonant circuit, the quality factor of the cavity as well as the theoretical resonant frequency must be known. The theoretical resonant frequency is easily obtained from the eigenvalue equation of the boundary value problem solved earlier,

$$\omega_o = \frac{1.84118c}{a_{eff}\sqrt{\varepsilon_r}} \quad \left(\frac{rad}{sec}\right) \tag{4.46}$$

The quality factor is defined as,

$$Q = \omega \frac{W_T}{P_T} \tag{4.47}$$

where, W_T= energy stored within the cavity, and

$P_T = P_r + P_d + P_c$

P_r= the total power radiated,

P_d= the dielectric losses, and

P_c= the conductor losses.

The expressions for W_T and P_T for dominant mode excitation are given by Bahl and

Bhartia [14]. Once values for Q and ω_o are generated, the values for L and C_{eq} are,

$$C_{eq} = \frac{Q}{\omega_o R_a} \quad \text{and} \quad L = \frac{R_a}{\omega_o Q} \tag{4.48}$$

Thus, all component values are known and the input impedance as a function of frequency can be generated.

For the numerical and experimental results, the following patch characteristics were employed:

ε_r= 2.52,

h= 1.59 mm,

d= 1.25 mm,

a= 1.65 cm,

δ= loss tangent of the dielectric = 0.002

$\sigma_{cu}= 5.7\times10^7 \quad (\frac{1}{\Omega\,m})$

and $\frac{\rho_o}{a}$= 0.5,

where ρ_o is the probe position. Note that this particular probe location is not ideal for 50 Ω operation. An input impedance of 50 Ω occurs when $\frac{\rho_o}{a}$= 0.2. The formerly mentioned value had to be used, however, to allow enough working space in behind the element so that feed cables could be easily connected and disconnected to and from the probes.

The results for the theoretical input impedance are shown in Fig. 4.29 in a rectangular plot. There are two resonant points, one at 2.99 GHz and one at 3.25 GHz. The former corresponds to the sought after theoretical resonant frequency of 3.0 GHz. The latter corresponds to a point at which the reactance of the probes cancels the reactance of the patch impedance. Hence, the latter resonance is artificially created by the inclusion of the two probes. Note that resonance is defined here as that point at which the reactance is zero.

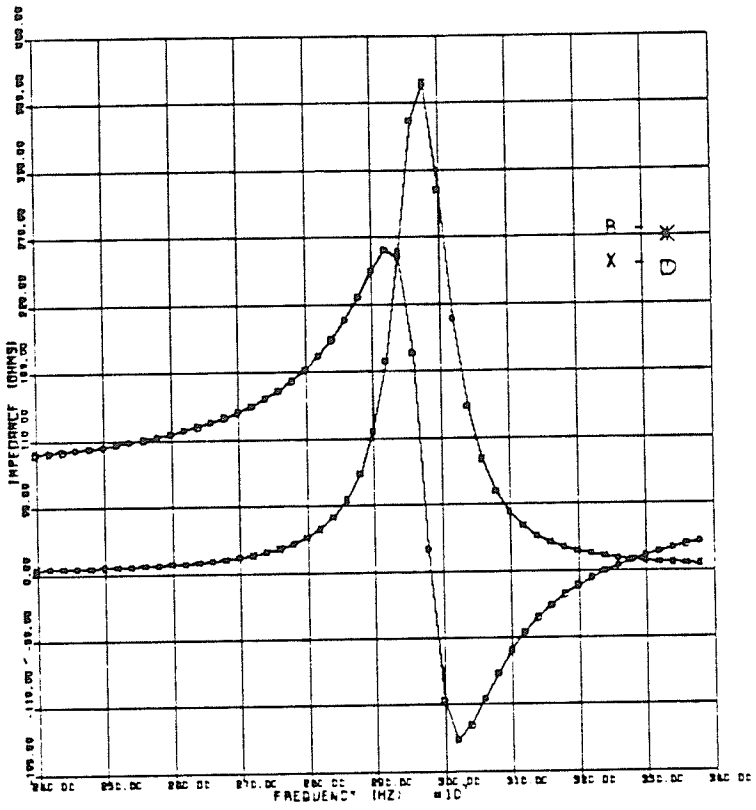

Figure 4.29: Theoretical input impedance vs frequency for the patch antenna

The experimental input impedance was measured for the elements for two distinct patch-plus-substrate dimensions. The two dimensions are shown below in Fig. 4.30. The first geometry was that used in the initial array configuration while the second smaller dimensions were used for later tests for which the patch-plus-substrate had to be cut. Figures 4.31 and 4.32 present the normalized input impedances in Smith Chart representation for the two patch-plus-substrate dimensions.

The experimental input impedance given by Figs. 4.31 and 4.32 is representative of each element in the array for each probe. It is immediately apparent that the input impedance of the smaller patch-plus-substrate is larger in and around the first resonant frequency. For example, at 3.03 GHz, the resistance for the smaller configuration is 400 Ω, while that for the larger dimensions is 300 Ω. The results in and around the

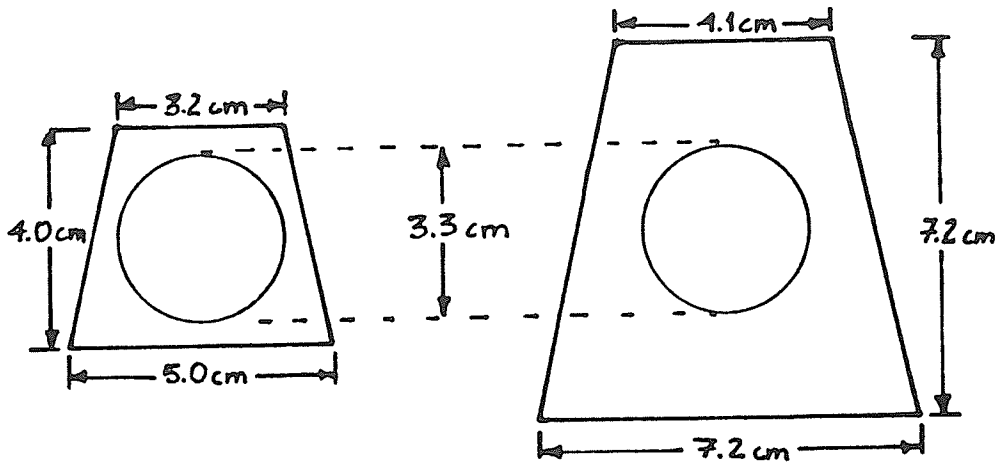

Figure 4.30: Two patch-plus-substrate dimensions used in the experimental work

artificially created resonant frequency are nearly identical for the two. The theoretical impedance, when normalized to the 50 Ω system, and shown as the dotted curve in both figures, is very accurate in its prediction. The model holds true more so for the smaller patch plus substrate dimensions than that for the larger dimensions. Moreover, the predicted resonant frequencies are nearly identical to the experimentally observed ones.

In discussing the mismatch loss at the antenna terminals, it was necessary to obtain the return loss of the antenna elements. Since the probe position could not be placed at that point for 50 Ω at resonance, the mismatch loss at the antenna terminals was expected to be large. However, if the same mismatch loss could be obtained for each of the elements in the array, the size of the value would be indeterminant. Such was the case for the 3 elements used in the experimental work. Figure 4.33 shows the return loss per probe for each of the three patches.

As seen from Fig. 4.33, the largest return loss occurs at the artificially created resonant frequency of 3.22 GHz. Consequently, since this is the frequency at which the antenna is best matched, all upcoming experimental patterns in Chapter 5 will treat this as the center frequency of operation for the antenna. The expression for the mismatch

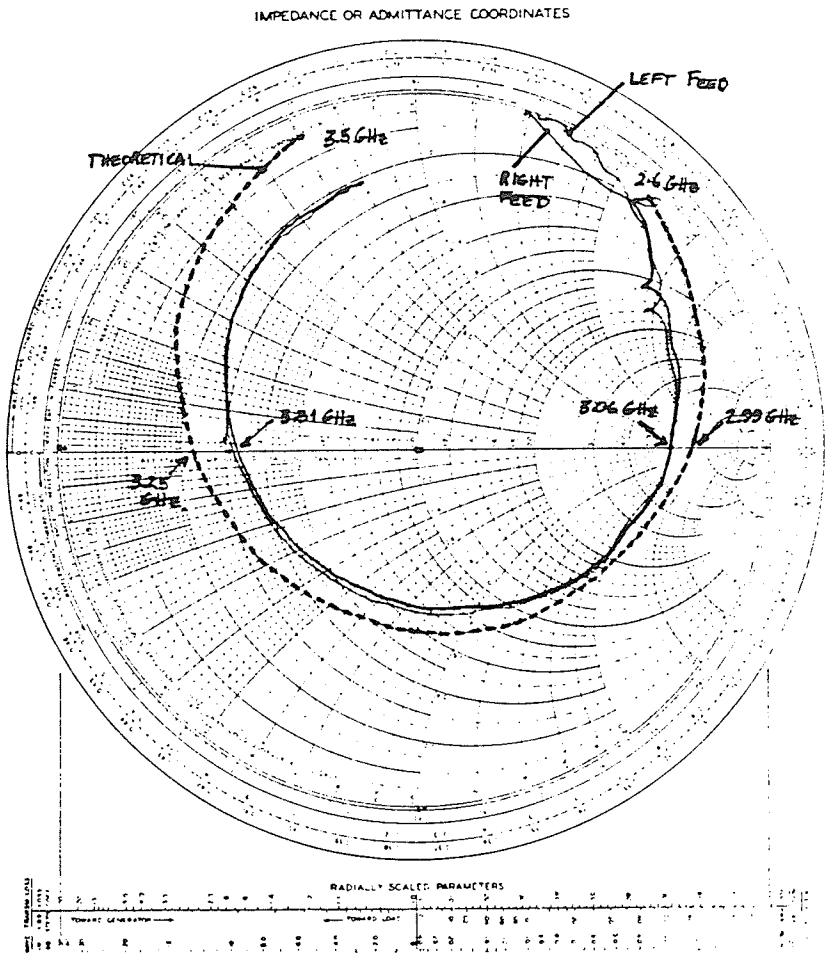

Figure 4.31: Input Impedance for the larger patch-plus-substrate geometry

loss in terms of the reflection cooefficient of the antenna, Γ_L, is

$$L_M = 10 \text{ LOG } \left(\frac{1}{1 - |\Gamma_L|^2} \right) \tag{4.49}$$

and the reflection cooefficient magnitude in terms of the return loss value (L_R) is,

$$|\Gamma_L|^2 = 10^{-(\frac{|L_R|}{10})} \tag{4.50}$$

From the experimental results, the return loss values for the three elements varied between 5.0 and 6.0 dB. On average then, the return loss is approximately 5.5 dB per

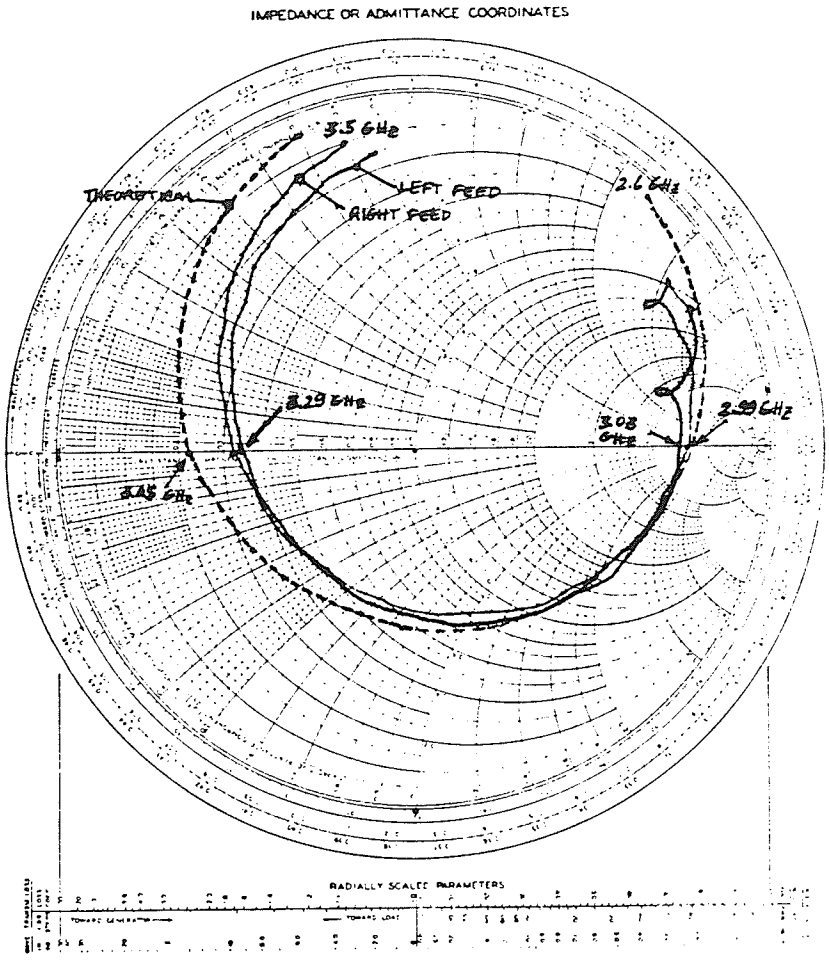

Figure 4.32: Input Impedance for the smaller patch-plus-substrate geometry

element which corresponds to a mismatch loss of 1.44 dB. This value will be taken into account later when the experimental absolute gain of the antenna is calculated.

Finally, the frequency bandwidth of the antenna may be obtained from the return loss measurements. It is apparent from the curves that the antenna's return loss value of 5.5 dB is approximately constant over a 75 MHz bandwidth, from 3.175 GHz to 3.25 GHz. This corresponds to a 2.3 % bandwidth. This low value was expected, since the major drawback of the microstrip antenna is its narrow frequency bandwidth. However, methods do exist which can increase the bandwidth. One in particular is to

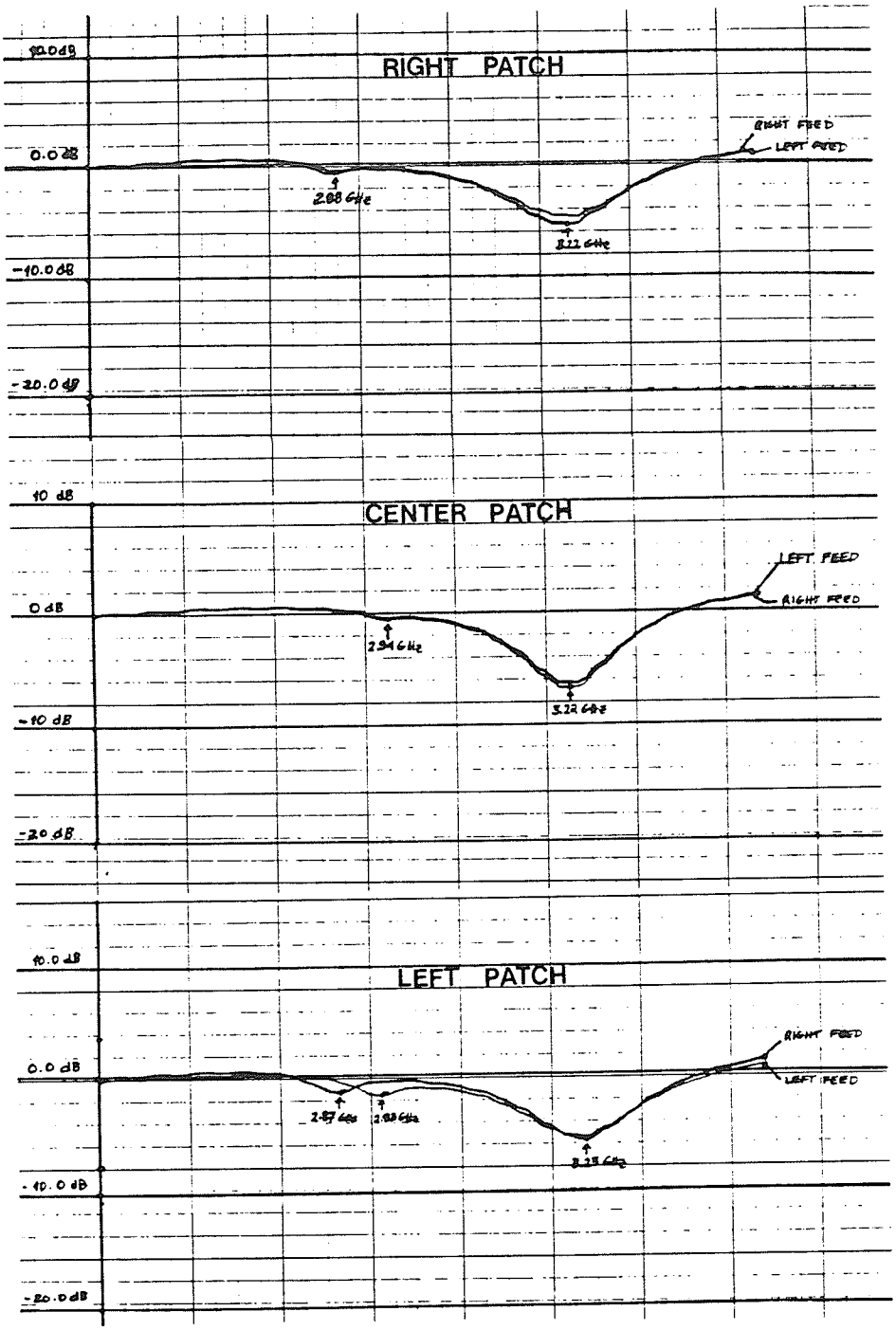

Figure 4.33: Return Loss curves for the three array elements

place a parasitic element above the active one. Hori et al [26] built a 6-element spherical array in such a fashion and found the resultant bandwidth to be 8.0 %.

CHAPTER 5

EXPERIMENTAL PERFORMANCE OF A TEN-ELEMENT CONICAL PATCH ANTENNA

5.1 Introduction

Based on the results of Chapter 4, a prototype antenna array was constructed and its radiation characteristics were explored using the antenna measurement system in the University of Manitoba's anechoic chamber. Various array arrangements were studied during the experimental work in order to determine their effect on the radiation patterns.

In the following section, observations from experiments performed with a single element above a ground plane are presented. The work was done prior to the array testing so as to acquire some knowledge of the ground plane effects on the individual element's far field distribution and ellipticity. The remainder of the chapter focuses on a 10-element, 3-patch excitation array. Its construction and feed system are discussed and the observed radiation characteristics are presented for three different element dimensions.

5.2 Observations from a Single Element Above a Ground Plane

The first step in the experimental work was to examine the radiation patterns of a single circular microstrip patch antenna above a large ground plane. The patch was printed on an oak substrate with a copper backplane. Figure 5.1 shows two views of the element used in the tests along with dimensional information.

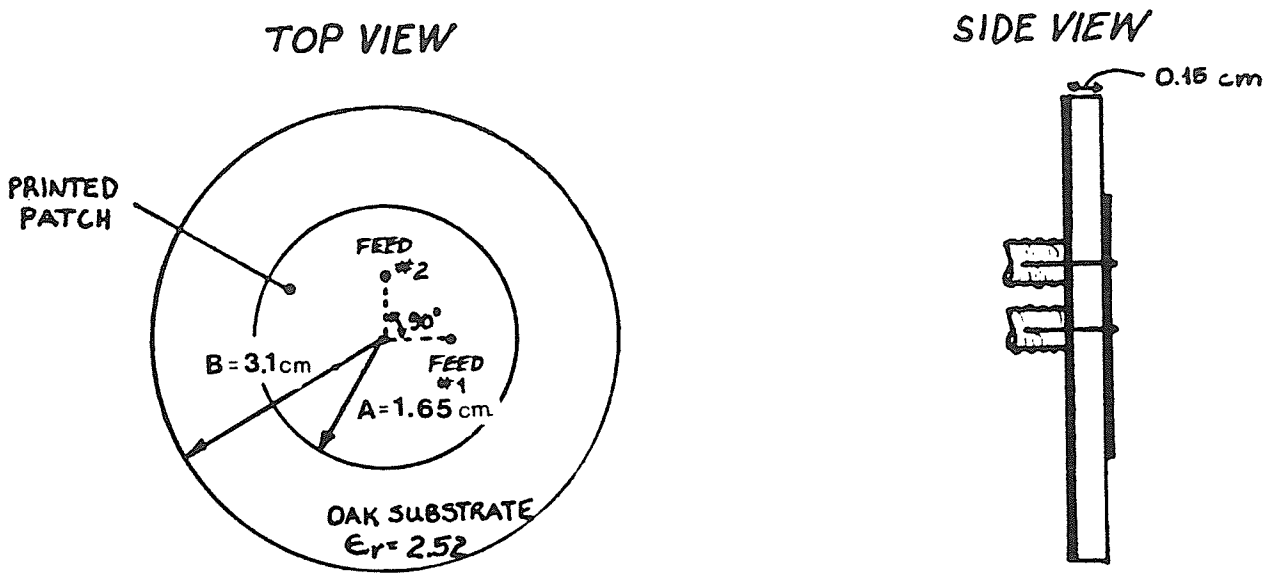

Figure 5.1: The single element used for the first tests

A non-metallic supporting brace was secured in the center of a large ground plane. The patch was then mounted on this brace with the feed cables protruding from behind the element. The size of the ground plane used was approximately 40 × 60 cm, so that the distance from the element-edge to the ground plane edge was about 25 cm or 2.7 λ at 3.2 GHz. The element feed system included a 90 degree hybrid necessary to produce the phase difference required to generate a circularly polarized far field. Although many experimental results were obtained for various tilt angles and patch-edge to ground plane distances, only the ground plane effect on the feed orientation and beam peak position is presented. These particular cases are mentioned since they are the ones incorporated into the array construction.

Two different feed orientations were examined in the testing. These are shown in Figs. 5.2a and 5.2b. Since the local field distribution for a single feed patch in the dominant mode is of the form, $E_z = E_a \cos(\beta - \beta_f)$, it is apparent that for feed #1, the local fields are minimum at $\phi = 90$ and 270 degrees. Similarly, for feed #2, the fields are minimum at $\phi = 0$ and 180 degrees. Consequently, the equivalent magnetic currents

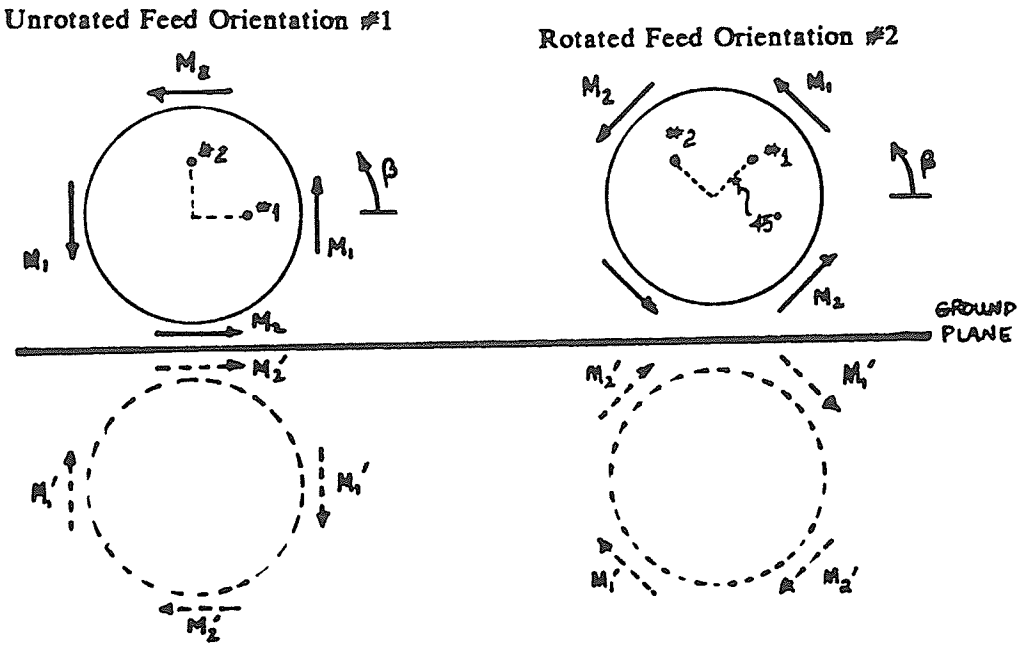

Figure 5.2: Feed orientations above the ground plane

are minimum at the same respective locations. The arrows with symbols M_1 and M_2 shown in Fig. 5.2 represent these magnetic currents. Note that the same analysis holds true for the equivalent electric currents. With the equivalent currents as defined above, the images for the vertical current components of feed #1 are in the opposite direction whereas the images for the horizontal current components of feed #2 are in the same directions. Hence, problems in the ellipticity of the far fields are anticipated since the effect of the image currents of the two feeds will not be equal over the elevation region. In an attempt to rectify this problem, the feeds were rotated by 45 degrees to the orientation shown in Fig. 5.2b. Here, the fields produced by each feed are equally affected by the ground plane, so the ellipticity of the far field is expected to be better.

From the experimental observations, the ellipticity of the fields produced by the rotated feed configuration was in every case as good or better than the corresponding fields from the unrotated feed configuration. Patch-edge to ground plane distances were set from d= 1.5 cm to d=8.0 cm for the two feed orientations, where d is the distance from the patch-edge to ground plane. For the larger distances, the effects of the

ground plane and feed orientation were not as noticeable as for the smaller distances. For d=8.0 cm, for example, a beam peak near θ= 45 degrees was observed and the ripple in the rotating linear pattern had peak to peak oscillations of 2 dB up to θ= 50 degrees, after which the oscillations grew in size up to 6 dB. For d=1.5 cm, on the other hand, the beam peak relocated to θ= 52 degrees and oscillations were now 3-4 dB up to θ= 45 degrees after which they grew in value to around 5 to 6 dB. This beam peak shift of 12 degrees is the second key result that was observed and taken into consideration for the tests performed with the array, as a 45 degree tilt was used in all the experimental work. Figure 5.3 shows the E-plane pattern for d=1.5 cm with the rotated feeds.

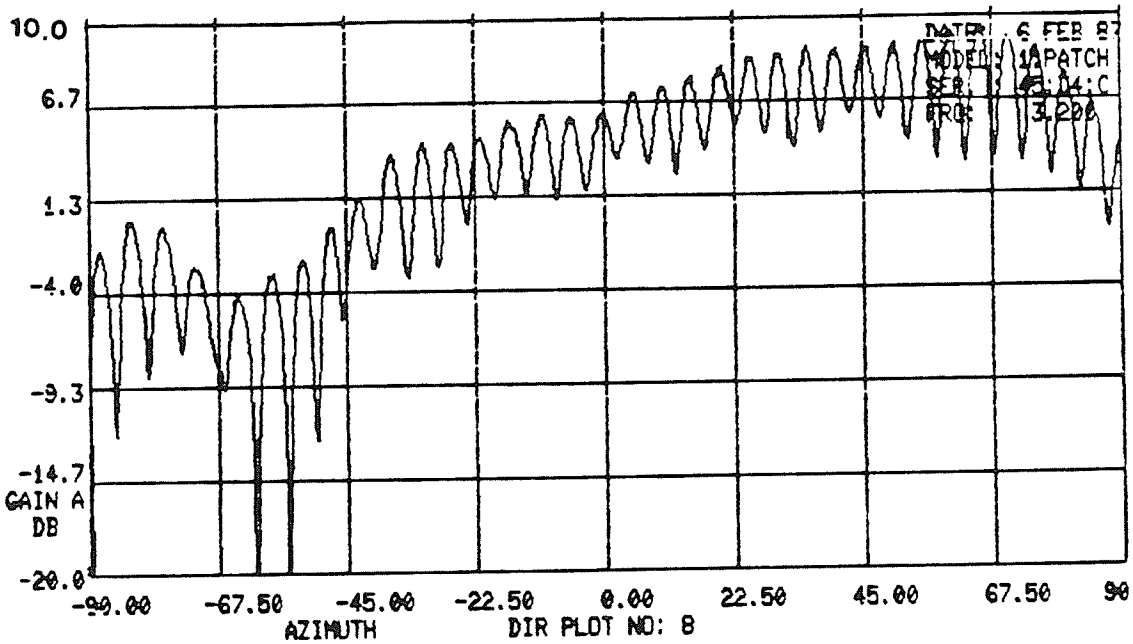

Figure 5.3: E-plane pattern for d= 1.5 cm with rotated feeds

To obtain some insight into the causes for the poor ellipticity over some of the elevation regions and for the beam peak shift, two linearly polarized tests were performed for the element with the unrotated feed configuration. The first test had the transmitting horn set to radiate a vertically polarized wave while in the second test, a

horizontally polarized wave was transmitted. Both the amplitude and the phase of the resultant fields were recorded. Figure 5.4 shows the resultant field amplitudes and Fig. 5.5 the resultant phases.

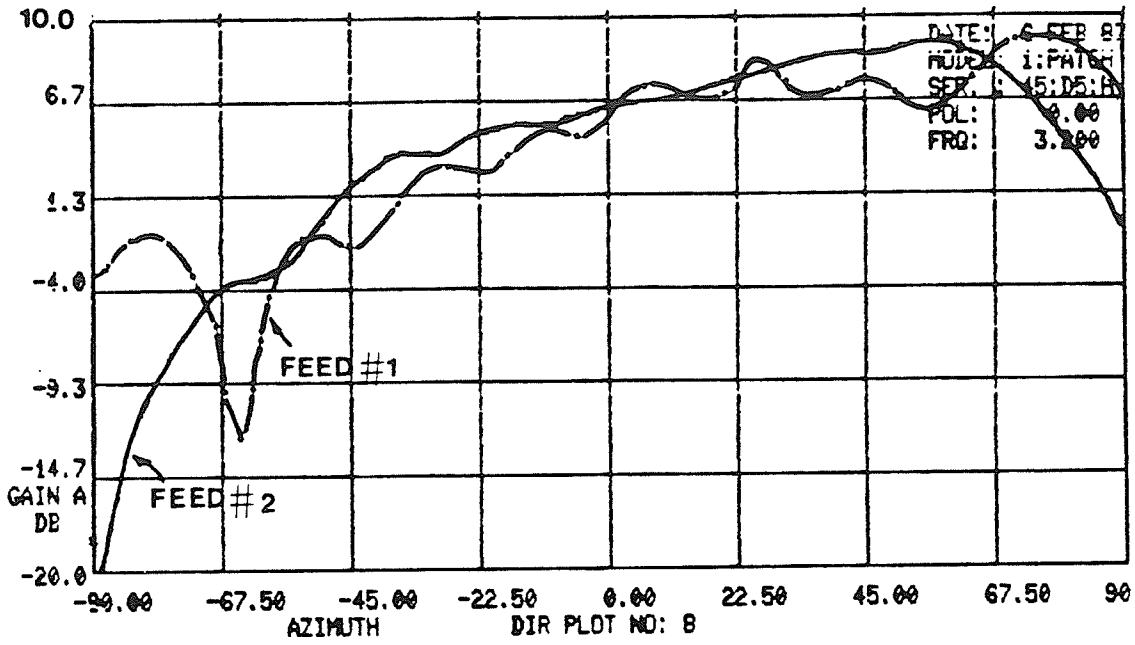

Figure 5.4: Amplitude pattern for the vertically and horizontally illuminated single patch element with 45 degree tilt

The transmitted vertically polarized wave corresponds to the E-plane pattern due to feed #1 while the transmitted horizontally polarized wave corresponds to the E-plane pattern due to feed #2. As can be seen from a comparison of the amplitudes, the fields due to feed #1 oscillate throughout the entire elevation region and the beam peak occurs at θ= 70 degrees. On the other hand, the fields due to feed #2 are smooth with a beam peak at θ= 50 degrees. These results support the argument given earlier for the effects of the ground plane on the equivalent currents due to the two feeds. Similarly, the phase distribution for the E-plane of feed #1 is not as uniform as that obtained for feed #2. Consistency in the phase for the two feed locations is present only between θ= -45 to 40 degrees, but even in this region, there is a discrepancy of

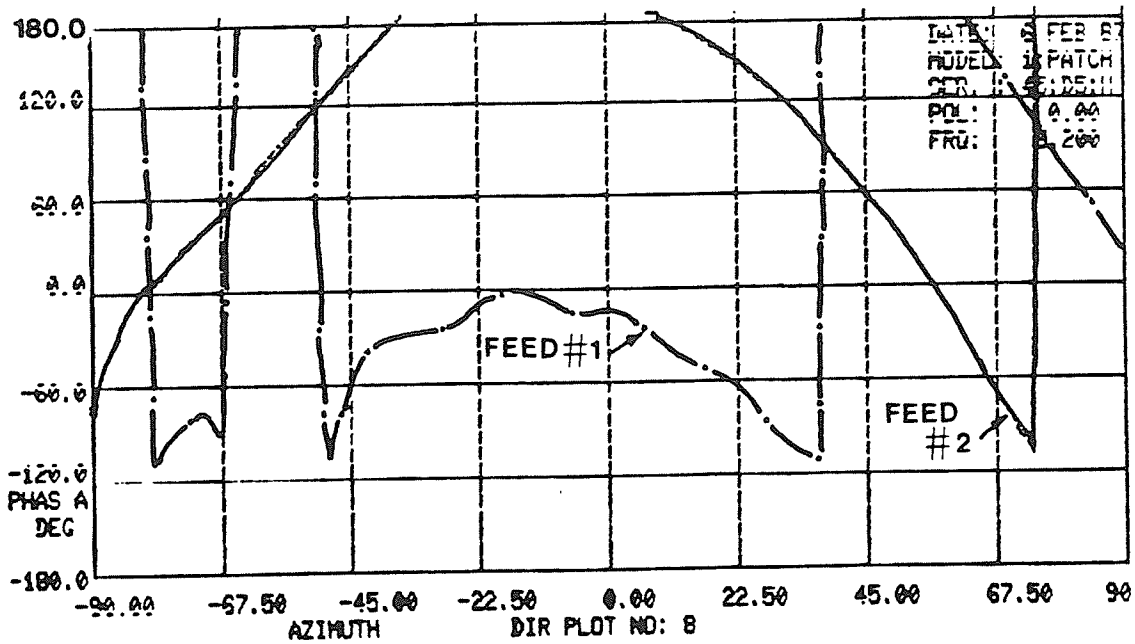

Figure 5.5: Phase pattern for the vertically and horizontally illuminated single patch element with 45 degree tilt

180 degrees between the two values. Due to these observed differences in amplitude and phase, the resulting ellipticity is therefore poor. The beam peak shift is more difficult to understand, but is apparently a result of the combination of the patch-edge to ground plane distance and the ground plane size. This effect will be further explored with the array experiments.

The beam peak elevation for a single element can thus be positioned in three ways. The first method is by setting a particular patch-edge to ground plane distance. The second is by the use of a finite ground plane. The last method is by varying the tilt angle of the conical support. In addition to positioning the peak elevation, however, each method causes a degradation in the ellipticity of the far fields, particularly for the last case mentioned. These observations can now be incorporated into the array construction and testing.

5.3 Construction of the Array and The Feed System

To reduce experimental complexity and since only 3 of the 10 array elements are radiating at one particular time, only 5 of the array elements were constructed and tested. Also, only the middle three were fitted with feed probes, as the outer element on either side of the three active ones act as parasitic elements and are included to account for any coupling or scattering that may be introduced. Figure 5.6 shows a photo of the constructed array.

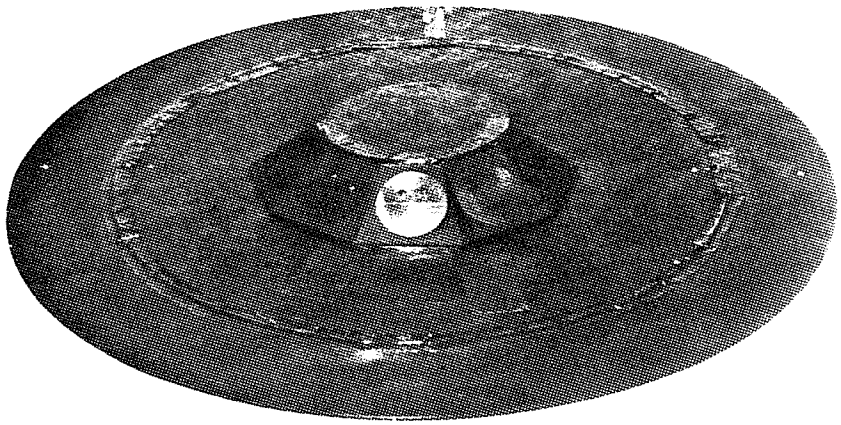

Figure 5.6: Photo of the constructed array

Two ground plane sizes were incorporated into the construction: the normal ground plane had a radius of 15 cm and with an extended 5 cm ring, the extended ground plane had a radius of 20 cm. The added ring extension was shorted to the fixed ground plane using copper tape. Copper tape was also used to short the back planes of individual elements to the ground plane. As well, for some of the tests, a metallic cap, as

shown in the photo, was placed on the top of the conical support and shorted with copper tape to the element back planes. For other tests, the cap was replaced by absorbing material.

The antenna dimensions were initially referenced to the S-band center frequency of 3.0 GHz where λ= 10 cm. All experiments were performed using frequencies between 2.0 and 4.0 GHz since this was the operating bandwidth of the test equipment being used. The actual dimensions of the array at 1.6 GHz would be approximately 2 times greater. Hence, the outer ground plane radius of 20 cm or 2 λ at 3.0 GHz, would be about 40 cm at 1.6 GHz. The resulting ground plane diameter is then 80 cm which is a good approximation to a car top which has an area, on average, of 1 m^2.

As mentioned earlier, the tilt angle for the array was set to 45 degrees for each test and supporting brackets were no longer employed as they were too awkward to use. Thus, the 45 degree tilt was obtained by cutting the sides of the element to appropriate angles, such that when the elements were brought together, the array had the required tilt. To consider other tilts, it would have been necessary to cut the sides of the elements at some other angle. Furthermore, the feed probes connected to the elements were rotated the 45 degrees required to minimize the ground plane effect on the ellipticity of the fields. Three different array configurations were used in the experiments, these being obtained by varying the size of the element's backplane. Consequently, the height of the element's patch-center above the ground plane was varied. Each time the tests for one particular element configuration were completed, the element backplanes were cut. In this way, no repeat experiments could be performed on the earlier used array configurations.

The feed network used for the experimental work is shown in Fig. 5.7. The feed network consisted of a Mini-Circuits ZA3PD 3-way power divider, three ARRA Inc. 4164-90 90 degree hybrids, three 50 Ω matched loads and nine coaxial cables of the same lengths. The cables were assumed to have losses on the order of 0.1 dB, the insertion loss of the power splitter was specified as a maximum of 1.0 dB, and the

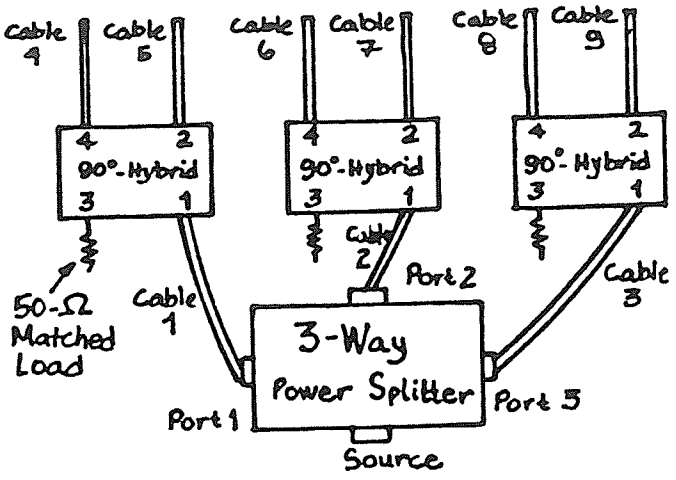

Figure 5.7: Feed network used in the experimental array work

hybrids were specified to have an insertion loss of 0.25 dB with a VSWR of 1.25, which translates to a 0.11 dB mismatch loss. Adding up all the losses results in a total feed network loss per feed probe of 1.56 dB. Adding in the feed probe mismatch loss of 1.44 dB at 3.2 GHz, the total losses add up to 3.0 dB.

The losses were checked by performing various measurements on the components at 3.2 GHz. Table 12 lists the insertion losses and phase shifts (referenced to a short circiuit) of the nine cables to verify that they were indeed similar. The total loss for each probe from the power source input to the output of the cable which connects to the feed probe, was then recorded. Two of the three ports were match terminated and ideal 2 and 3-way power splits were assumed through the hybrids and the power divider respectively. The measurement was then made at one cable from the hybrid output while the other port and cable were connected to the antenna feed connector. The setup is shown in Fig. 5.8. The 2- and 3-way power splits account for 7.77 dB of the power loss through the network, so that the total insertion loss is obtained by subtracting this value from the recorded measurement. Table 13 lists the insertion losses

Table 12: Cable measurement results

Cable #	Phase Shift (deg.)	Insertion Loss (dB)
1	115	0.218
2	117	0.218
3	117	0.218
4	117	0.250
5	117	0.250
6	117	0.250
7	117	0.250
8	113	0.250
9	113	0.250

measured for each of the feeds.

Table 13: Insertion loss measurements

Feed Branch	Measured Loss (dB)	Insertion Loss (dB)
Port 1-cable 4	9.75	1.98
Port 1-cable 5	9.75	1.98
Port 2-cable 6	9.38	1.61
Port 2-cable 7	9.38	1.61
Port 3-cable 8	9.63	1.86
Port 3-cable 9	9.63	1.86

The measured losses are seen to be slightly larger than the assumed loss of 1.56 dB. Taking an average of the readings for each port, a total network loss of 1.82 dB will be assumed in the conversion of true gain to absolute gain. Adding in the 1.44 dB antenna probe mismatch loss, the total losses for each feed of each element are 3.26 dB.

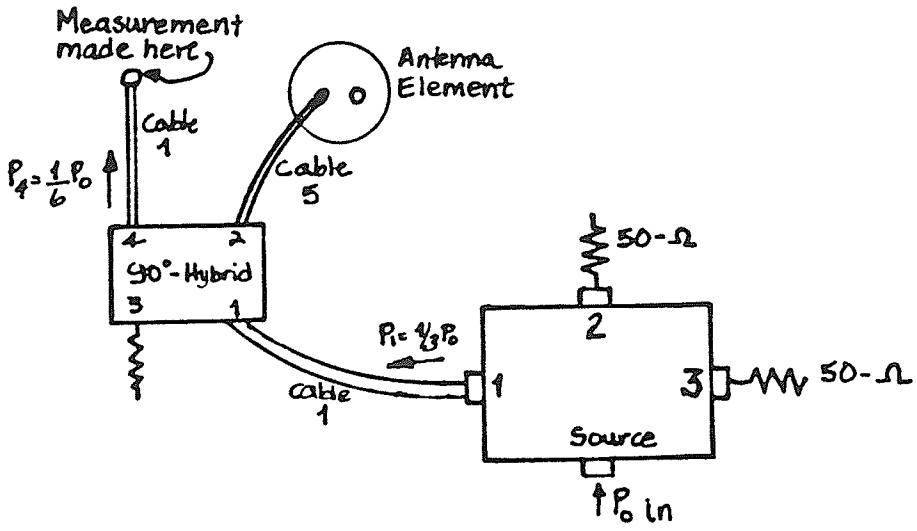

Figure 5.8: Insertion loss measurement setup for the feed network

5.4 Experimental Performance of the Array

Unlike the experiments performed with the single element, the experiments with the array were calibrated for true gain. This calibration involved the use of a standard gain horn (10 dB) whose power levels were stored and later automatically used in the gain by comparison technique to determine the true gain of the test antenna. Since the received power levels were referenced at the output of the source cable, and since the horn was matched at the test frequencies employed, the absolute gain of the test

antenna is obtained by adding on the network and mismatch losses inherent in the feeding arrangement along with a polarization gain or loss, as described in section 4.3. A +/- 0.5 dB accuracy is assumed for the recorded measurements. This number is obtained by assuming losses through the receiving and transmitting circuitry and losses due to cable leakages.

In the following subsections, the experimental results for three different patch-center to ground plane distances are presented. The ground plane effects on the axial ratio and the field distribution are presented, and based on the procedure for calculating absolute gains mentioned in Section 4.3, the absolute gains from the experimental rotating linear patterns are generated and compared with the numerically generated ones.

5.4.1 Patch-center to Ground Plane Distance d= 3.6 cm

The dimensions for the first element geometry are shown in Fig. 5.9.

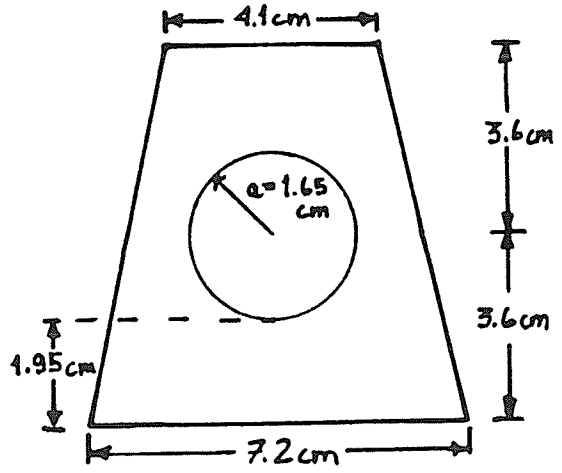

Figure 5.9: Dimensions for element with d=3.6 cm

For these dimensions, the distance from the patch-edge to the ground plane is 1.95 cm. Five such elements were joined together using copper tape and were centered on a

finite ground plane. The centers were spaced by 36 degrees with a base radius of 11.08 cm. The geometry of the array is shown in Fig. 5.10 from a top and side view.

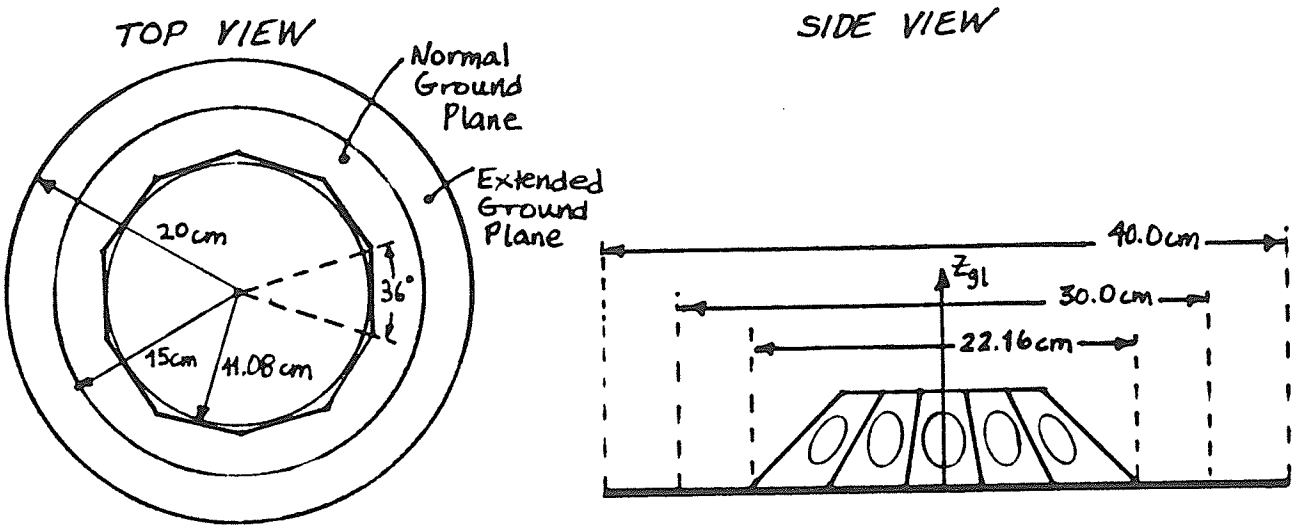

Figure 5.10: Array dimensions for d=3.6 cm

At 3.2 GHz, the distance from the array edge to the edge of the normal ground plane is 0.418 λ, and with the extension, this distance increases to 0.952 λ. At 3.0 GHz, the corresponding distances are 0.392 λ and 0.892 λ. Both these test frequencies and the respective distances in terms of their wavelengths are given since a difference in the field ellipticities was observed at the two different frequencies.

The result observed between the patterns recorded at 3.0 GHz and 3.2 throughout all the experimental work was the discrepancy in the ellipticity of the fields. An excellent example of this discrepancy is shown by the rotating linear patterns of Fig. 5.11. These are the patterns associated with the central element of the array when active in the array environment. For the pattern at 3.0 GHz, the axial ratio is poor between 0 and 30 degrees where its value is 5 dB or more, and the value is less than 2 dB

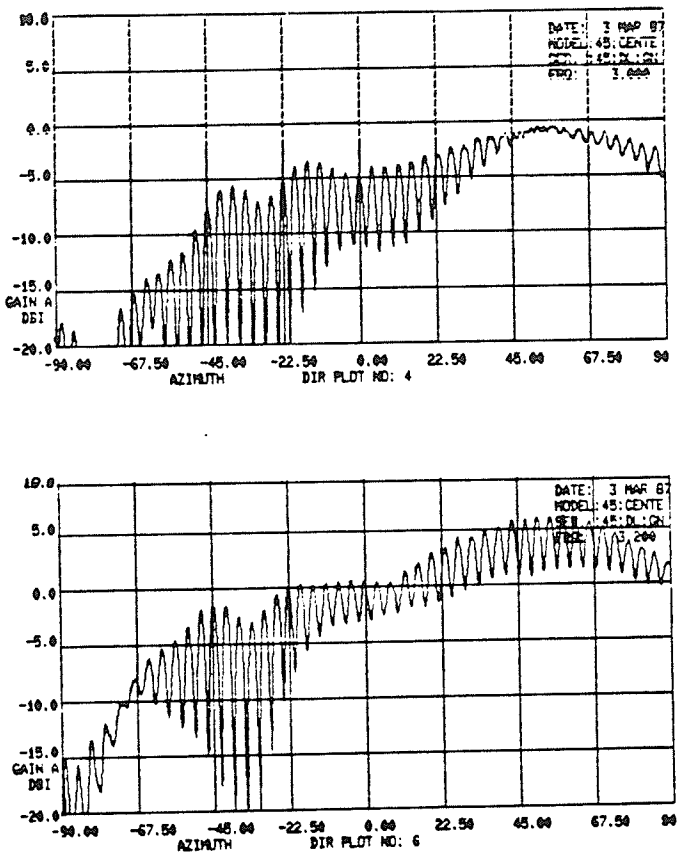

Figure 5.11: E-Plane pattern for the central element in the array environment at 3.0 (a) and 3.2 GHz (b)

between θ= 40 and 80 degrees. In fact, the fields at the beam peak are nearly perfectly circularly polarized as no peak to peak swings in the pattern are observed. The 3.2 GHz pattern, on the other hand, shows a considerable increase in the ellipticity. The axial ratio is less than 3 dB between 0 and 30 degrees, and then degrades between 40 and 60 degrees. The difference in peak gains between the two patterns is, as mentioned before, the result of the better impedance match at 3.2 GHz. Hence, if the input impedance of the antenna elements were matched to 50 Ω at 3.0 GHz, the larger gain should occur at this latter frequency and the axial ratio should remain as good. The total gain would thus be as large or larger. Note that the difference in observed axial ratios at the two frequencies were not always as drastic as presented by the results of

Fig. 5.11. A further example of this effect will be given in the next section for the patterns due to three active elements.

In the array setup, with all three of the elements active, the extended ground plane was used and absorbing material filled the conical volume space. For one of the tests, the element backplanes were not shorted to the ground plane, while in a second test they were. Figure 5.12 shows the principal E-plane patterns for these two cases.

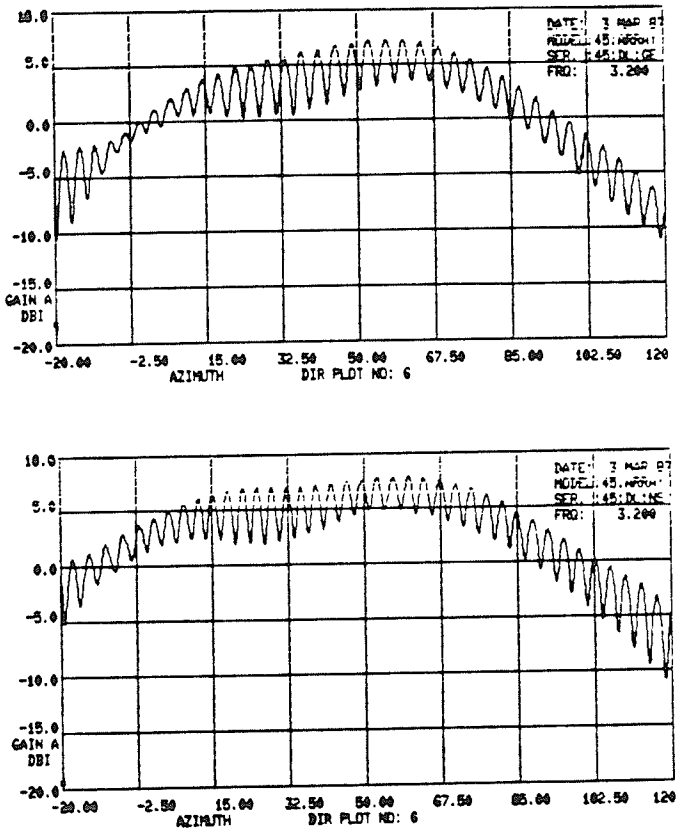

Figure 5.12 E-plane patterns for d=3.6 cm with extended ground plane and absorbing material for shorted (a) and unshorted (b) element backplanes

The rotating linear pattern beam peak occured at θ= 55 degrees for both of the tests. This is the same elevation angle as that observed from the single element tests. The shorted patch test produced a peak gain of 7.0 dB while the test without the shorted

elements produced a peak gain of 7.4 dB. The additional gain increase for the unshorted case is due to an improvement in the axial ratio of the received fields.

The absolute gain for the unshorted element case was determined from the results generated over the region from θ= -90 degrees to 100 degrees. The radiation pattern is shown in Fig. 5.13 plotted with the numerically generated E-plane pattern. For a base radius of 1.182 λ, and a patch-center to ground plane radius of 0.384 λ at 3.2 GHz, the translation distance and angle as defined in Chapter 4, are 0.95 λ and 73.4 degrees respectively. The peak gain for the theoretical plot is 11.585 dBic or 1.28 dBic smaller than that for the experimental results of the unshorted case which was 12.89 dBic. The comparison of the radiation patterns for the experimental and numerically generated results show nearly identical behaviour with the only major difference between the patterns being the beam peak location. For the numerically generated results, a beam peak at θ= 40 degrees is obtained whereas the beam peak for the experimental results is at θ= 55 degrees.

5.4.2 Patch-Center to Ground Plane Distance d=2.5 cm

The dimensions for the second element geometry used in the array are shown in Fig. 5.14. Initially, the patch-center to backplane-edge distances were 3.0 cm to the top and bottom edges. After running several tests, the bottom edge was cut to produce a patch-center to ground plane distance of 2.5 cm. Here the patch-edge to ground plane distance is only 0.85 cm or 0.091 λ at 3.2 GHz. The top portion of the array element was intentionally kept larger than the corresponding bottom portion to see if improvements in the axial ratio could be obtained over the corresponding results from the element with equal patch-center to backplane-edge distances. The base radius of the array for this case is 7.7 cm or 0.821 λ at 3.2 GHz. One of the tests run for this array geometry included the addition of a metallic cap which was shorted to the top portion of the element backplanes, while another test had absorber filling in place of the cap.

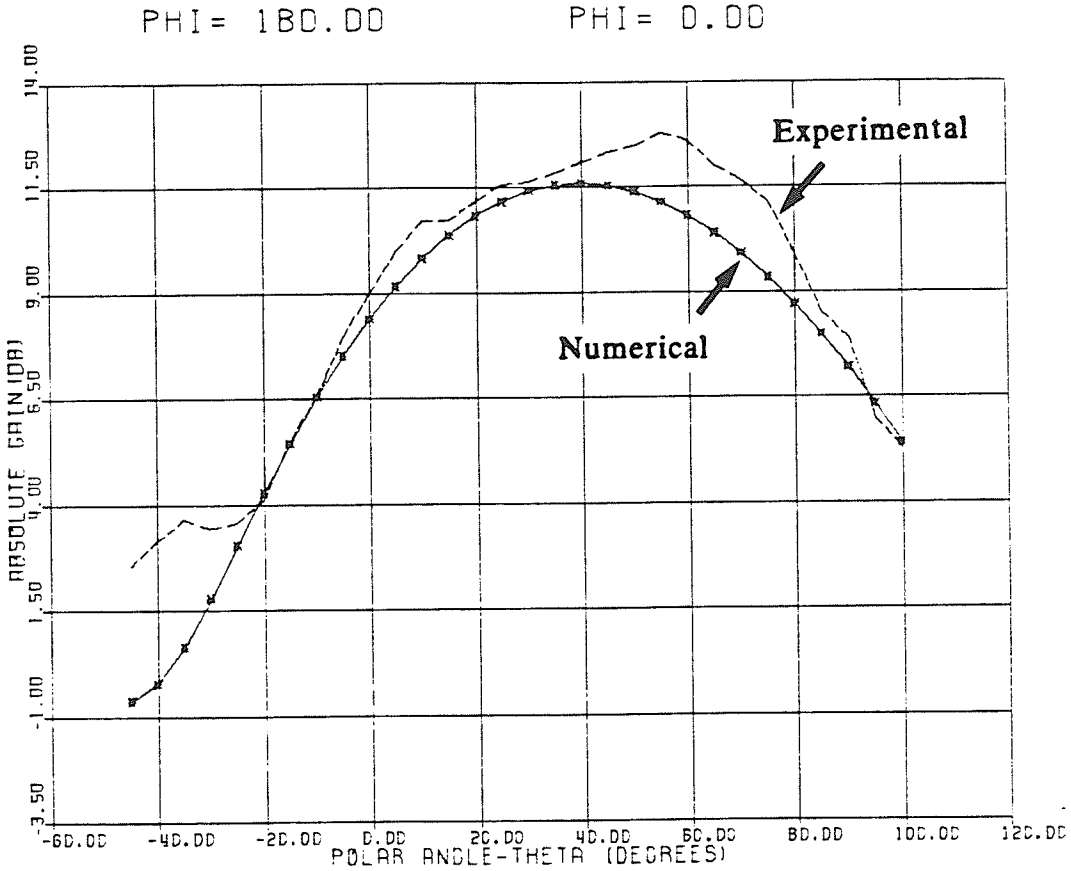

Figure 5.13: Comparison of absolute gains for the experimental and numerical results for d= 3.6 cm

Moreover, in all tests performed, the bottoms of the element backplanes shorted to the ground plane.

With the fixed ground plane, tests with and without the metallic cap were performed. The beam peaks for both cases were situated at approximately θ= 48 degrees. The beam peak shift in this case, with the normal sized ground plane, is three degrees larger than the tilt angle set on the array. Another noteworthy difference was in the ellipticity of the fields. Slightly larger oscillations were observed for the configuration which included the metallic cap. There was no difference in the peak gain. The ellipticity discrepancy was more apparent for the tests run with the extended ground plane.

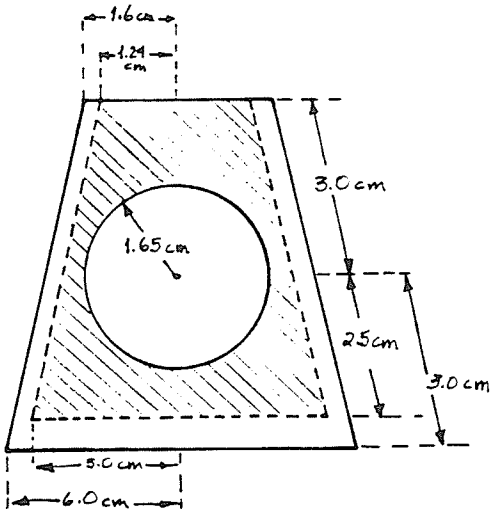

Figure 5.14: Second array element dimensions with d=2.5 cm

These results will be discussed next, but before, the difference in the ellipticities at 3.0 and 3.2 GHz are presented. Figure 5.15 shows the patterns for the absorber filled cone with the normal ground plane at the two frequencies. Here, three elements are actively receiving energy. It is noted that the discrepancy between the two patterns is not as severe as that observed in the previous section for a single active patch. However, the peak to peak swings from θ= 50 degrees to 70 degrees are certainly smaller at 3.0 GHz, than those at 3.2 GHz.

With the extended ring added to the normal ground plane, patterns were once again recorded with and without the metallic cap shorting the tops of the elements. The resulting E-plane patterns are shown in Fig. 5.16 for the two cases. The two patterns are very similar in form, as the peak gains are equal and are located at the same elevation angle of θ= 50 degrees. Hence, the extended ground plane shifts the beam an additional two degrees in comparison to the results observed without the extension. The major difference in the patterns is once more in the axial ratios. The axial ratio with the absorber is noticeably better up to θ= 50 degrees. After this angle, however, its value is nearly the same as that for the results with the metallic cap. The axial ratio in the elevation regions from 30 to 50 degrees continues to be very poor for both cases. Since the axial ratio over the band of elevation angles mentioned is not

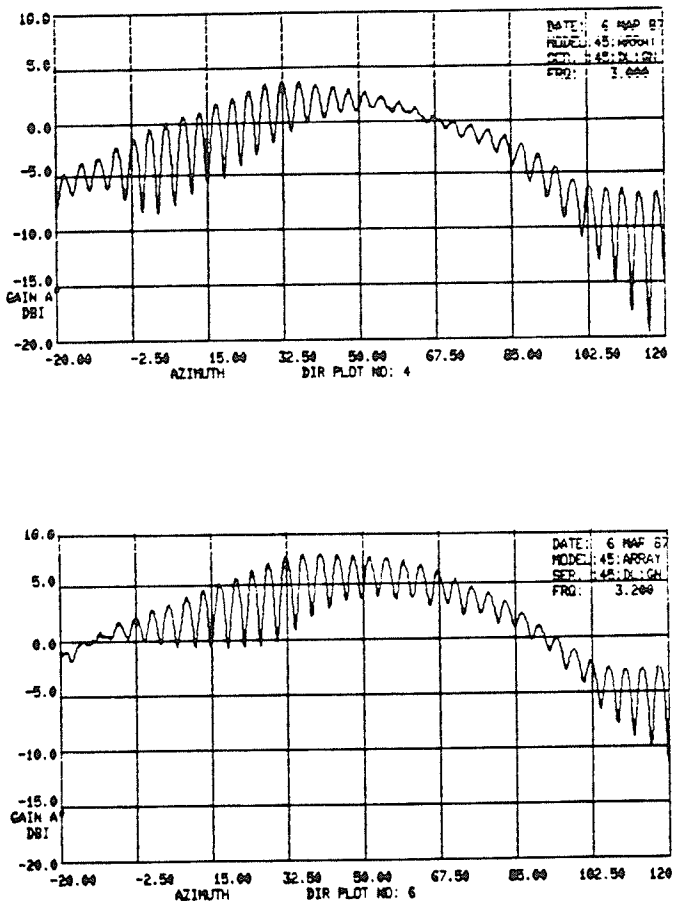

Figure 5.15: E-plane patterns at 3.0 (a) and 3.2 GHz (b) for d=2.5 cm and the normal fixed ground plane

improved with the current element dimensions, the additional length for the top portion of the element backplane is not helpful, and is therefore not required.

The experimental plot of Fig. 5.16b is converted to an absolute gain pattern by adding in the mismatch and network losses as well the polarization gain or loss. The resulting pattern is shown along with the numerically generated results in Fig. 5.17. The radial translation distance for a base radius of 0.821 λ is 0.66 λ_o at 3.2 GHz with a 73.4 degree translation angle. The peak gain for the numerically generated plot is 10.58 dBic and is located at θ= 40 degrees. The peak gain for the experimental pattern is 11.89 dBic and is located at θ= 55 degrees. The discrepancy between the two

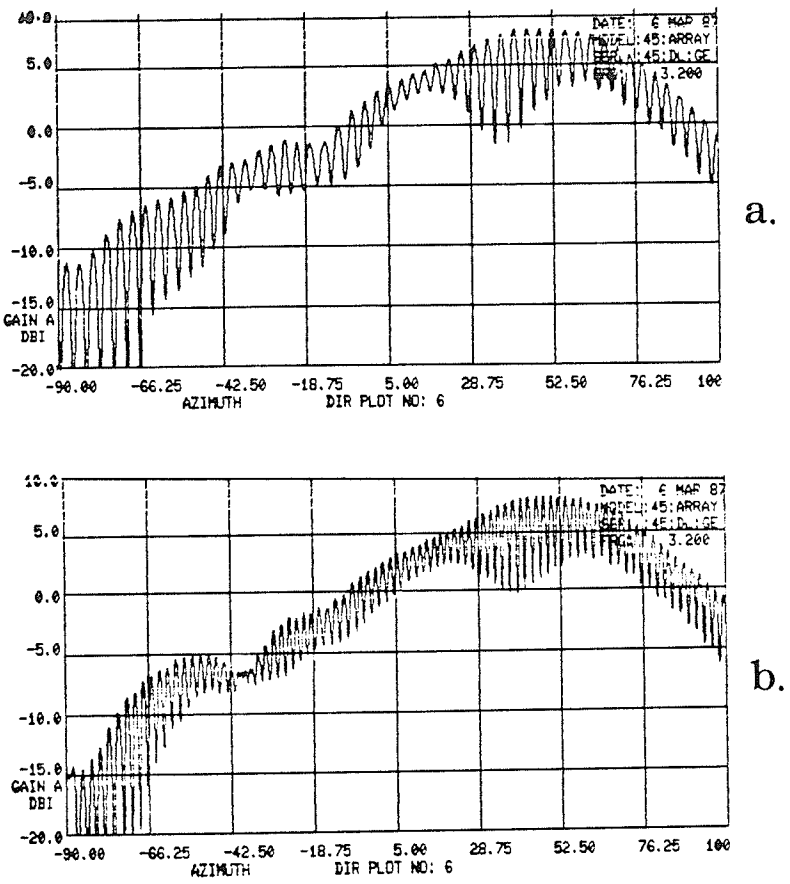

Figure 5.16: E-plane patterns for d=2.5 cm with (a) and without (b) the metallic cap over the extended ground plane

peak gains is 1.3 dBic, which is approximately the same as that for the comparison in the previous section. In fact, the overall patterns are again very similar for all elevation angles, with the exception of the observed beam peak shift and the formation of a sidelobe at θ= 20 degrees.

5.4.3 Patch-Edge to Ground Plane Distance d=2.0 cm

The final element geometry used in the experiments is shown in Fig. 5.18. Here, the distance between the patch center to ground is 2.0 cm, making the distance from

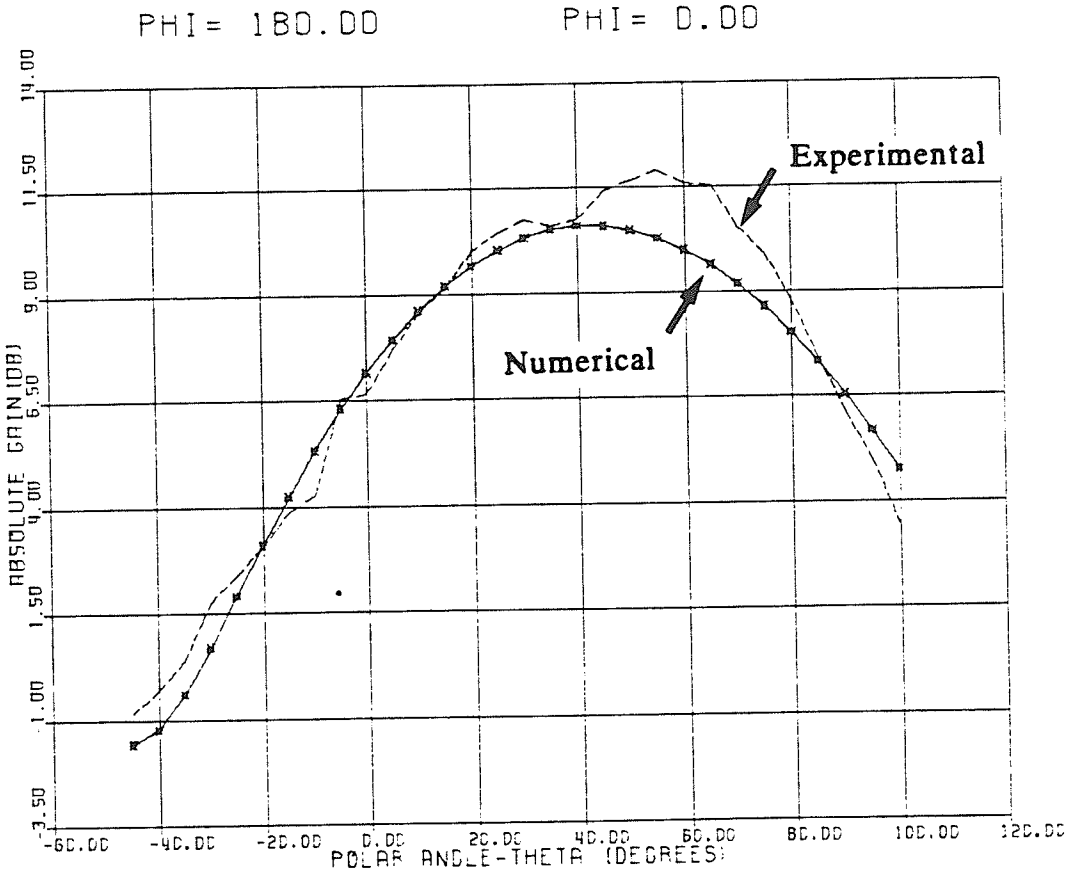

Figure 5.17: Comparison of absolute gain patterns for the experimental and numerical results with d=2.5 cm

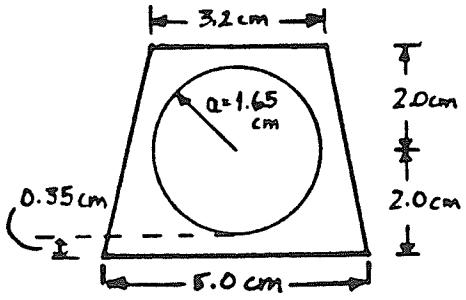

Figure 5.18: Element dimensions for d=2.0 cm

the edge of the patch to ground 0.35 cm. This is in keeping with the restriction of a minimum distance from the patch center to ground plane of a + 2h, where a is the patch radius and h is the thickness of the substrate. The elements were once again spaced azimuthally by 36 degrees and at a base radius of 7.7 cm. The translation distance to the center of the patch from the origin of the global coordinate system is therefore 0.687 λ at 3.2 GHz and the translation angle is 77.3 degrees.

The experiments performed with this last element geometry were, in fact, of the greatest interest. This is so since the element size corresponds to that with the minimum allowable distance from the patch-edge to the ground plane. Translating the dimensions to those at the midband frequency of 1.6 GHz, the base radius of the array would be 15.4 cm and the height only 5.85 cm. This would make a very compact mobile antenna if it had the necessary required field characteristics.

The first two tests performed with this array configuration used both the finite and extended ground planes with the metallic cap shorted to the element backplanes. Figure 5.19 shows the two resulting patterns at 3.2 GHz. In the comparison of the two patterns, three differences were noted. First, the peak gain of the extended ground plane was 0.5 dB greater than that for the normal sized ground plane. In performing the two experiments, the only alteration made to the geometry of the array after recording the data for the normal ground plane, was the addition of the extended ring. Hence, the supplementary gain picked up can be considered as a ground plane gain. Secondly, the location of the beam peak shifted. With the normal ground plane, the peak of the rotating linear pattern occured at θ= 46 degrees, whereas with the extension, the peak occured at θ= 52 degrees. In the current configuration, the distance between the base of the array and the ground plane edge is 0.78 λ for the normal ground plane case and 1.3 λ for the extended ground plane case. In Section 5.3.1, where the comparable distances from the base of the array to the ground plane edges were 0.418 λ and 0.952 λ, a shift in the beam peak was not noticed. In fact, the beam peak for both cases was already located at θ= 55 degrees. Moreover, in the previous

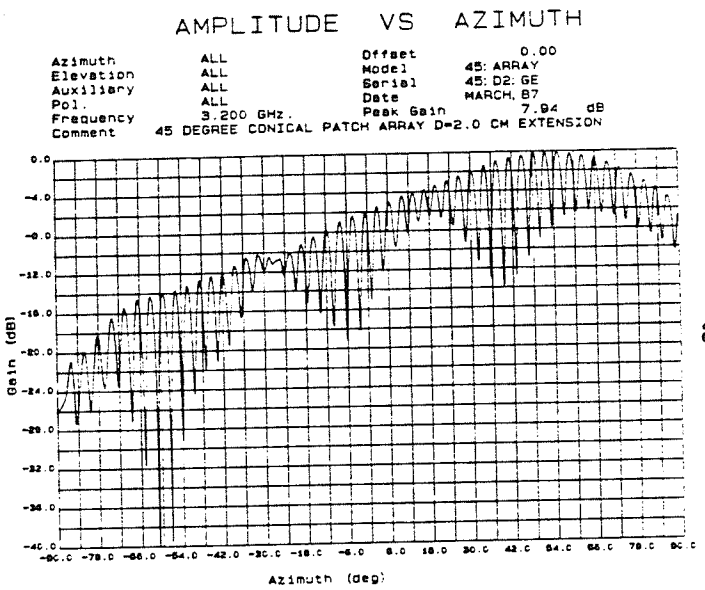

a.

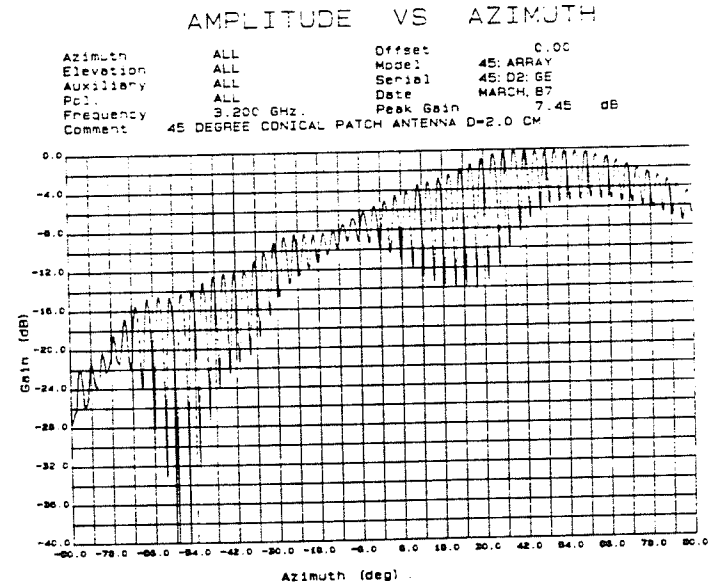

b.

Figure 5.19: E-plane pattern for d=2.0 cm with the metallic cap (a) and with and without (b) the ground plane extension

element configuration, tested in 5.3.2, only a slight shift was noted between the two peaks with and without the extended ground plane. Refering back to Figs. 5.15b and 5.16b, beam peaks at θ= 48 and 50 degrees occured for the normal and extended ground plane sizes. Hence, the addition of the extended ground plane ring becomes

more of a factor for the smaller patch-edge to ground plane distances. This was expected since a similar result was observed in the single element experiments.

The third effect observed was that of a degradation in the ellipticity of the fields. With the normal ground plane, axial ratios $\geq$ 8 dB occured between θ= 8 and 40 degrees, beyond which they leveled off to 4.5 dB. With the addition of the extended ground plane ring, the band of poor ellipticity noted split into two separate bands, the first band occurring between θ= -12 and 0 degrees and the second occurring between θ= 30 to 54 degrees. Beyond 54 degrees, the axial ratio leveled off to 5 dB. Thus, the band of poor ellipticity protrudes farther into the lower elevation region where the axial ratio is to be kept below 3 dB. This effect will have to be compensated somehow if the array configuration is to be used. Chapter 6 includes some recommendations for futher experiments which may correct the band of poor ellipticity.

When polarization gains and losses, as well as the network and mismatch losses are accounted for, the absolute gain patterns for the normal and extended ground plane sizes are shown in Fig. 5.20 along with the numerically generated absolute gain pattern. The peak gains for the experimental results are 11.39 and 11.37 dBic for the normal and extended ground plane results, respectively. The increase in peak gain of 0.5 dB of the rotating linear pattern for the extended ground plane configuration results is no longer observed here. Hence, the increase in the ellipticity neutralizes the increase in peak gain and causes further degradation to the pattern. This is noted by the formation of two side lobes, one at θ= 20 degrees, and the second at θ= -20 degrees. As well, the absolute beam peak location is shifted to θ= 60 degrees, an additional shift of 5 degrees in comparison to the previously shown absolute gain patterns. The pattern for the normal ground plane is more consistent with the numerically generated one, but still deviates slightly between θ= 0 and 30 degrees. The beam peak occurs at the familiar location of θ= 55 degrees. The numerically generated peak gain is 10.32 dBic so that the discrepancy is on the order of 1.05 dBic.

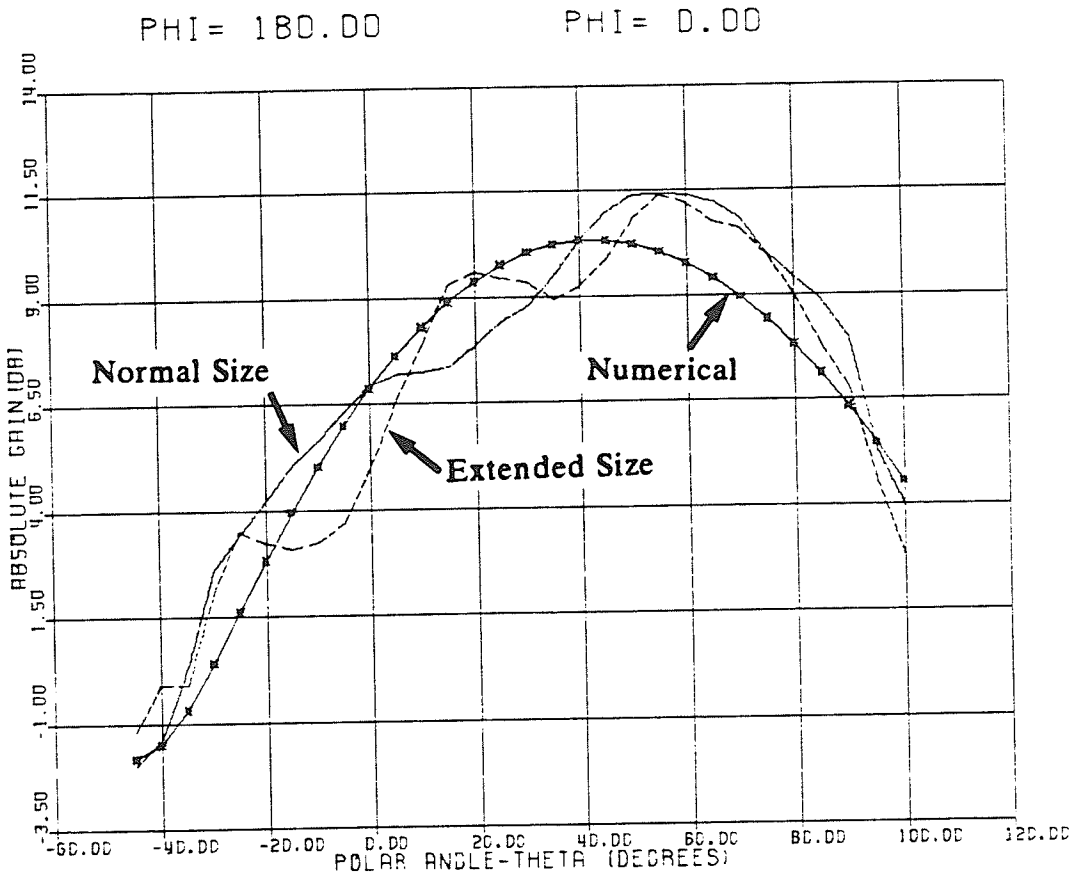

Figure 5.20: Absolute gain patterns for the experimental and numerical results with d=2.0 cm with and without the extended ground plane

To observe the effects of the metallic cap for the present element dimensions, the cap was replaced by absorbing material. The recorded E-plane rotating linear pattern is shown in Fig. 5.21. The two bands of poor ellipticity are once again observed in the results but the peak to peak swings are somewhat smaller. Overall improvements of 1.5 to 2.0 dB were noted for the results with the absorber filled cone. However, the peak gain of the rotating linear pattern decreased by 0.34 dB from 7.94 for the metallic cap case to 7.6 dB for the absorber case. The beam peak remained at θ= 50 degrees. The pattern, after conversion to absolute gain form, is shown in Fig. 5.22 along with the numerically generated one. The resulting absolute beam peak gain reoccurred at θ= 55 degrees. This result shows the influence of the metallic cap on the ellipticity. In fact, the absolute gain with the absorber was 11.43 dBic, 0.04 dBic greater than the

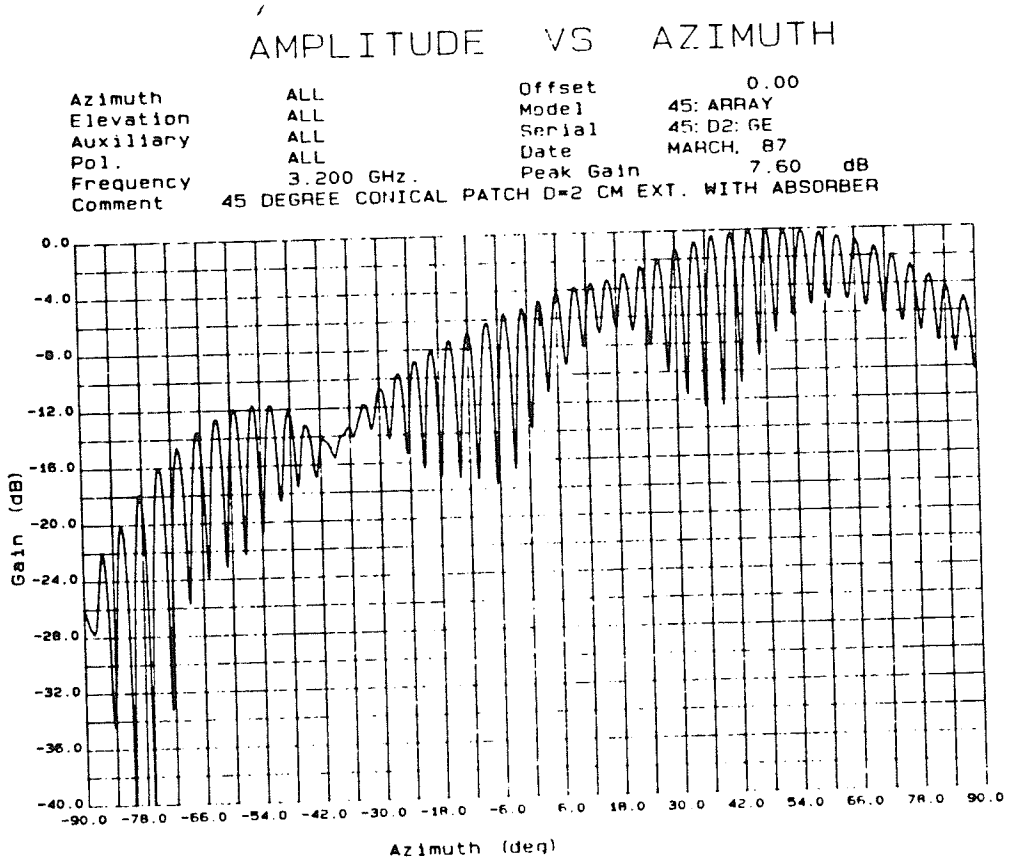

Figure 5.21: E-plane pattern for d=2.0 cm with absorber over the extended ground plane

corresponding result from the pattern with the metallic cap.

The final test performed with the current array configuration involved the addition of a 40 degree phase excitation to the elements left and right of the center element. This additional phase shift was obtained by making the feed cables from ports 1 and 3 of the 3-way power divider shown in Fig. 5.7, longer than that from port 2 by approximately 1.0 cm. At 3.2 GHz, this length corresponds to 0.107 λ which produces a phase of 0.67 radians or 38.4 degrees. The resulting rotating linear E-plane pattern is shown in Fig. 5.23. The peak gain of the recorded pattern is 7.84 dB at approximately θ= 52 degrees. This gain is slightly smaller than that for the test without the additional phase shift, but only by 0.1 dB. The location of the peak gain is also at the same value. The

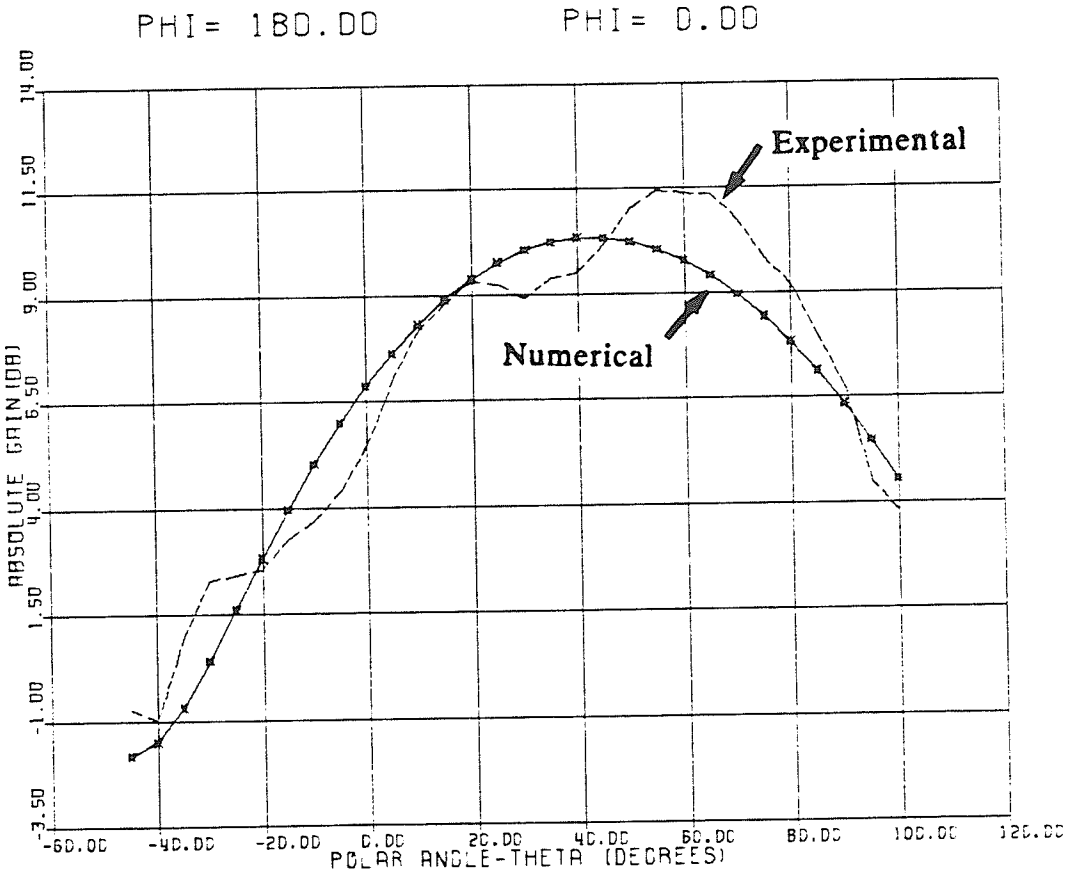

Figure 5.22: Absolute gain patterns for experimental and numerical results for d=2.0 cm with the absorber over the extended ground plane

big improvement observed over the results of Fig. 5.19, however, is in the ellipticity of the fields. The two elevation bands where the axial ratio was very poor is still observed for the present case, but the peak to peak swings are smaller by about 5 dB. For example, between θ= 30 and 40 degrees, the axial ratio achieves a maximum of 9 dB whereas in the previous test, the maximum value was 14 dB. For regions beyond 50 degrees, the axial ratio is on the order of 4 dB.

The numerically generated absolute gain pattern for the additional 40 degrees of phase excitation to the two outer elements is shown plotted in Fig. 5.24 along with the converted experimental absolute gain pattern. The numerically generated pattern achieves a peak gain of 10.44 dBic at an elevation angle of 45 degrees. The experimental pattern's peak gain is 12.07 dBic, this occuring at θ= 60 degrees. The gain

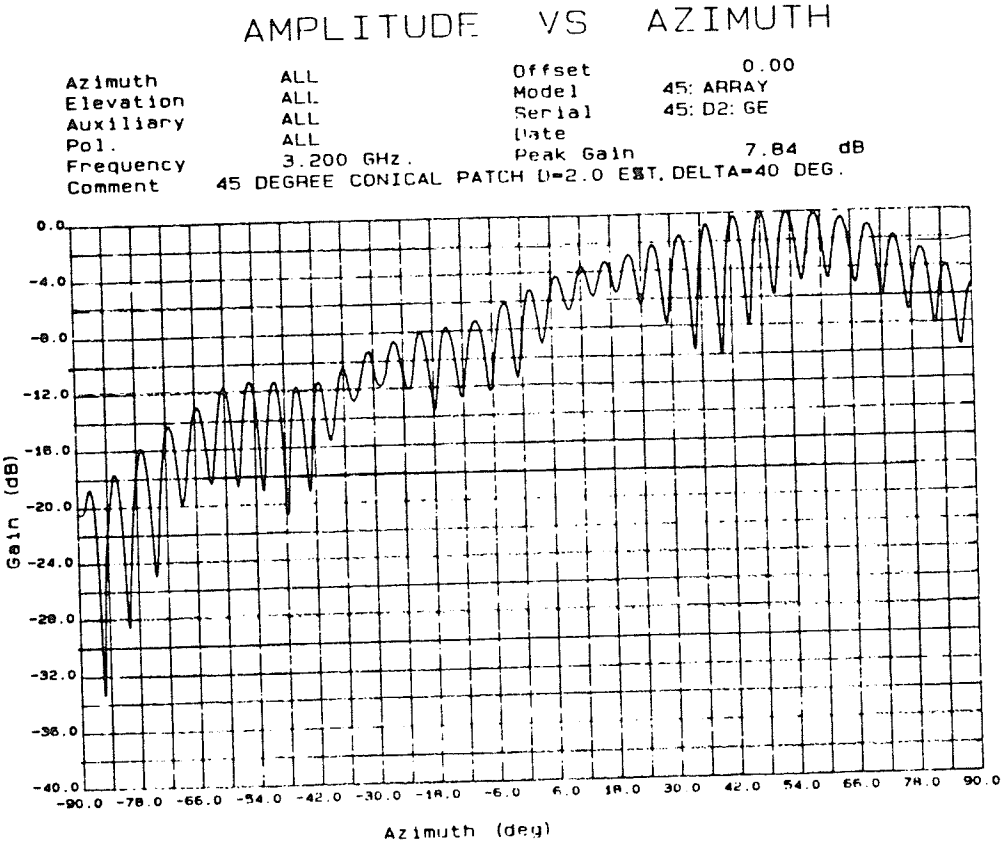

Figure 5.23: Patterns for d=2.0 cm with the metallic disc over the extended ground plane with Δ_ϕ = 45 degrees to the left and right elements

discrepancy of 1.62 dBic is slightly greater than the previous comparisons. The increase is partially linked to the improved axial ratio of the fields since the polarization correction factor increases by about 0.7 dB.

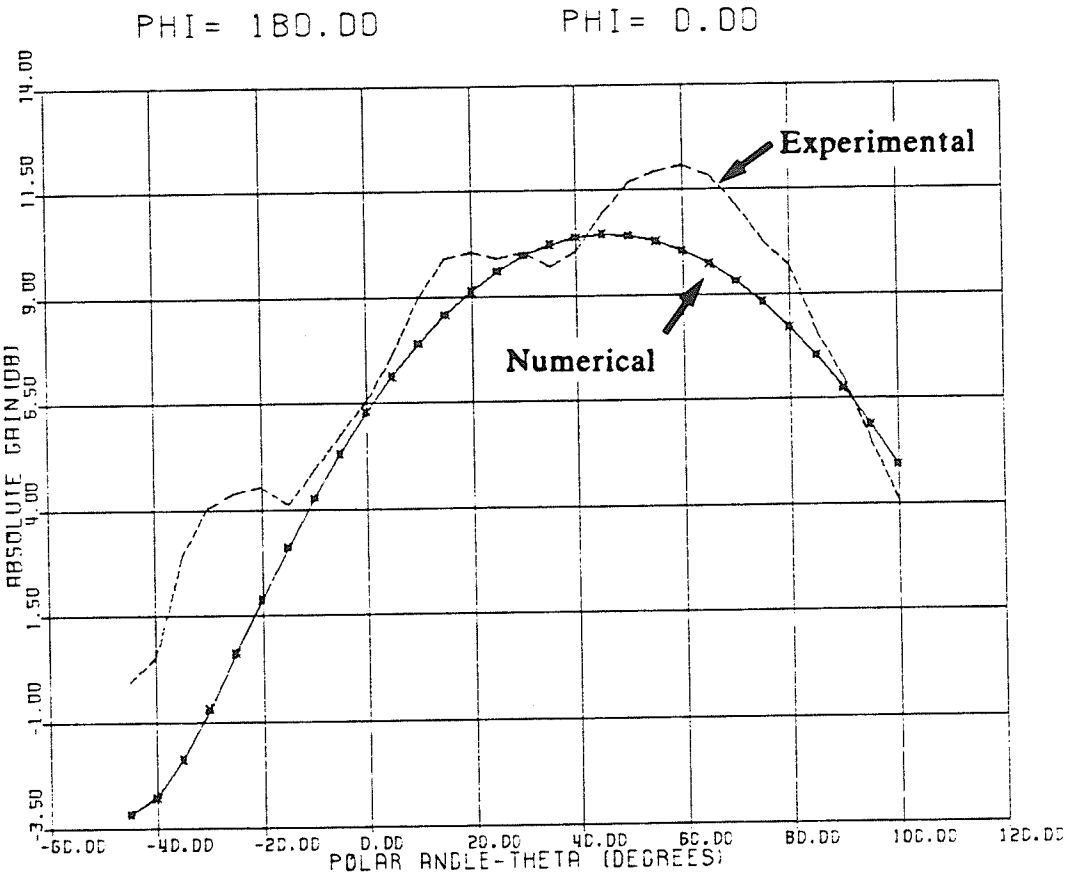

Figure 5.24: Absolute gain patterns for the numerically generated results and for d- 2.0 cm with the additional phase excitation

CHAPTER 6

DISCUSSION AND RECOMMENDATIONS

6.1 Discussion on the Numerical and Experimental Results

The numerically optimized ten- and twelve-element array configurations produce the required 10 dBic of absolute gain coverage over the elevation regions from θ= 40 to 65 degrees with the conical tilt set to ψ_p= 55 degrees. Complete azimuth coverage is obtained by phasing each of the outer two elements with an additional 45 degrees relative to the central element, thus producing two beams per three active elements. In this way, 20 beams result for the 10 element case, and 24 for the 12 element configuration. Single beam azimuth coverage over the 25 degrees of elevation could not be obtained from any of the configurations simulated, although the 12-element two and three patch excitations had fairly broad radiation patterns which nearly satisfied the requirements.

In comparing the two particular optimized array geometries, the peak gains are approximately the same at 11.36 dBic, and are located at θ= 50 degrees. The differences lie in the large array size and broader field characteristics associated with the twelve-element array. At the center L-band frequency of 1.6 GHz, the dimensions for the base radius and array height are 18.525 cm and 6.88 cm respectively. The corresponding lengths for the 12-element array are 21.975 cm and 7.2 cm. The ten-element array was, perhaps, stressed more in the work since it required two less elements and less space. Hence, the feed network presented in section 4.8 was directed towards the 10-patch array, although a similar arrangement is possible for the 12-element configuration.

From the initial experimental work studying the ground plane effects on the feed orientation and patch-edge to ground plane distance, two key observations were noted. The first was the influence on the ellipticity of the fields due to the feed placement

over the ground plane. In order to generate an equal ground plane effect on the fields produced by each feed, the feeds were rotated by 45 degrees as was shown in Section 4.3, Fig. 5.2b. The other result observed from the single element experiments was the beam peak shift due to the smaller patch-edge to ground plane distances. A 12 degree beam peak shift was observed for d=1.5 cm when the conical tilt was set at 45 degrees. Hence, the required shift to the lower elevation angles can be obtained by utilizing an appropriate patch-edge to ground plane distance. The conical tilt may thus be set to a fixed value of ψ_p= 45 degrees.

In the array experiments, three different patch-center to ground plane distances were tested. These lengths, after subtracting off the physical patch radius of 1.65 cm, translate to patch-edge to ground plane distances of 1.95 cm, 0.85 cm, and 0.35 cm. The ellipticity of the fields associated with each configuration showed a strong dependence on the ground plane size. In each case, the extended ground plane caused larger peak to peak swings in the rotating linear patterns indicating larger axial ratios. Moreover, as the patch-edge was brought closer to the ground plane, the resulting ellipticity for the same ground plane extension also became poorer. This is shown in a comparison of the rotating linear patterns of Figs. 5.17b and 5.22. The former corresponds to the geometry with the 0.85 cm distance, and the latter for the 0.35 cm distance.

In addition to the ellipticity degradation, a beam peak shift is also characteristic of the smaller patch-edge to ground plane distances. For the very first configuration tested, the beam peak of the rotating linear pattern was located at θ= 55 degrees. This value was associated with the extended and normal ground plane sizes. For the smaller patch-edge to ground plane distances, the beam peaks with and without the extended ground planes were different. The extended ground plane caused shifts of 2 and 6 degrees in the beam peak location for the second and third array configurations respectively. The patterns of Fig. 5.20 show the 6 degree shift very explicitly for the results with and without the ground plane extension.

Finally, the influence of the ground plane is also observed in the peak gain of the rotating linear patterns. For the third array configuration with a patch-edge to ground plane distance of 0.35 cm, a 0.5 dB gain increase was observed with the addition of the extended ring. This increase in the gain, however, was neutralized by the degradation in the ellipticity of the fields. This effect was apparent from the absolute gain patterns which showed peak gains of 11.37 and 11.39 dBic with and without the extended ground plane ring.

6.2 Recommendations for Future Analysis and Experimentation

In the numerical work, the array was modelled in free space and only dominant mode operation was assumed for the array elements. Although the results between the numerical and experimental work were similar, it would be beneficial to incorporate a ground plane in future analysis. The ground plane effects could then be included into the array design prior to any experimental tests. As well, a more complex method of analyzing the single element could be used in the solution process. The added complexity would ensure that all element modes, no matter how weak in comparison to the dominant mode excitation, would be included in the solution of the local and the far fields.

The first two recommendations for future experimental work would be to match the elements of the array to 50 Ω at the resonant frequency, and to build in a parasitic element above the active one. The first recommendation will undoubtedly improve the axial ratio of the fields, since a difference in the ellipticity was noted at the two resonant frequencies. Moreover, by matching the elements, a better mismatch loss should be obtained since the return loss would be in the neighborhood of -20 dB. The second recommendation will result in an increase in the frequency bandwidth of the antenna. This will enable the array to operate over the required uplink and downlink frequency bands.

Furthermore, with the last array configuration presented, the array should be suspended above the ground plane by various distances. Effects on the poor ellipticity bands could be studied in terms of the element distances above the ground plane. As well the beam peak location and its value could also be observed, and by not shorting the elements to the ground plane, the effects of the ground plane currents could also be observed. Furthermore, a test should be run with the array elements not shorted together. This too would give the designer some information of the influence of the backplane currents on the array's radiation characteristics.

A test using the the elements of the first array configuration should also be run. For this test, the elements should be shorted to the normal sized ground plane. An RF-choke could then be attached to the portion of the ground plane protruding beyond the base of the array. The purpose of the choke would be to dissipate the surface currents formed on the extension. The resulting structure could then be placed on top of a larger ground plane and the effects of the isolation between the array and the ground plane could be observed.

Finally, the 45 degrees of additional phase excitation should be utilized in the experimental work and experiments should be run for several ϕ-cut planes to identify the plane with the beam peak. In this way, the true coverage region could also be found and compared to that generated numerically.

REFERENCES

[1] Butterworth, J.S. and Matt E.E., "*The Development of a Vehicle Antenna for Satellite Communications in the 800 MHz Band*", May, 1982.

[2] Shafai, L. and Kumar G., "*Microstrip Antennas as a Candidate for MSAT Vehicular Application* ", Special report TR84-1, University of Manitoba, Winnipeg, May, 1984.

[3] Sandrin, W.A., "*Land-Mobile Start-up Systems*", Comsat Technical Review, vol. 14, no. 1, spring 1984, pp. 137-164.

[4] Siddiqi, A.I. et al, "*An L-Band Active Array System for Global Coverage*", Comsat Technical Review, vol. 15, no. 1, spring 1985, pp. 39-69.

[5] Shafai, L. et al, "*Performance of Planar Microstrip Arrays Including Mutual Coupling: MSAT Application*", Special Report TR87-1, University of Manitoba, Winnipeg, 1987.

[6] Neilson, Gordon B., "*Computer Aided Design Techniques Applied to the Development of an MSAT Ground Station Antenna*", M.Sc. Thesis, University of Manitoba, Winnipeg, 1986.

[7] Jacob, Nathan R. and Feuer Brian N., "*System Design of a Seven Element Drooping Dipole Array*", B.Sc. Thesis, University of Manitoba, Winnipeg, 1986.

[8] Milne, R.M.T., "*A Small Adaptive Array Antenna for Mobile Communications*", IEEE 1985 International Symposium on Antennas and Propagation Digest, vol. II, June 1985, pp. 797-800.

[9] McNally, J.L., "*A Mobile Satellite System for Canada*", FibreSat 86, Vancouver, Canada, Sept. 9-12, 1986, pp.14-21.

[10] Jordan E.C. and Miller W.E., "*Slotted Cylinder Antenna*", Electronics, February 1947, pp.90-93.

[11] Harrington, R.F., *Time Harmonic Electromagnetic Fields,* McGraw-Hill, 1961.

[12] Ragheb, H.A. and Hamid M., "*Multiple Interaction Between a Radiating Dipole and Parallel Conducting Cylinder*", Canadian Journal of Physics, vol. 65, no.2, February 1987, pp. 101-108.

[13] Hahn, Ronald F. and Fikioris John G., "*Impedance and Radiation Patterns of Antennas above Flat Discs*", IEEE Trans. on Ant. and Prop., January 1973, pp. 97-100.

[14] Bahl, I.J. and Bhartia P., *Microstrip Antennas,* Dedham, M.A.: Artech House, 1982.

[15] Kishk, A.A. and Shafai L., "*The Effect of Various Parameters of Circular Microstrip Antennas on their Radiation Efficiency and the Mode Excitation*", IEEE Trans. on Ant. and Prop., AP-34, no. 8, August 1986, pp.969-976.

[16] Shen, Liang C., "*Analysis of a Circular-Disc Printed-Circuit Antenna*", Proceedings IEE, vol. 126, no. 12, December 1979, pp. 1220-1222.

[17] Bhattacharyya A.K. and Garg R., "*Self and Mutual Admittance Between Two Concentric Coplanar, Circular Radiating Current Sources*", Proceedings IEE, vol. 131, Pt. H, no.3, June 1984, pp. 217-219.

[18] Elliot, Robert S., *Antenna Theory and Design,* Prentice-Hall Inc., Englewood Cliffs, New Jersey, 1981.

[19] Sroka, P.J., "*Nomograph saves time in Converting Antenna Gain*", Microwaves, March 1974, pp.54-55.

[20] Ma, M.T., *Theory and Application of Antenna Arrays,* Wiley Interscience Publication, John Wiley and sons, New York, 1973.

[21] Abouzahra, Mohamed D., "*Design and Performance of a Wideband Multilayer Feed Network*", *IEEE MTT-S Digest, June 1986, pp. 143-146.*

[22] Yau, W., Schellenberg J.M. and Shih J.C., "*A New n-Way Broadband Planar Power Combiner/Divider*", *IEEE MTT-S Digest, June 1986, pp. 147-149.*

[23] Bhattacharyya A.K. and Garg R., "*Input Impedance of Annular Ring Microstrip Antenna using Circuit Theory Approach*", IEEE Trans. on Ant. and Prop., vol AP-33, no.4, April 1985, pp. 369-374.

[24] Liboff, Richard L. and Dalman G.C., *Transmission Lines, Waveguides and Smith Charts,* Macmillan Publishing Co., N.Y, N.Y, 1985.

[25] Carver, Keith R. and Mink James W., "*Microstrip Antenna Technology*", *IEEE Trans. on Ant. and Prop., vol. AP-29, no. 1, January 1981, pp.2-24.*

[26] Hori, T., Terada N. and Kagoshima K., *Electronically Steerable Spherical Array Antenna for Mobile Earth Station*", EAP-S Digest , March 1987, pp.55-58.

APPENDIX A

Generation of the Far Field Expressions Based on The Electric and Magnetic Vector Potentials

Using Fig. 4.1 of Chapter 4 as the associated coordinate system, the electric vector potential can be defined as [1],

$$\vec{F}(x,y,z) = \int_S \mu_o \frac{\vec{M}(x',y',z')}{4\pi R} e^{-j(kR-\alpha_i)}\, dS' \qquad (A.1)$$

and the magnetic vector potential as [1],

$$\vec{A}(x,y,z) = \int_S \mu_o \frac{\vec{J}(x',y',z')}{4\pi R} e^{-j(kR-\alpha_i)}\, dS' \qquad (A.2)$$

where, $R = \sqrt{(x-x')^2 + (y-y')^2 + (z-z')^2}$

$= r - (x'\sin\theta\cos\phi + y'\sin\theta\sin\phi + z'\cos\theta)$

$= r - r'(\sin\theta\sin\theta'\cos(\phi-\phi') + \cos\theta\cos\theta')$

and α_i is the phase excitation of the i^{th} feed. For the circular patch antenna,

$$r' = a$$

$$\theta' = 90$$

$$dS' = a\, d\phi'\, dz'$$

$$\vec{M}(x',y',z') = \frac{2}{\mu_o} E_z(a,\phi',h)\hat{a_\phi} = M_\phi \hat{a_\phi} \qquad (A.3)$$

$$= -\sin\phi' M_\phi \hat{a_x} + \cos\phi' M_\phi \hat{a_y} \qquad (A.4)$$

and, $\vec{J}(x',y',z') = -2y_a E_z(a,\phi',h)\hat{a_z}$

The Cartesian components can be translated to the spherical coordinate system by using the appropriate direction cosines,

$$\vec{F}_\theta(r,\theta,\phi) = \cos\theta\cos\phi\,\vec{F}_x + \cos\theta\sin\phi\,\vec{F}_y$$

$$\vec{F}_\phi(r,\theta,\phi) = -\sin\phi\,\vec{F}_x + \cos\phi\,\vec{F}_y$$

$$\text{and,}\quad \vec{A}_\theta(r,\theta,\phi) = -\sin\theta\vec{A}_z \tag{A.5}$$

where,

$$\vec{F}_x(r,\theta,\phi) = -\frac{\mu_o}{4\pi}\int_S \sin\phi' M_x e^{-j(kR-\alpha_i)}dS' \tag{A.6}$$

$$= -C_1\int_0^{2\pi} \sin\phi'\cos n\phi' e^{jk_oL}d\phi'$$

$$\text{where,}\quad L = a\sin\theta\cos(\phi-\phi')$$

$$\text{and,}\quad C_1 = \frac{E_o}{2\pi}J_n(k_{nm}a)hae^{-jk_or}e^{j\alpha i}$$

Similarly,

$$\vec{F}_y(r,\theta,\phi) = C_1\int_0^{2\pi} \cos\phi'\cos n\phi' e^{jk_oL}d\phi' \tag{A.7}$$

$$\text{and,}\quad \vec{A}_z(r,\theta,\phi) = -y_a\mu_oC_1\int_0^{2\pi} \cos n\phi' e^{jk_oL}d\phi' \tag{A.8}$$

Therfore,

$$\vec{F}_\theta(r,\theta,\phi) = C_1\cos\theta\int_0^{2\pi}[-\cos\phi\sin\phi' + \sin\phi\sin\phi']\cos n\phi' e^{jk_oa\sin\theta\cos(\phi-\phi')}]\,d\phi'$$

$$= C_1\cos\theta\int_0^{2\pi}\sin(\phi-\phi')\cos n\phi' e^{jk_oa\sin\theta\cos(\phi-\phi')}d\phi' \tag{A.9}$$

Letting $u = \phi - \phi'$, $du = -d\phi'$, one obtains,

$$\vec{F}_\theta(r,\theta,\phi) = -C_1\cos\theta\int_0^{2\pi}\sin u\cos n(\phi-u)e^{jk_o\sin\theta\cos u}du \tag{A.10}$$

Replacing cosn($\phi - u$) by cosnϕ cosnu + sinnϕ sinnu,

$$\vec{F}_\theta(r,\theta,\phi) = - C_1\cos\theta \left[\cos n\phi \int_0^{2\pi} \cos nu \sin u e^{jk_o a \sin\theta \cos u} du \right.$$

$$\left. + \sin n\phi \int_0^{2\pi} \sin nu \sin u e^{jk_o a \sin\theta \cos u} du \right] \qquad (A.11)$$

The first integral has a null value due to the multiplication of an odd and even function. In the second integral, $\sin nu \sin u = \frac{1}{2}(\cos(n-1)u - \cos(n+1)u)$ is inserted to obtain,

$$\vec{F}_\theta(r,\theta,\phi) = - \frac{C_1}{2} \sin n\phi \left[\int_0^{2\pi} \cos(n-1)u e^{jk_o a \sin\theta \cos u} du \right.$$

$$\left. - \int_0^{2\pi} \cos(n+1)u e^{jk_o a \sin\theta \cos u} du \right] \qquad (A.12)$$

Now, one uses the fact that the integral representation of a Bessel function is given as,

$$J_n(x) = \frac{j^{-n}}{\pi} \int_0^{\pi} e^{jx\cos\theta} \cos n\theta \, d\theta \qquad (A.13)$$

to obtain the final form,

$$F_\theta(r,\theta,\phi) = - C_1 \cos\theta \sin\phi \, \pi j^{n-1} [J_{n-1}(k_o a \sin\theta) + J_{n+1}(k_o a \sin\theta)] \qquad (A.14)$$

The other two vector potential components are obtained in a similar fashion,

$$\vec{F}_\phi(r,\theta,\phi) = - C_1 \cos n\phi \, \pi j^{n+1} [J_{n-1}(k_o a \sin\theta) - J_{n+1}(k_o a \sin\theta)] \qquad (A.15)$$

and,

$$\vec{A}_\theta(r,\theta,\phi) = - 2C_1 \pi y_a \cos n\phi \, j^n J_n(k_o a \sin\theta) \sin\theta \qquad (A.16)$$

The far field components are transverse to the radial direction of propagation and are represented in terms of the vector potentials as,

$$\vec{E}_\theta(r,\theta,\phi) = j(\omega\mu_o A_\theta - k_o F_\phi)$$

$$= C_1 \pi \cos n\phi \, j^{n+1} \, [- 2\omega\mu_o y_a J_n(k_o a \sin\theta)\sin\theta$$

$$+ jk_o(J_{n+1}(k_o a\sin\theta) - J_{n-1}(k_o a\sin\theta))] \qquad (A.17)$$

and,

$$\vec{E}_\phi(r,\theta,\phi) = jk_o F_\theta$$

$$= - k_o C_1 \cos\theta \sin n\phi \, \pi j_n[J_{n-1}(k_o \sin\theta) + J_{n+1}(k_o a\sin\theta)] \qquad (A.18)$$

APPENDIX B

The Derivation of the Coordinate Transformation Matrix due to a Pitch-Yaw-Roll Movement

The axes of the elements are rotated by a pitch-yaw-roll (ψ_p , ψ_r , ψ_y) with respect to the global coordinate system, and then they are translated by a vector $\vec{r}_t$ (r_t , θ_t , ϕ_t) to the required local origin. The global coordinate system coordinates and symbols will be subscripted with a gl. The rotated coordinate system will be super-scripted with primes. Figure B.1 shows the completely rotated system.

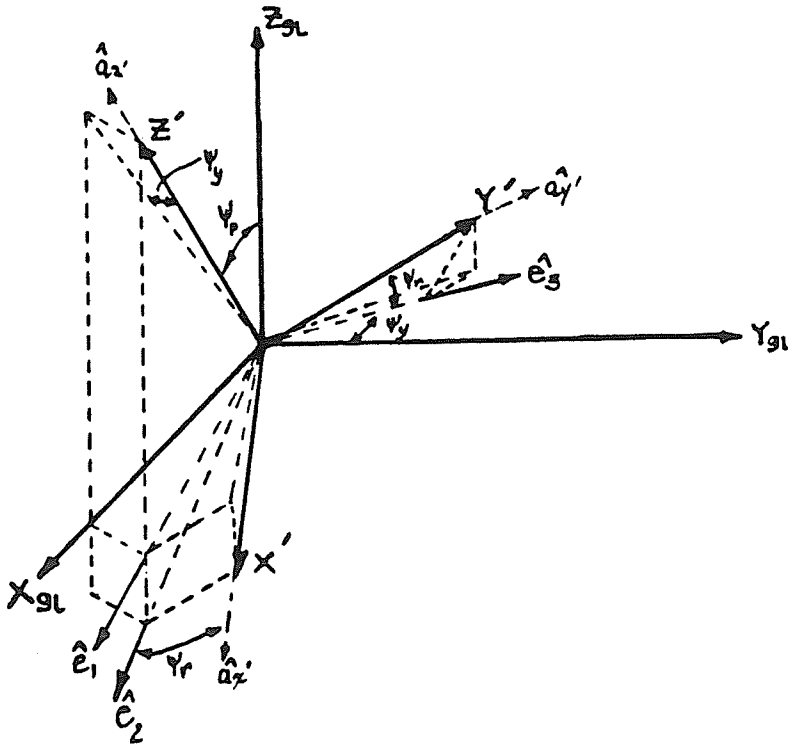

Figure B.1: The rotated local coordinate system

From Fig. B.1, three unit vectors were added, $\hat{e}_1$, $\hat{e}_2$, and $\hat{e}_3$. These are defined in terms of the global unit vectors as,

$$\hat{e}_1 = \cos\psi_y \, \hat{a}_{x_{gl}} + \sin\psi_y \, \hat{a}_{y_{gl}} \tag{B.1}$$

$$\hat{e}_2 = \cos\psi_p \, \hat{e}_1 - \sin\psi_p \, \hat{a}_{z_{gl}} \tag{B.2}$$

$$\hat{e}_3 = -\sin\psi_y \, \hat{a}_{x_{gl}} + \cos\psi_y \, \hat{a}_{y_{gl}} \tag{B.3}$$

Note that the unit vectors $\hat{e}_1$ and $\hat{e}_3$ are in the $X_{gl} - 0 - Y_{gl}$ planes. The unit vector $\hat{e}_2$ is located in the $X' - 0 - Y'$ plane (a plane tilted θ degrees and pivoted on the Y_{gl} axis). The rotated coordinate system's unit vectors can now be expressed in terms of these three unit vectors which in turn expresses them in terms of the global coordinate's unit vectors.

For $\hat{a}'_x$:

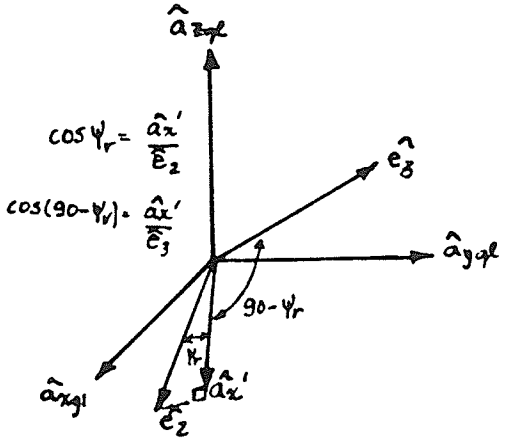

$$\hat{a}'_x = \cos\psi_r \hat{e}_2 + \sin\psi_r \hat{e}_3 \tag{B.4}$$

For $\hat{a}'_y$:

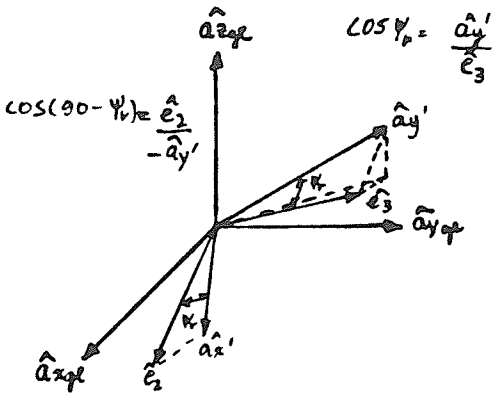

$$\hat{a}'_y = -\sin\psi_r\,\hat{e}_2 + \cos\psi_r\,\hat{e}_3 \tag{B.5}$$

For $\hat{a}'_z$:

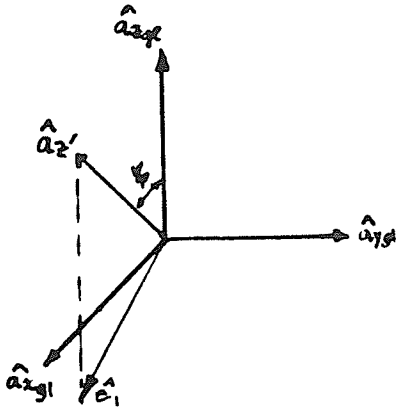

$$\hat{a}'_z = \cos\psi_p\,\hat{a}_{z_{gl}} + \sin\psi_p\,\hat{e}_1 \tag{B.6}$$

Substituting expressions B.1-B.3 into B.4-B.5, the unit vectors associated with the rotated coordinate system in terms of the global coordinate system are,

$$\hat{a}'_x = \alpha_{11}\hat{a}_{x_{gl}} + \alpha_{21}\hat{a}_{y_{gl}} - \alpha_{31}\hat{a}_{z_{gl}} \tag{B.7}$$

$$\hat{a}'_y = \alpha_{12}\hat{a}_{x_{gl}} + \alpha_{22}\hat{a}_{y_{gl}} + \alpha_{32}\hat{a}_{z_{gl}} \tag{B.8}$$

$$\hat{a}'_z = \alpha_{13}\hat{a}_{x_{gl}} + \alpha_{23}\hat{a}_{y_{gl}} + \alpha_{33}\hat{a}_{z_{gl}} \tag{B.9}$$

The direction cosines denoted by α_{ij} are given by

$$\alpha_{11} = \cos\psi_p\cos\psi_y\cos\psi_r - \sin\psi_y\sin\psi_r$$

$$\alpha_{12} = -\cos\psi_p\cos\psi_y\sin\psi_r - \sin\psi_y\cos\psi_r$$

$$\alpha_{13} = \sin\psi_p\cos\psi_y$$

$$\alpha_{21} = \cos\psi_p\sin\psi_y\cos\psi_r + \cos\psi_y\sin\psi_r$$

$$\alpha_{22} = -\cos\psi_p\sin\psi_y\sin\psi_r + \cos\psi_y\cos\psi_r$$

$$\alpha_{23} = \sin\psi_p\sin\psi_y$$

$$\alpha_{31} = -\sin\psi_p\cos\psi_y$$

$$\alpha_{32} = \sin\psi_p\sin\psi_y$$

$$\alpha_{33} = \cos\psi_p$$

To be certain the the direction cosines are orthogonal, it is easily shown that the $\det(\alpha_{ij}) = 1$, i.e.

$$\begin{vmatrix} \alpha_{11} & \alpha_{12} & \alpha_{13} \\ \alpha_{21} & \alpha_{22} & \alpha_{23} \\ \alpha_{31} & \alpha_{32} & \alpha_{33} \end{vmatrix} = 1$$